Diss. ETH No. 12976

Electronic Properties of Tailored Semiconductor Nanostructures with Tunable Dimensionality

A dissertation submitted to the
SWISS FEDERAL INSTITUTE OF TECHNOLOGY
ZURICH

for the degree of
Doctor of Natural Sciences

presented by

Gian Salis

born 26. December 1970
citizen of Vicosoprano and Soglio (GR)

accepted on the recommendation of

Prof. Dr. Klaus Ensslin, examiner
Prof. Dr. Gianni Blatter, co-examiner

1999

Contents

1 **Introduction** 1

2 **Sample Fabrication and Characterization** 5
- 2.1 AlGaAs System 5
- 2.2 Samples 6
  - 2.2.1 Layer Sequence 6
  - 2.2.2 Optical Lithography and Ohmic Contacts 7
  - 2.2.3 Measurement Set-Up 10
- 2.3 The PQW as a Quasi-3D System 11
- 2.4 Electron States 12
  - 2.4.1 Bloch Wave Functions 12
  - 2.4.2 Self-Consistent Calculation of the Electron States 14
- 2.5 Transport 15
  - 2.5.1 Low Temperature, Magnetic Fields 17
  - 2.5.2 Shubnikov-de Haas Oscillations 18
- 2.6 Tuning the Electron Gas 22
  - 2.6.1 Density Tuning 22
  - 2.6.2 Displacing the Electron Gas 24

3 **Wave Function Spectroscopy** 29
- 3.1 Concept of Wave Function Spectroscopy 30
- 3.2 Experimental Details 32
- 3.3 Width of the Electron Distribution 32
- 3.4 Scanning the Wave Function 35
- 3.5 Discussion and Conclusions 36

4 **Scattering Times in Parabolic Quantum Wells** 38
- 4.1 Calculation of Scattering Times 38
  - 4.1.1 Fermi's Golden Rule 38
  - 4.1.2 Electron Screening 39
  - 4.1.3 Scattering Mechanisms 42
  - 4.1.4 Scattering Times in a Two-Subband Quantum Well 44
- 4.2 How Does Elastic Scattering Vary Across a PQW? 45
  - 4.2.1 Introduction 46
  - 4.2.2 Experimental 46

4.2.3 Determination of Drude Scattering Times 47
4.2.4 Determination of Single-Particle Scattering Times 50
4.2.5 Calculation of the Scattering Times 51
4.2.6 Density-Dependence of the Scattering Times 53
4.2.7 Conclusions 53

5 Phase-Coherent Transport **55**
5.1 Phase-Coherence Length 55
5.2 Weak Localization 56
5.3 Universal Conductance Fluctuations 59
5.3.1 Theory 60
5.3.2 Experimental setup and data evaluation 60
5.4 Conclusions 65

6 Subband Densities and in-Plane Magnetic Field **66**
6.1 Introduction 67
6.2 Experiment 68
6.3 Comparison with theory 70
6.3.1 First order perturbation theory 70
6.3.2 Second-order term and subband-dependent DOS 72
6.3.3 Exact solution for a parabolic potential 73
6.4 Discussion and Conclusions 73

7 Ballistic One-Dimensional Systems **77**
7.1 Introduction 79
7.2 Experiment 80
7.3 Tuning the Shape of the Constriction 81
7.4 1D Subband Spectrum in Magnetic Fields 84
7.5 Conclusions 88

8 Conclusions and Outlook **90**

A Comparison of Screening Approximations **92**

B 2D Parabolic Confinement **94**

C List of Samples **98**

Publications **99**

Bibliography **100**

Acknowledgements **108**

Curriculum Vitae **110**

Abstract

The operation of conventional semiconductor devices can be understood within a semiclassical theory of conduction. Where the dimensions of the considered structures are comparable to the Fermi wave length, quantum effects become important. The finite size of such structures constrains the electron motion, and the energy gets quantized. With the ongoing miniaturization of computer chips this limit will be reached soon. For further size-reduction it is of fundamental importance to know how conduction in such quantum structures is described. With the technological progress it has become possible to fabricate well-defined structures in the nanometer range, where the atomic composition is controlled within monolayers. In principle, such "nanostructures" are the experimental realization of standard text-book examples of a particle in a quantum well. However, the nanostructure is neither an abstract quantum well nor an isolated atom, but still consists of millions of atoms and electrons. This thesis is aimed to investigate how far transport in nanostructures can be described by single-particle quantum mechanics, and where more refined models have to be considered. For this purpose, we have fabricated a semiconductor model system where a parabolic potential profile is realized along one spatial direction in the conduction band of a semiconductor heterostructure. This parabolic quantum well was grown by molecular beam epitaxy of $\mathrm{Al}_x\mathrm{Ga}_{1-x}\mathrm{As}$ by varying x appropriately. Carriers in the well are provided by modulation-doping.

The magnetoresistance and Hall resistance of the electron gas confined in the well has been measured at temperatures down to 40 mK and magnetic fields up to 13 T. The energy of the 76 nm wide well was found to be quantized, leading to the formation of subbands. With gate electrodes on both sides of the well, the electron density in the quantum well has been varied and up to three subbands could be occupied. The electron sheet density could be tuned between 1 and $6 \cdot 10^{15}\,\mathrm{m}^{-2}$. By measuring Shubnikov-de Haas oscillations in the magnetoresistance, the individual subband densities have been determined.

With appropriate voltages applied to the gate electrodes, the electron gas could be displaced across the quantum well by ±15 nm, while the sheet density was kept constant. By growing a narrow potential spike of well-defined strength in the center of the parabolic quantum well, we have probed the difference in the squared wavefunction modulus between the two lowest subbands. The results agree with single-particle envelope wave functions calculated in the Hartree approximation.

Individual subband scattering times have been obtained from low-field magnetoresistance measurements. The scattering time of the subband lowest in energy depends mainly on the distance of the electron gas to the dopant layer, whereas the scattering

time of the upper subband is influenced by density-dependent screening effects. As suggested by a calculation of the intra- and intersubband scattering times, the electron mobility is limited by Coulomb scattering from ionized dopants on both sides of the well. The dependence of the scattering times on the position of the electron gas indicates a segregation of dopants on the substrate side towards the quantum well during sample growth.

The transition from one to two occupied subbands is of special interest, as a cross-over from two- to three-dimensional behavior is expected. From universal conductance fluctuations and the weak-localization correction to the magnetoresistance, the phase-coherence length can be extracted. Both, universal conductance fluctuations and weak-localization, indicate a change in the phase-coherence length at the dimensional cross-over.

The electron confinement due to a magnetic field oriented along arbitrary directions has been studied. For magnetic fields oriented in the plane of the electron gas, the electron densities of the upper subbands decrease with the magnetic field, and the subbands are successively depopulated. It has been found that the diamagnetic shift of the subband energy is not solely responsible for the electron redistribution. It is rather the change of the in-plane dispersion relation which leads to a subband-dependent change in the density of states and to a strong carrier redistribution. This effect has been calculated in second-order perturbation theory and quantitatively accounts for the measured effect.

The two-dimensional electron gas has been electrically confined in one lateral direction by lithographically fabricated split-gate electrodes. This forms a quantum point contact, where transverse modes in both directions can be occupied. We have found the conductance to be quantized, indicating ballistic transport through the quantum-point contact. A measurement of the conductance plateaus allows for spectroscopy of single-particle energy levels. A suppression of certain conductance plateaus has been observed, which we explain by degeneracies in the 1D subband energy structure. By applying a magnetic field in the direction of current flow, a coupling of the 1D subbands has been observed, which is described by a generalized Darwin-Fock spectrum. Level anticrossings have been explained by the non-parabolic confinement of the quantum point contact.

Zusammenfassung

Die Funktionsweise konventioneller Halbleiterbauteile kann mit Hilfe eines semiklassischen Modells des Elektronentransports verstanden werden. Für kleinere Strukturen mit Abmessungen vergleichbar der Fermiwellenlänge werden Quanteneffekte wichtig. Aufgrund der eingeschränkten Elektronenbewegung nehmen die Energien hier quantisierte Werte an. Mit der zunehmenden Miniaturisierung der Computerchips wird diese Grenze bald erreicht sein. Es ist deshalb von Interesse, wie man Elektronentransport in solchen Quantenstrukturen beschreiben kann. Mit modernen technologischen Verfahren ist es heute möglich, nanometergrosse Strukturen herzustellen, die auf atomare Monolagen genau zugeschnitten sind. Im Prinzip ist in solchen Strukturen das Lehrbuchbeispiel eines Teilchens in einem Quantentopf experimentell realisiert, nur dass wir es hier nicht mit einem abstrakten Quantentopf oder einem Atom zu tun haben, sondern immer noch mit Millionen von Atomen und Elektronen. In der vorliegenden Arbeit soll untersucht werden, inwiefern man solche Nanostrukturen dennoch als einfache Quantensysteme begreifen kann und wo erst kompliziertere Modelle ihre Funktionsweise erhellen können. Um dieses Ziel zu erreichen, wurde ein Modellsystem hergestellt, in welchem entlang einer Raumrichtung ein parabolförmiges Potential realisiert ist. Dieser parabolische Quantentopf wurde mittels Molekularstrahlepitaxie von $\mathrm{Al}_x\mathrm{Ga}_{1-x}\mathrm{As}$ gewachsen, wobei der Aluminiumgehalt x von Schicht zu Schicht entsprechend geändert wurde.

Das Elektronengas, das sich im modulationsdotierten Quantentopf aufhält, wurde elektrisch kontaktiert und dessen Widerstand sowie Hallwiderstand für Magnetfelder bis 13 T und Temperaturen bis 40 mK gemessen. Die Quantisierung der Energie im 76 nm breiten parabolförmigen Quantentopf führt zur Bildung von Subbändern. Mittels Elektroden, die auf beiden Seiten des Topfes angebracht wurden, konnte die Elektronendichte zwischen 1 und $6 \cdot 10^{15}\,\mathrm{m}^{-2}$ geändert werden. Durch Messungen von Shubnikov-de Haas Oszillationen des Magnetowiderstandes wurden die einzelnen Subbanddichten aufgelöst.

Indem geeignete Spannungen an die Elektroden angelegt wurden, konnte die Elektronenverteilung im Quantentopf bei konstanter Dichte um 15 nm hin- und hergeschoben werden. Mit Hilfe einer eingewachsenen Potentialspitze konnten wir die Differenz von Wellenfunktionsbetragsquadraten zweier Subbänder bestimmen. Die erhaltenen Messwerte stimmen gut mit berechneten Werten überein, welche wir mit der Hartree-Näherung erhalten haben.

Die Streuzeiten der einzelnen Subbänder wurden mittels Messung des Magnetowiderstandes bei kleinen Magnetfeldern bestimmt. Während die Streuzeit des energetisch tieferliegenden Subbandes hauptsächlich vom Abstand der Elektronenverteilung von

den Störstellen abhängt, ist die Streuzeit des höherliegenden Subbandes bestimmt durch Abschirmung, die mit der Subbanddichte zunimmt. Eine Berechnung zeigt, dass die Streuzeiten durch Coulomb-Steuung an ionisierten Donatoren limitiert sind. Die spezielle Abhängigkeit der Streuzeiten von der Position des Elektronengases im Quantentopf deutet darauf hin, dass während des Wachstums der Probe auf der Substratseite Donatoren in Richtung des Quantentopfes diffundiert sein könnten.

Der Übergang von einem zu zwei besetzten Subbändern ist besonders interessant, da er den Bereich zwischen einem zwei- und dreidimensionalen System kennzeichnet. Die Phasenkohärenzlänge kann in diesem Bereich durch Messungen universeller Leitwertfluktuationen und der Widerstandskorrektur aufgrund der Schwachen Lokalisierung studiert werden. Beide Grössen deuten auf einen Wechsel der Phasenkohärenzlänge am Übergang hin.

Das durch ein entlang einer beliebigen Richtung angelegte Magnetfeld erzeugte magnetoelektrische Potential wurde untersucht. Für Magnetfelder in der Ebene des Elektronengases beobachteten wir mit zunehmendem Magnetfeld eine Abnahme der Elektronendichte der höheren Subbänder. Diese Abnahme ist viel stärker, als aufgrund der diamagnetischen Verschiebung der Subbandenergien vermutet werden könnte. Es ist vielmehr die zusätzlich vom Magnetfeld bewirkte Änderung der Dispersionsbeziehung in der Ebene, die zu der starken Umverteilung der Ladungsträger zwischen den Subbändern führt. Dieser in Störungstheorie zweiter Ordnung berechnete Effekt erklärt die gemessenen Daten quantitativ.

Das Elektronengas wurde zusätzlich zum parabolförmigen Quantentopf in einer weiteren Raumrichtung eingeschnürt. Dies wurde mittels einer geteilten Elektrode bewerkstelligt. Der so entstandene Quantenpunktkontakt leitet transversale Moden beider Richtungen. Die gemessenen Leitwerte sind quantisiert, was auf ballistischen Transport im Punktkontakt hinweist. Das Ausmessen der Leitwertsplateaus ermöglicht die Spektroskopie der Einteilchenenergien im Punktkontakt. Gewisse Leitwertsplateaus sind unterdrückt, was wir mit einer Entartung von Modenenergien erklären. Wird ein Magnetfeld in Richtung des Stromes angelegt, beobachten wir eine Modenkopplung, welche in einem erweiterten Darwin-Fock-Modell erklärt werden kann. Nicht alle Modenenergien kreuzen sich mit zunehmendem Magnetfeld. Dass sich einige abstossen, wurde auf ein nichtparabolisches Einschlusspotential zurückgeführt.

List of abbreviations

Symbol	Explanation
a_{B}	Bohr radius
B	magnetic field
$B_{\parallel}$	parallel magnetic field
$B_{\perp}$	perpendicular magnetic field
ΔB	width of weak localization peak
ΔB_c	correlation field of universal conductance fluctuations
$\Delta\rho$	amplitude of Shubnikov-de Haas oscillations
$D_T(X)$	Dingle term, $D_T(X) = X/\sin X$
D	diffusion constant
e	electron charge
ϵ	dielectric permittivity
ϵ_0	vacuum dielectric constant
$\epsilon_{ij,lm}$	dielectric tensor
E	electric field
E_i	2D subband energy
$E_{l,m}$	1D subband energy
$F_{ij}(q, z_i)$	Form factor for the Coulomb potential
$F_{ij,lm}(q)$	another Form factor for the Coulomb potential
$\varphi_i(z)$	subband envelope wave function
ϕ	quantum mechanical phase of an electron
Φ	full electrostatic potential
Φ^{C}	scattering potential from Coulom scatterers
Φ^{A}	scattering potential from ternary alloy disorder
Φ^{IR}	scattering potential from interface roughness
Φ^{ext}	external electrostatic potential
G	conductance
δG	amplitude of conductance fluctations
$\hbar$	Planck's constant divided by 2π
I	current
j	current density
$\mathbf{k}$	wavenumber
$\mathbf{k}_{\parallel}$	in-plane wavenumber
k_{B}	Boltzmann constant
K_1, K_2 and K_3	coefficients of the two-subband scattering matrix
L	length of a sample
l_B	magnetic length
l_{el}	elastic scattering length
l_ϕ	phase-coherence length

continued...

continued from previous page

Symbol	Explanation
m	electron mass
m^*	effective electron mass, $m^* = 0.067m$ in GaAs.
n_{ind}	charge density induced by an external potential
n_{ext}	density of external charges
n	electron charge density
n_{H}	Hall density
n^{3D}	3D density
n_i	electron sheet density of subband i
N	number of states
P	electric polarization
$P_{ij}(\vartheta)$	transition rate from subband i to j with angle ϑ of momentum change
R	resistance
$\mathbf{r}$	spatial coordinate
$\mathbf{r}_{\parallel}$	in-plane spatial coordinate
r_{s}	mean spacing between electrons divided by the Bohr radius
ρ	density of states
ρ_i	density of states in subband i
ρ_{xx}	magnetoresistivity
ρ_{xy}	Hall resistance
σ_{xx} or σ	magnetoconductivity
$\Delta\sigma(B)$	weak-localization correction to the conductivity
$\Delta\sigma_0$	weak-localization correction at $B = 0$
σ_{xy}	Hall conductivity
T	temperature
τ_{el}	Drude scattering time
τ_i	Drude scattering time of subband i
τ_{s}	single-particle scattering time
τ_{ϕ}	phase-coherence time
$U(z)$	electric potential energy
U_{bg}	back gate voltage
U_{fg}	front gate voltage
U_{xc}	exchange potential
U_{H}	Hartree potential
U_{sc}	self-consistent potential
$v(\mathbf{r}, \mathbf{r}')$	Green's function of the Poisson equation
w	width of the parabolic quantum well
W	lateral width of a sample
x	Al-content of $\mathrm{Al}_x\mathrm{Ga}_{1-x}\mathrm{As}$
$\omega_c = eB/m^*$	cyclotron frequency
Ω	harmonic frequency of the parabolic quantum well

Abbreviation	Explanation
2DEG	two-dimensional electron gas
AFM	atomic force microscope
bg	back gate
DOS	density of states
DQW	double quantum well
fg	front gate
LL	Landau level
LDA	local density approximation
PQW	parabolic quantum well
QPC	quantum point contact
RPA	random phase approximation
SdH	Shubnikov-de Haas
sg	split gate

Chapter 1

Introduction

The progress in the fabrication of semiconductor structures of high purity has achieved a level where monoatomic layers of different materials can be grown on top of each other. Thereby the crystal lattice can be maintained to a very large extent. The synthesis of artificially quantized structures, in which the electrons move through a restricted, but almost defect-free crystalline lattice is therefore possible. In such small structures, the electrons experience quantum effects which strongly modify their behavior. Especially the investigation of an electron gas confined to a plane (a so-called two-dimensional electron gas, 2DEG) has lead to fundamental discoveries such as the integer quantum Hall effect, for which the 1985 Nobel prize was awarded. This effect, where the Hall resistance is quantized in integer fractions of a fundamental resistance unit, was first observed at the oxide-semiconductor interface in gated silicon [1], the material every microchip is made of. Although industry is focused on Si technology, basic research concentrates on the III/V compound GaAs, mainly for three reasons: (i) GaAs is a direct-bandgap semiconductor allowing for optical applications, (ii) a higher electron mobility is achieved due to a lower effective electron mass and the advantage of modulation doping [2, 3], and (iii) the combination of GaAs with AlGaAs ternary alloys allows the fabrication of almost defect-free interfaces between semiconductors with different physical properties, but almost identical lattice constants.

A high-mobility 2DEG is formed at the $\mathrm{Al}_x\mathrm{Ga}_{1-x}\mathrm{As}/\mathrm{GaAs}$ heterointerface if the structure is doped remotely. The spatial separation of the ionized dopants from the 2DEG is responsible for the high mobilities achieved in such structures. This paved the way for the discovery of a new kind of quasi-particles [4] which shows up in excitations of fractional-quantum Hall states [5] and carries a charge which is only a fraction of the electron charge (also worth a Nobel prize in 1998).

The AlGaAs system provided new kinds of optical and electronic devices [6]. New transistors based on 2DEGs are used in high-frequency applications, and quantum-well lasers operate in compact-disc players and are used in optical telecommunication.

The development goes to smaller and smaller structures ("nano-structures"). The additional confinement of the electrons leads to 1D ("wires") and 0D ("dots") devices. Today lithography allows for structure sizes with dimensions comparable to the Fermi wavelength (typically 40 nm in semiconductors) and much smaller than the electron mean-free path (several micrometers). In such quantized, "ballistic" systems, the transport properties are modified significantly, and electron-electron interactions become increasingly important. The Coulomb-blockade effect encountered in such systems has a possible application in the single-electron transistor [7].

While the fabrication of 1D and 0D structures has advanced considerably in recent years, much less effort has been undertaken in the direction of high-purity 3D systems. At the crossover from two to three dimensions, the quantum Hall effect breaks down. Electrons formerly captured in one vertical quantum state spread among additional states. Transitions between those states modify the electronic properties. In pure 3D electron gases, a condensation of the electrons into a 3D Wigner-crystal is predicted [8], but has never been clearly observed experimentally.

In order to realize 3D systems with high mobility, the dopants should be spatially separated from the electron gas, similar to a remotely doped heterointerface. Evidently no 3D system with infinite extensions can be realized with dopants located "outside". But quantum wells, wide enough for many energy levels to be occupied, offer the electrons quasi-free motion in the direction across the well. Such quasi-3D systems are preferably realized in a quantum well with parabolic potential shape (so-called parabolic quantum wells, PQW). Due to the interaction among the electrons, the effective potential in a PQW is flat, and the 3D electron density is uniform [9, 10].

The parabolic potential itself is of great interest, apart from this technological aspect (i.e. the realization of a high-mobility 3D electron gas). Parabolic potentials are of fundamental importance in physics. In general, motion of a mass around a potential minimum can be approximated by a harmonic oscillation, as long as the displacement from the equilibrium position is small enough. This is reflected in the Taylor expansion around the potential minimum, where the first non-zero term is quadratic in the displacement. Using this approximation, vibrations of molecules or of a crystal lattice are described.

In this thesis, a model system is investigated, where an artificial parabolic potential is provided for electrons in a semiconductor. The potential acts along one spatial direction, in the other two directions the electrons are free to move. The motion of electrons in the parabolic potential cannot be described classically. The allowed energies are quantized. Thus this system is perfectly suited for the investigation of quantum mechanical phenomena. Typical text-book problems of quantum mechanics in one, two and three dimensions involving potential wells and magnetic fields along arbitrary directions can be experimentally realized in the system considered.

The description of the electron states is not as simple as the text-book's examples might suggest. The parabolic well is realized in a semiconductor, and the potential of the periodic lattice can only be neglected in the approximation of the "envelope" wave function. If more than one electron sits inside the well, Coulomb repulsion between the electrons occurs. The exact quantum-mechanical calculation of the electron motion is a many-body problem, which cannot be solved analytically for more than a few electrons. Here, the single-electron approximation comes into play, where the motion of one electron in the averaged potential of all others is calculated. One aim of this thesis is to investigate experimentally, how far the measured effects can be explained within these approximations.

PQWs have attracted a lot of attention because they can be used for unique experiments inaccessible to other potential shapes. In optical transmission experiments, the equidistant energy levels of a bare parabolic potential are measured, as if there was no electron-electron interaction [11, 12]. This striking observation was explained by a generalization of Kohn's theorem [13] stating that in the bare parabolic well the absorption spectrum is independent of the electron-electron interaction, and also independent of the number of electrons in the well [14].

The parabola is the only mathematical function which maintains its shape if a linear function of arbitrary slope is added. This fact has useful consequences for the experiments with PQWs. The potential of the as-grown PQW is parabolic. A voltage applied to a plane gate near the PQW produces a linearly increasing potential. The sum of the two potentials is again a parabola with the same curvature, but with a displaced origin. We employ this fact in order to tune the spatial position of the electron gas in growth direction.

In this thesis, the PQW properties are investigated by transport measurements. The sample resistance in a magnetic field and the Hall effect reveal the electron population and scattering times of individual quantum states. From the electron population, conclusions on the single-particle energy levels can be drawn. The sample fabrication and the properties of the confined electron gas will be discussed in chapter 2.

We not only intended to probe the quantized energy levels, but also the corresponding wave functions. This is much more difficult than energy spectroscopy and usually requires the presence of a highly localized scattering center which is used as a wave-function probe. Such a sensor has been realized by enhancing the Al content of three monolayers in the center of the PQW. This way we have measured the quantum-mechanical electron probability density at the sensor position, and by displacing the electron gas relatively to the probe, the distribution of the probability density (chapter 3). This novel method allows scanning of the wave function within one single sample. The results agree with calculations of the single-particle wave functions.

The Si dopants on both sides of the quantum well limit the electron mobility. The electrons in the well are scattered by the ionized dopants. It is not clear how the dopants are distributed across the structure. Segregation of Si during growth might occur. We present a new method, where the influence of the dopant position on the electron gas can be investigated. By varying the position of the electron gas, we have a unique means of probing the distribution of the remote scatterers. We have investigated in detail the dependence of the electron scattering times on the electron-gas position across the quantum well (chapter 4).

With gate voltages, not only the position of the electron gas along the growth direction can be tuned, but also the electron sheet density. At low densities, only the PQW ground state is occupied, and the system has a pure 2D character. With the occupation of upper PQW states, a transition to a quasi-3D system can be realized. It is of particular interest to study the electron-electron scattering rate at this transition. Electron-electron scattering leads to a decrease of the electron phase-coherence length, which has been studied by measuring fluctuations and the weak-localization peak in the sample resistance. We have observed characteristic changes of those features at the transition, which will be discussed in chapter 5.

The PQW is a "text-book system", which can be studied with magnetic fields applied along arbitrary directions. An in-plane magnetic field leads to a diamagnetic shift of the energy levels, and in addition, the in-plane dispersion relation is modified. In order to describe the experimental results, the change in the dispersion relation was usually neglected. We have showed that for a PQW system this effect is crucial for describing the measured effects (chapter 6).

The PQW represents a system where a quasi 3DEG is realized. Given that, we can go back and reduce the dimensionality. We realized a quantum point contact (QPC) by laterally confining the electron gas. This device differs significantly from one fabricated conventionally at a semiconductor hetereointerface. The QPC defined on a PQW can be tuned in both lateral directions (one defined vertically by the PQW, the other laterally by lithography), and the occupied states are described by two quantum numbers. The QPC resembles an optical waveguide, transmitting electrons instead of photons. One interesting question is what happens in a magnetic field. Because photons have no charge, no mode coupling can occur, whereas in an electron waveguide the magnetic field leads to mode coupling which changes the energy spectrum significantly.

The measured conductance through the QPC shows plateaus which are at integer multiples of the fundamental conductance unit given by $2e^2/h$. The position of the conductance plateaus and their suppression at certain parameter values have revealed the quantum-mechanical single-particle spectrum in the two-dimensional constriction and its dependence on a magnetic field (chapter 7).

Chapter 2

Sample Fabrication and Characterization

2.1 AlGaAs System

The two semiconductors AlAs and GaAs both consist of atoms arranged in a zinc-blende lattice with very similar lattice constants[1]. This makes it easy to grow the two materials epitaxially on top of each other with negligible strain between the layers and minimal lattice mismatch. With current epitaxial growth techniques like molecular beam epitaxy (MBE), layer thickness and layer composition can be controlled perfectly. The layer smoothness reaches the atomic level.

This way monoatomic layers of the ternary compound $\mathrm{Al}_x\mathrm{Ga}_{1-x}\mathrm{As}$ can be grown, where the ratio of Ga and Al determines the physical properties of the semiconductor. AlAs has a larger band gap than GaAs. In the ternary compound with Al-content x, the band gap varies linearly with x for $0 < x < 0.4$. If two ternaries with different Al-content x are brought together, the difference in the band gap is distributed between the conductance and valence band offsets. Semiconductor quantum wells are generally realized in $\mathrm{Al}_x\mathrm{Ga}_{1-x}\mathrm{As}$/GaAs heterojunctions, where the two materials $\mathrm{Al}_x\mathrm{Ga}_{1-x}\mathrm{As}$ and GaAs are brought together at an atomically flat interface. An n-doped layer in $\mathrm{Al}_x\mathrm{Ga}_{1-x}\mathrm{As}$ provides electrons, which 'fall' into the energetically lower GaAs region. There they are confined to the interface by the attractive electrostatic potential of the positively charged ionized donors remaining in the $\mathrm{Al}_x\mathrm{Ga}_{1-x}\mathrm{As}$ region. The effective potential for the electrons at the GaAs-$\mathrm{Al}_x\mathrm{Ga}_{1-x}\mathrm{As}$ interface has the shape of a triangle.

Arbitrary potential shapes can be realized in structures where x is varied continuously from layer to layer in growth direction. The spatial variation of the conductance band edge amounts to 79 meV per 10 percent of Al [16].

---

[1] At 300 K, GaAs has a lattice constant of 5.6533 Å, while that of AlAs is 5.6605 Å [15]

2.2 Samples

In section 2.2.1, the vertical structure of the samples is discussed. This includes the parabolic well, spacer layers, doping layers and a gate electrode on the back side of the well. The processing of the lateral structure as well as the ohmic contacts to the 2DEG are described in section 2.2.2. Finally, we briefly discuss the measurement set-up in section 2.2.3.

2.2.1 Layer Sequence

In this thesis, a series of samples has been investigated with a design as schematically shown in Fig 2.1. The wafers were grown by MBE at the University of California in Santa Barbara[2]. The samples are realized by growing layers of $Al_xGa_{1-x}As$ on a GaAs wafer. Thereby the conduction-band edge is modified along the growth direction, i.e., perpendicular to the wafer surface.

The shape of the well was achieved by a digital alloy technique [17]. In this approach, a superlattice as shown in Fig.2.2 with variable amount of Al in each period is grown. Within 760 Å, the spatially averaged Al-content x varies parabolically between 0 and 0.1. At $x = 0.1$, a conduction band offset of 79 meV is assumed, based on established experimental data. With a parabolic potential given by $U(z) = m^*\Omega^2 z^2/2$, this corresponds to an oscillator frequency of $\Omega = 1.68 \cdot 10^{13}\,\mathrm{s}^{-1}$ and an energy separation of $\hbar\Omega = 11.0\,\mathrm{meV}$. Similar samples have been investigated in transport[18, 19], by capacitance measurements[20] and by optical experiments [21].

The well is embedded between 200 Å of undoped $Al_{0.3}Ga_{0.7}As$ spacer layers with remote Si-doping on both sides, providing electrons which accumulate in the well. On the surface side, the dopants are provided by 11 sheets, each with a Si donor density of nominally $5{\cdot}10^{15}\,\mathrm{m}^{-2}$ Si-concentration, arranged in a 200 Å thick layer. On the back side, the dopants are located within one δ-doping layer with a concentration of $5{\cdot}10^{15}\,\mathrm{m}^{-2}$. This asymmetry in the doping allows for saturation of the surface states and an effectively symmetric location of the electron distribution in the well.

A back gate electrode consisting of a 250 Å thick n^+-doped layer is located 1.35 μm below the well. In order to enhance the electric isolation to the electron gas, the back gate is separated from the PQW by 0.5 μm of low-temperature grown GaAs [22]. A front-gate electrode was realized by evaporation of TiPtAu on top of the structure. By applying voltages U_{fg} and U_{bg} to the front- and back gates, the carrier density and the position of the electron distribution inside the well can be tuned independently (chapter 2.6).

The description given above considers only the essential features of the sample layout. A lot of other finesses had to be considered in order to fabricate perfect samples. For a review of growth and experiments on wide graded quantum wells see Ref. [16] and the PhD thesis of Hopkins [23].

---

[2] The wafers were grown by K. Maranowski on 11/17/96 and 10/27/94. For an overview of the processed wafers, see appendix C.

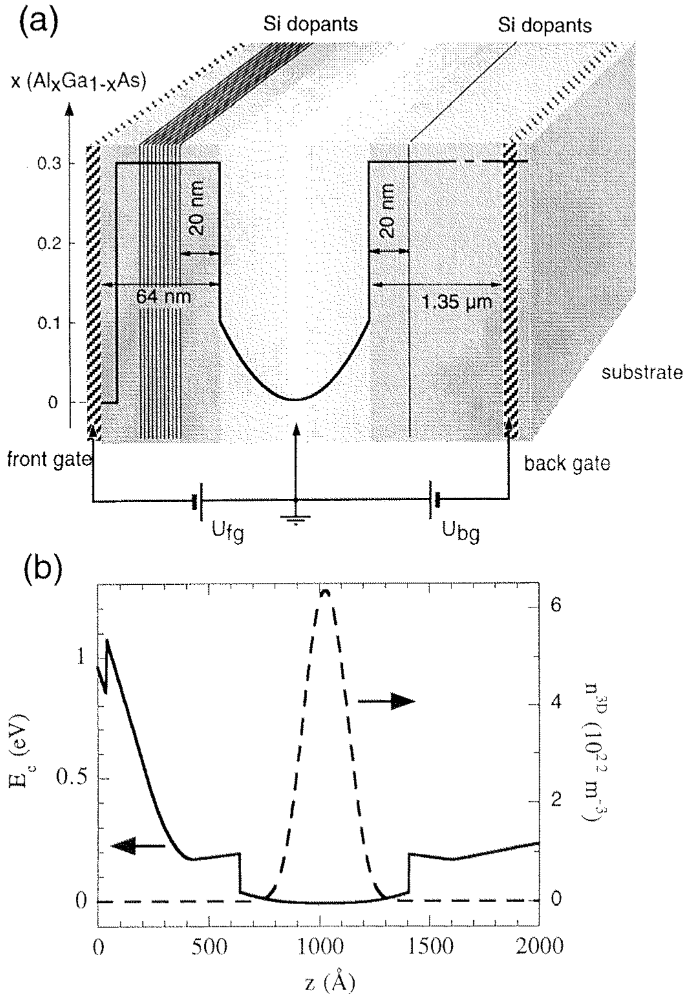

Figure 2.1: (a) Schematic sample layout (not to scale) showing the Al concentration along the growth direction and the donor layers. Voltages can be applied to the metal front gate electrode and the buried n$^+$-doped back gate electrode.
(b) Self-consistently calculated conductance band profile along the growth direction z and 3D electron density n^{3D} for $U_{\mathrm{fg}} = -360\,\mathrm{mV}$ and $U_{\mathrm{bg}} = -1000\,\mathrm{mV}$.

2.2.2 Optical Lithography and Ohmic Contacts

After the MBE growth of the PQW and the cap layers, one has a 2DEG which extends laterally over the whole wafer. The transport properties of the 2DEG can be measured in a Hall-bar structure (Fig. 2.3), which is connected electrically. Also an ohmic contact to the back gate has to be realized. In the following we explain how these steps are performed.

The processes involved in the fabrication of the Hall bar mesa are schematically explained in Fig. 2.4A. Conventional photolithographic techniques used in our lab allow etching and metallization of micron-sized structures. A 500 nm thick photoresist is spun onto the sample surface. The structure is transferred to the photoresist by exposure through a photomask using UV light. A subsequent development of the resist locally removes the photoresist. In the next step, the sample is either etched (typically 80 nm deep to remove the 2DEG) or covered by a metallic film. We can reliably fabricate structures as small as 2μm with this technique. Industrial processes can go much smaller, actually 0.25μm are routinely achieved in today's chip fabrication – a next chip generation will be realized with 0.18μm-technology. For structures smaller than 2μm we used electron-beam lithography. With this technique, the UV light source and the mask are replaced by a focussed electron beam, which is

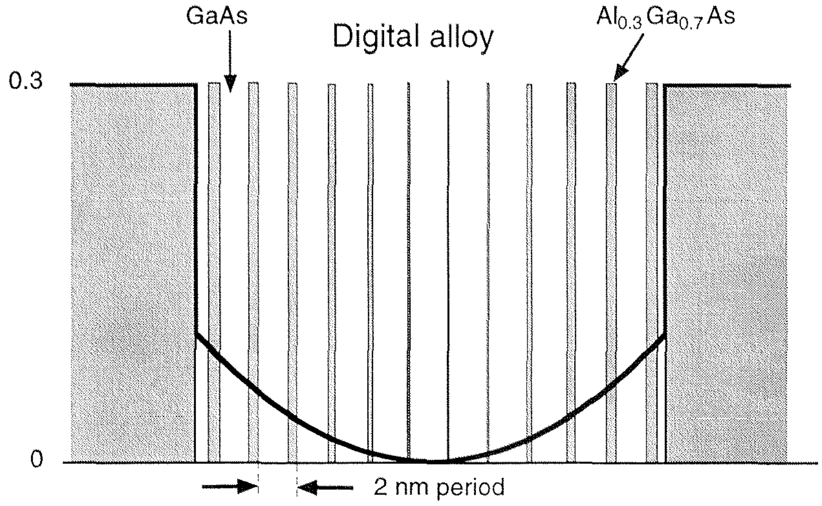
GaAs
Digital alloy
$Al_{0.3}Ga_{0.7}As$
0.3
0
2 nm period

Figure 2.2: Parabolic quantum well with digital alloy: Exact and averaged Al density profile x. The well consistst of a superlattice with a period of 2 nm but variable amount of Al in each period.

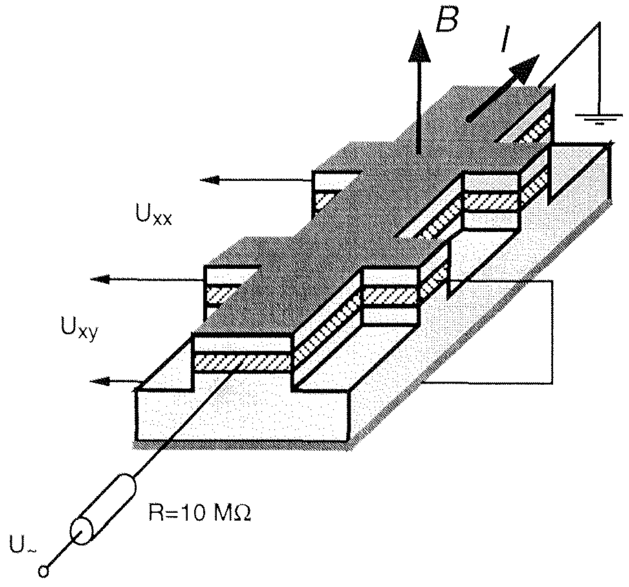
B
I
Uxx
Uxy
R=10 MΩ
U~

Figure 2.3: Schematic Hall bar and measurement set-up. A current I flows through the Hall bar via a resistance R, the voltage U_{xx} is measured on voltage probes on one side, the Hall voltage U_{xy} on opposite sides. A magnetic field B is usually applied in a direction perpendicular to the 2DEG.

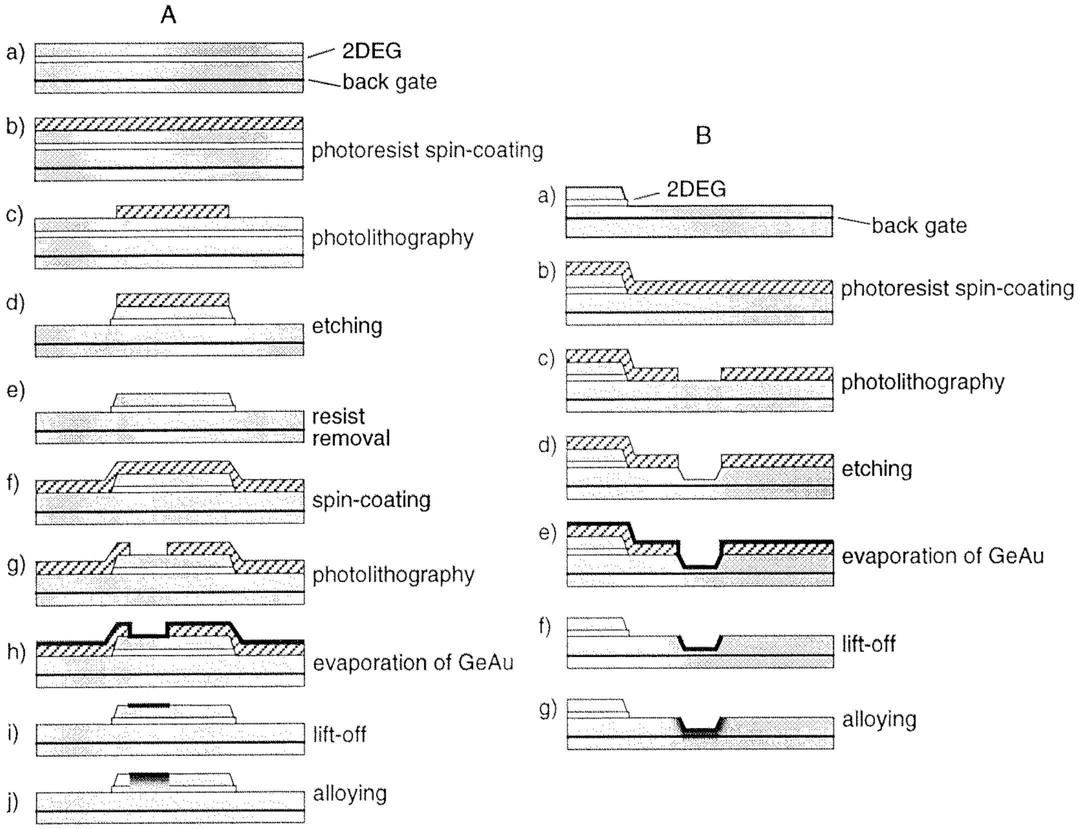
A
a)
2DEG
back gate
b)
photoresist spin-coating
c)
photolithography
d)
etching
e)
resist removal
f)
spin-coating
g)
photolithography
h)
evaporation of GeAu
i)
lift-off
j)
alloying
B
a)
2DEG
back gate
b)
photoresist spin-coating
c)
photolithography
d)
etching
e)
evaporation of GeAu
f)
lift-off
g)
alloying

Figure 2.4: A: Processing steps of the etching and contacting of a piece of 2DEG. B: Contacting the back gate.

positioned on the sample surface by deflection through magnetic coils. Thin Hall bars fabricated for conductance fluctuation measurements (chapter 5.3) and the split gate electrodes defining a quantum point contact (chapter 7) are examples for structures defined by electron-beam lithography.

The 2DEG is contacted by evaporation of the eutectic GeAu alloy with a mass ratio of Ge:Au=12:88. We have grown four layers in the sequence Ge, Au, Ge, Au with layer thicknesses of 18 nm, 50 nm, 18 nm and 50 nm, respectively. On top a 40 nm thick Ni layer serves as a diffusion barrier, and finally 100 nm of Au allows for contacting the pad with bond wires. After evaporation and lift-off, the samples have been alloyed for one minute at a temperature of 400°C at reduced pressure of 50 mbar in a N_2 atmosphere with 5 % of H_2.

This step melts the GeAu alloy, which diffuses into the GaAs and contacts the 2DEG layer. The details of this process are not completely understood [24], but lead to reproducibly functioning contacts.

The back gate electrode is more difficult to contact, because it is buried 1.4 μm below the surface, and the low-temperature grown GaAs layer seems to hinder the diffusion of the GeAu alloy. An etching step has to precede the evaporation of the eutectic. We used a mixture of H_2O_2:H_2SO_4:$H_2O = 3:3:50$, which etches approximately 1.4μm in 3 minutes. Figure 2.4B schematically summarizes the steps involved.

Figure 2.5a shows the photograph of a sample structure realized on a PQW. In

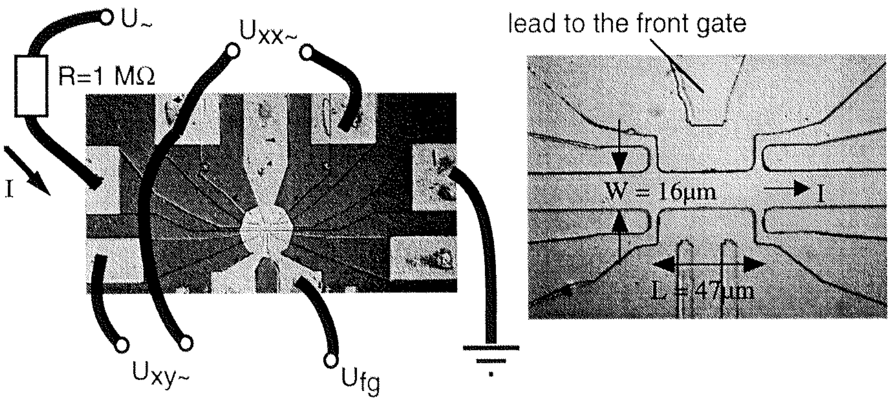

Figure 2.5: (a) Photograph of Hall bar defined with optical lithography. The current I flows along the Hall bar. The Hall resistivity ρ_{xy} is measured across the voltage probes, the longitudinal resistivity ρ_{xx} along the Hall bar. (b) Geometry of the measured part of the Hall bar.

Fig. 2.5b, an enlargement of the 16 μm wide Hall bar region is shown. The fingers (two coming from above and one from below) are metallic leads to TiAu front gates, which are evaporated in a last step (visible in Fig. 2.5a).

2.2.3 Measurement Set-Up

Two voltage probes on each side of the Hall bar allow a four-point measurement of the voltage drop U_{xx} along the direction of current flow I and the Hall voltage U_{xy} in perpendicular (Fig. 2.3). The current I has been generated by applying an oscillating voltage of typically 100 mV via a resistor of $R = 10\,\mathrm{M}\Omega$ to one side of the Hall bar, and grounding the other side. Because the sample resistance is much smaller than R, the current is given by $I = U/R$ which is typically 10 nA. A very low frequency of the current has been chosen (typically 13 Hz), such that capacitive and inductive signals can be neglected. The voltages U_{xx} and U_{xy} are measured by Lock-In amplifiers.

A voltage U_{fg} has been applied between the front-gate electrode and the grounded electron gas (Fig. 2.5a). Similarly, a voltage U_{bg} has been applied between the back-gate electrode and ground.

The resistivity ρ_{xx} is given by $\rho_{xx} = WU_{xx}/LI$, where W is the width of the Hall bar and L then length between two voltage probes. The Hall resistivity is given by $\rho_{xy} = U_{xy}/I$.

2.3 The PQW as a Quasi-3D System

As mentioned above, PQWs have been proposed in order to realize high-mobility 3D electron systems [8]. In a 2DEG, the electrons can be separated spatially from the ionized donors (Fig.2.6a). This reduces Coulomb scattering and thus greatly improves the electron mobility compared to a bulk doped material. It is evident that such a modulation doping [2, 3] is not applicable to an electron system which extends infinitely in all three dimensions. Nevertheless a quasi-3D system can be realized which has two free dimensions and a confinement in the third dimension. If the confinement width is large compared to the Fermi wave length, several QW states can be occupied and motion across the well is possible. In such a structure, the dopants can be located outside the quasi-3D electron gas.

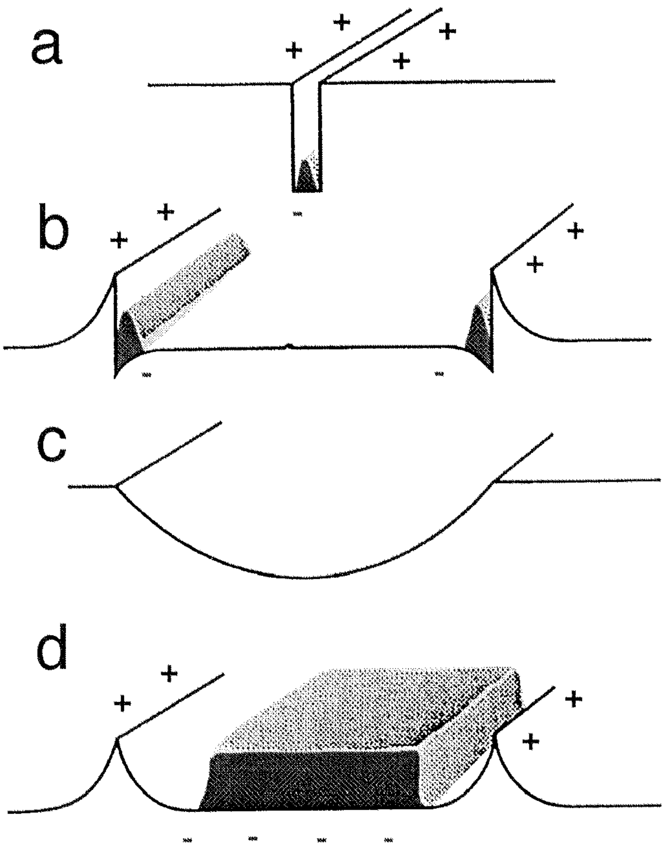

Figure 2.6: Realization of a modulation doped 3D system: (a) In a narrow quantum well only one energy level is occupied by electrons, the system has 2D character. (b) In a wide rectangular quantum well, Coulomb repulsion between electrons leads to accumulation of the electrons on both sides of the well. However, a parabolic potential (c) transforms to a rectangular potential (d), if electron-electron interactions are included. This leads to a wide electron layer with homogeneous 3D electron density.

Figure 2.6b shows what happens if a wide square well potential is filled with electrons: The Coulomb interaction separates the electrons into two narrow regions with 2D character. The self-consistent potential on each side is equivalent to the triangular-shaped conductance band in a heterojunction. Only if the potential is parabolic (Fig.2.6c), these difficulties can be overcome. A parabolic potential can be thought of as being composed of a homogeneous slab of a positively charged background with density n^{3D} (Fig. 2.7). This can be made clear if one considers the Poisson equation $d^2U(z)/dz^2 = e^2 n^{3D}/\epsilon\epsilon_0$. The curvature of the parabolic potential $U(z)$ is proportional to the positive 3D density. The electrons try to compensate this charge and start to fill in the minimum of the potential. Each (imagined) positive charge is compensated by an electron. Thus the electrons will arrange themselves in a slab with a uniform 3D density equal to n^{3D}. The width of the electron slab is n^{3D}/n_{H}, where n_{H} is the density of electrons per area (Fig.2.6d). With $U(z) = m^*\Omega^2 z^2/2$, one obtains the effective electron density $n^{3D} = \epsilon\epsilon_0 m^*\Omega^2/e^2$, which amounts to $7.8 \cdot 10^{22}\,\mathrm{m}^{-3}$ for $\Omega = 1.68 \cdot 10^{13}\,\mathrm{s}^{-1}$. The frequency Ω of the PQW is the plasma-frequency of the 3D

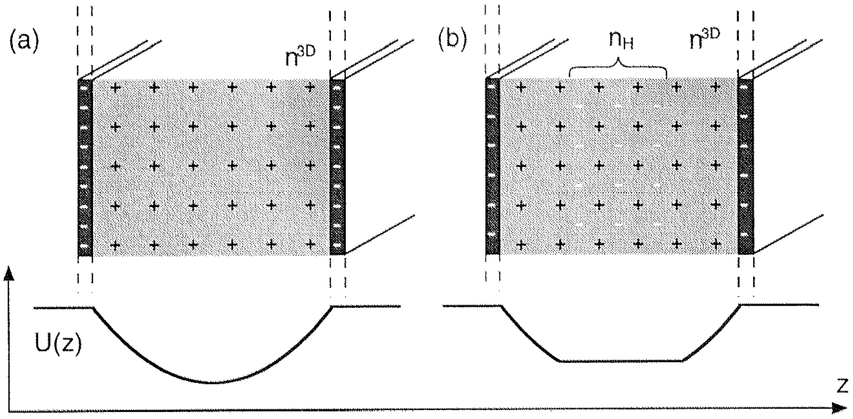

Figure 2.7: (a) A slab of homogeneous positive charge n^{3D} produces a parabolic potential $U(z)$ due to the Poisson equation $d^2U(z)/dz^2 = e^2n^{3D}/\epsilon\epsilon_0$. The negative surface charge forming the boundary of the slab gives rise to a flat potential outside the slab, if the total negative charge compensates the positive charge. (b) Electrons in the well try to compensate the positive charge, resulting in a flat potential bottom.

electron gas.

2.4 Electron States

In this section, the quantum mechanical description of the electron states in the PQW is summarized. Before we start to calculate the single-particle electron wave function and energy levels, we clarify the relation between the Bloch wave functions of electrons in a periodic potential and the envelope wave functions describing the bound states of the PQW (section 2.4.1). In order to calculate the envelope wave functions, electron-electron interactions cannot be neglected. In a self-consistent way, the Hartree energy and exchange interactions in the local density approach (LDA) are taken into account. Section 2.4.2 presents such self-consistently calculated envelope wave functions and energy levels for a PQW.

2.4.1 Bloch Wave Functions

The electrons in the valence band of a homogeneous semiconductor without any lattice perturbations are described by the Schrödinger equation

$$\left(\frac{\mathbf{p}^2}{2m} + V(\mathbf{r})\right)\psi_{\mathbf{k}} = E_{\mathbf{k}}\psi_{\mathbf{k}}. \tag{2.1}$$

Here m denotes the electron mass, $\mathbf{p}$ the momentum operator, and $V(\mathbf{r})$ is the periodic lattice potential. The electron wave function $\psi_{\mathbf{k}}$ can be written as

$$\psi_{\mathbf{k}}(\mathbf{r}) = e^{i\mathbf{k}\mathbf{r}}u_{\mathbf{k}}(\mathbf{r}), \tag{2.2}$$

where $u_{\mathbf{k}}(\mathbf{r})$ satisfies the Bloch condition $u_{\mathbf{k}}(\mathbf{r}+\mathbf{R}) = u_{\mathbf{k}}(\mathbf{r})$, with $\mathbf{R}$ a lattice vector. Then $\psi_{\mathbf{k}}$ oscillates with the periodicity of the lattice. A perturbation as induced by replacing some Ga atoms by Al adds a new term to Eq. 2.1. The complicated problem of solving the motion of an electron in a perturbed periodic potential can be simplified if the perturbation varies slowly on the length scale of the lattice period. A theorem by Slater, Luttinger and Kohn [25, 26] states that such an extra potential $U(\mathbf{r})$ can be treated as

$$\left(\frac{\hbar^2}{2m^*}\Delta + U(\mathbf{r})\right)\varphi_i(\mathbf{r}) = E_i\varphi_i(\mathbf{r}), \tag{2.3}$$

where m^* is the effective mass, which contains the effect of the lattice potential, and $\varphi_i(\mathbf{r})$ denotes the "envelope" wave function. By means of this theorem, the problem of electrons in a periodic lattice and an additional perturbing potential is reduced to the problem of free electrons in the perturbing potential. The envelope wave functions $\varphi_i(\mathbf{r})$ are related to the wave functions $\Psi_i(\mathbf{r})$ of the full problem by

$$\Psi_i(\mathbf{r}) = \sum_n \varphi_i(\mathbf{R}_n)a(\mathbf{r}-\mathbf{R}_n). \tag{2.4}$$

The sum is over all lattice vectors $\mathbf{R}_n$. Here we have introduced the Wannier functions $a(\mathbf{r})$, defined by

$$a(\mathbf{r}-\mathbf{R}_n) = N^{-\frac{1}{2}}\sum_{\mathbf{k}} e^{-i\mathbf{k}\mathbf{R}_n}\psi_{\mathbf{k}}(\mathbf{r}). \tag{2.5}$$

In a magnetic field the problem to find the wave functions can be simplified in the same way. With the vector potential $\mathbf{A}$, the Schrödinger equation for the envelope wave function is [27]

$$\left[\frac{1}{2m^*}\left(\frac{\hbar}{i}\nabla - e\mathbf{A}(r)\right)^2 + U(\mathbf{r})\right]\varphi_i(\mathbf{r}) = E_i\varphi_i(\mathbf{r}). \tag{2.6}$$

In the following we refer to the envelope wave functions $\varphi_i(\mathbf{r})$ as the wave function of the potential well. In the next section, we present a calculation of these wave functions and the corresponding energy levels for the electrons in a PQW without a magnetic field. The presence of a magnetic field B gives rise to an additional confinement of the electrons. The case where B is oriented perpendicular to the electron gas is of special importance, because the quantization of the in-plane motion into Landau levels significantly modifies the resistance. This effect is discussed in section 2.5.2.

2.4.2 Self-Consistent Calculation of the Electron States

In the case of a parabolic confinement $U(z) = \frac{m^*}{2}\Omega^2 z^2$, the Schrödinger equation is given by

$$-\frac{\hbar^2}{2m^*}\frac{d^2\varphi_i(z)}{dz^2} + U_{\mathrm{sc}}(z)\varphi_i(z) = E_i\varphi_i(z) \tag{2.7}$$

where $U_{\rm sc}(z) = \frac{m^*}{2}\Omega^2 z^2 + U_{\rm H}(z) + U_{\rm xc}(z)$ is the effective confinement potential, which is composed of a sum of the parabolic conduction band profile, the Hartree potential $U_{\rm H}(z)$ and the exchange-correlation potential $U_{\rm xc}(z)$. Without any electrons inside the PQW, $U_{\rm sc}(z)$ is a parabola and the energy levels are given by

$$E_{i,k_{||}} = \hbar\Omega\left(i + \frac{1}{2}\right) + \frac{\hbar^2 k_{||}^2}{2m^*}. \tag{2.8}$$

An electron state $E_{i,k_{||}}$ is defined by the wave number $k_{||}$ of the free in-plane motion and the quantized energy $E_i = \hbar\Omega(i + 1/2)$ in z-direction. E_i is usually called the subband energy. It defines the lower edge of the subband i, which can be filled with electrons free to move in the x- and y-direction with the same dispersion as the Bloch electrons of the unperturbed semiconductor. The number of electrons in subband i is related to the Fermi energy $E_{\rm F}$ by

$$n_i = \int_{E_i}^{E_{\rm F}} \rho(E) dE. \tag{2.9}$$

$\rho(E)$ is the two-dimensional density of states, which is independent of E:

$$\rho = \frac{m^*}{\pi\hbar^2}. \tag{2.10}$$

In the expression above a twofold degeneracy for each level was assumed, accounting for the electron spin. Because ρ does not depend on the energy, n_i is simply proportional to the difference between the Fermi energy and the subband bottom:

$$n_i = (E_{\rm F} - E_i)\frac{m^*}{\pi\hbar^2}. \tag{2.11}$$

If the PQW contains many electrons, electron-electron interactions have to be considered. The Hartree potential accounts for the electrostatic interaction of the electrons with themselves and with ionized impurities. It is determined by the Poisson equation:

$$\frac{d^2 U_{\rm H}}{dz^2} = \frac{e^2}{\epsilon\epsilon_0}\left[n_e(z) - n_D(z)\right], \tag{2.12}$$

where $n_e(z)$ is the electron concentration and n_D the concentration of ionized impurities. The distribution of the electrons is obtained from

$$n_e(z) = \sum_i n_i |\varphi_i(z)|^2. \tag{2.13}$$

The total electron sheet density $n_{\rm H}$ is given by

$$n_{\rm H} = \int dz\, n_e(z) = \sum_i n_i. \tag{2.14}$$

The exchange-correlation potential $U_{\rm xc}(z)$ can always be written as a functional of the local electron density[3] [28, 29]. The problem is to find the correct functional.

---

[3] a discovery which was awarded by the Nobel prize in Chemistry in 1998.

This is the so-called local density approximation (LDA). One possible form is given by [30]

$$U_{\mathrm{xc}}(z) = -\frac{1.69meV}{r_s}\left[1 + 0.0545\ln\left(1 + \frac{11.4}{r_s}\right)\right], \tag{2.15}$$

where $r_s = (4\pi n^{3D}(z)/3)^{-1/3}/a_B$ is the ratio of the mean electron spacing to the Bohr radius $a_B = 4\pi\epsilon\epsilon_0\hbar^2/m^*e^2$. For GaAs, $a_B \approx 100\,\mathrm{\AA}$, and r_s is about 1.5 for the 3D densities observed in the PQW. Note that r_s is a measure for the average interaction energy divided by the average kinetic energy of an electron. A value of $r_s \ll 1$ means small interaction energy, and the Hartree approximation is appropriate. On the other hand, for $r_s \gg 1$ exchange and correlation effects play an important role which can be accounted for in the LDA.

The energy levels, wave functions and $U_{\mathrm{sc}}(z)$ have to be determined self-consistently from Eqs. 2.7, 2.12 and 2.15. Figure 2.8 shows such self-consistent calculation[4] for a PQW sample [31, 32]. We chose $U_{\mathrm{bg}} = 0$ and varied U_{fg}. Three values of U_{fg} corresponding to three different sheet densities n_{H} are shown. From top to bottom, one, two and three subbands are occupied. While the back side of the well remains essentially unaffected by the front gate voltage, the self-consistent potential spreads out towards the front gate with increasing U_{fg}. One also observes the flat bottom of the self-consistent potential, indicating an almost homogeneous electron density.

A point of interest is the variation of the energy levels with the gate voltage. Figure 2.9 shows subband densities calculated without the exchange-correlation potential (lines) and taking exchange-correlation potential into account in the LDA (dashed). For the considered PQW, exchange and correlations are small corrections to the subband energies, except at the threshold where a new subband gets populated, where the LDA potential slightly enhances the subband energy difference. Such an exchange-enhancement has been observed experimentally in a two-subband system using capacitive measurements [33].

2.5 Transport

Resistance measurements not only provide the resistivity ρ_{xx}, but virtually all relevant properties of the electron gas under investigation (in the following the more general term "transport measurements" stands for resistivity measurements).

The elastic scattering time τ and the electron sheet density n_{H} are directly obtained from measured ρ_{xx} and ρ_{xy} in a magnetic field B:

$$\rho_{xy}(B) = \frac{eB}{n_{\mathrm{H}}} \tag{2.16}$$

$$\rho_{xx}(B=0) = \frac{m^*}{n_{\mathrm{H}}e^2\tau} \tag{2.17}$$

---

[4] We used a one-dimensional Schrödinger and Poisson solver written by G. Snider. The software is freely accessible on the internet on http://www.nd.edu/~gsnider

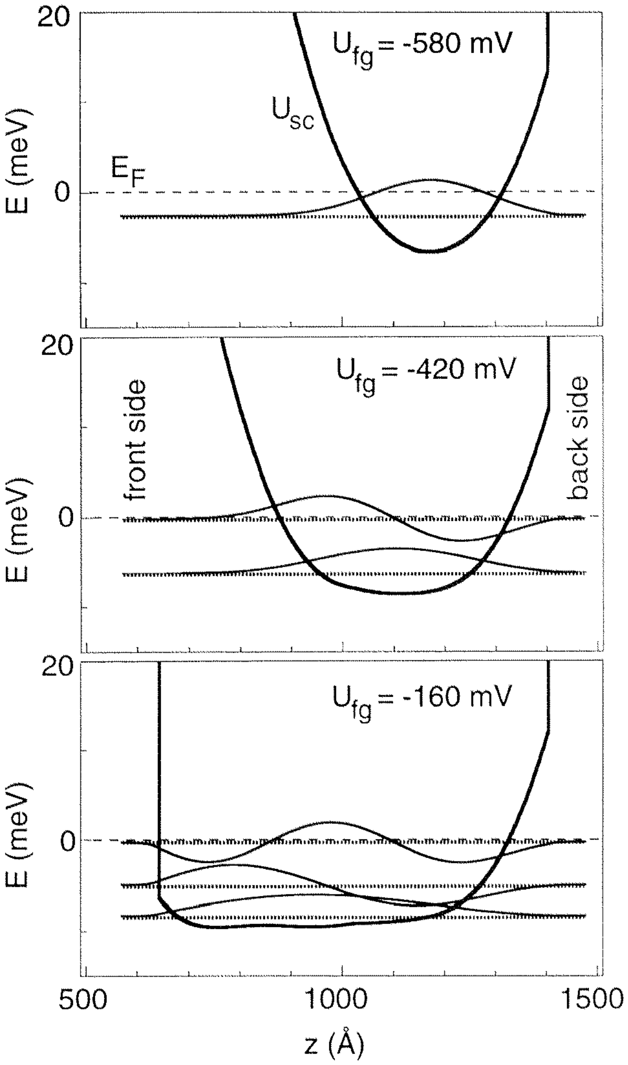

Figure 2.8: Self-consistent calculation of the conductance band profile $U_{sc}(z)$ relative to the Fermi energy (dashed), the subband energies and the subband wave functions for one, two and three occupied subbands. $z = 0$ corresponds to the sample surface. See text for details.

At low temperatures and in higher magnetic fields (section 2.5.1), the quantum nature of the energy spectrum modifies the resistivity due to the distribution of electrons on different subbands. For a magnetic field applied along the z-direction, ρ_{xx} oscillates as a function of $1/B$. These so-called Shubnikov-de Haas (SdH) oscillations are a direct consequence of the quantization of electronic orbits in a magnetic field. Analyzing the frequencies of SdH oscillations, the distribution of the electrons on different electric subbands and the individual subband densities are resolved. From the subband densities information on the energy spectrum is obtained. That way transport experiments make it possible to measure energy levels in mesoscopic systems. Section 2.5.2 describes the theory of SdH oscillations and how energy spectroscopy is realized.

2.5.1 Low Temperature, Magnetic Fields

Typical energies in mesoscopic systems (as the spacing between energy levels due to electric or magnetic confinement) are in the range of μeV to some meV. For quantum effects to manifest themselves in properties of the electron gas, the thermal broad-

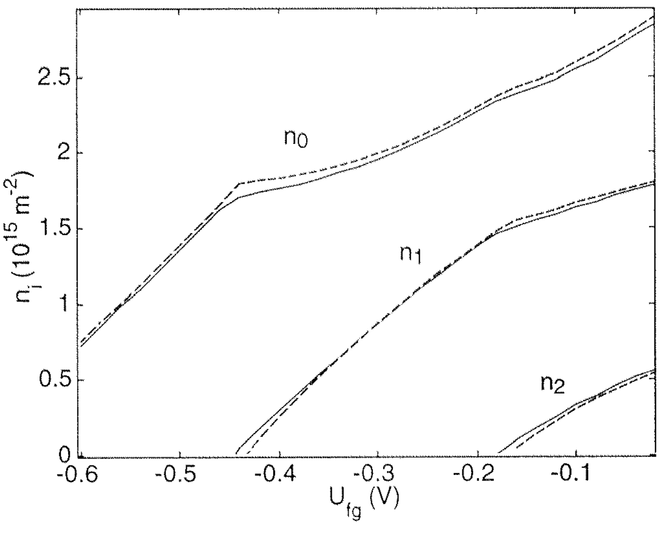

Figure 2.9: Self-consistent calculation of the subband electron densities in a PQW with a weak spike (Al-content x=0.05) and $U_{\mathrm{bg}} = 0$, considering exchange and correlation in the LDA (dashed) and without such corrections (lines).

ening kT of the Fermi distribution has to be smaller than those energies. At liquid Helium temperature $T = 4.2\,\mathrm{K}$, $k_{\mathrm{B}}T = 0.36\,\mathrm{meV}$. Sometimes a dilution refrigerator has to be used in order to cool the sample to 50 mK, where $k_{\mathrm{B}}T = 4.3\mu\mathrm{eV}$. For realistic applications of quantum effects, the envisioned devices should operate at room temperatures. This means that the energy spacing should be larger than 26 meV. In order to achieve this, the barrier height must be increased and the lateral dimensions have to be in the nanometer range:

Typical energy level spacings ΔE of potential wells of width w are found to be $\Delta E \approx \hbar^2/m^*w^2$. For electrons in GaAs this energy is 0.11 meV for $w = 100\,\mathrm{nm}$. In order to increase this energy to $k_{\mathrm{B}}T$ at room temperature, structures as small as 10 nm are required.

At higher temperatures, upper subbands in a 2DEG are thermally occupied due to the large value of $k_{\mathrm{B}}T$. Multi-subband effects, as investigated here for PQWs at liquid helium temperatures, become important.

2.5.2 Shubnikov-de Haas Oscillations

While the density of states (DOS) of a 3D system is proportional to the square root of the energy, it is energy-independent in a 2D system. For $B = 0$, the 2D DOS is given by Eq. 2.10. We consider a configuration where a magnetic field B is applied perpendicular to the plane of the 2DEG. The solution to the Schrödinger equation 2.6 are discrete Landau levels (LL) with energies E_l given by $\hbar\omega_c(l + 1/2)$, where ω_c

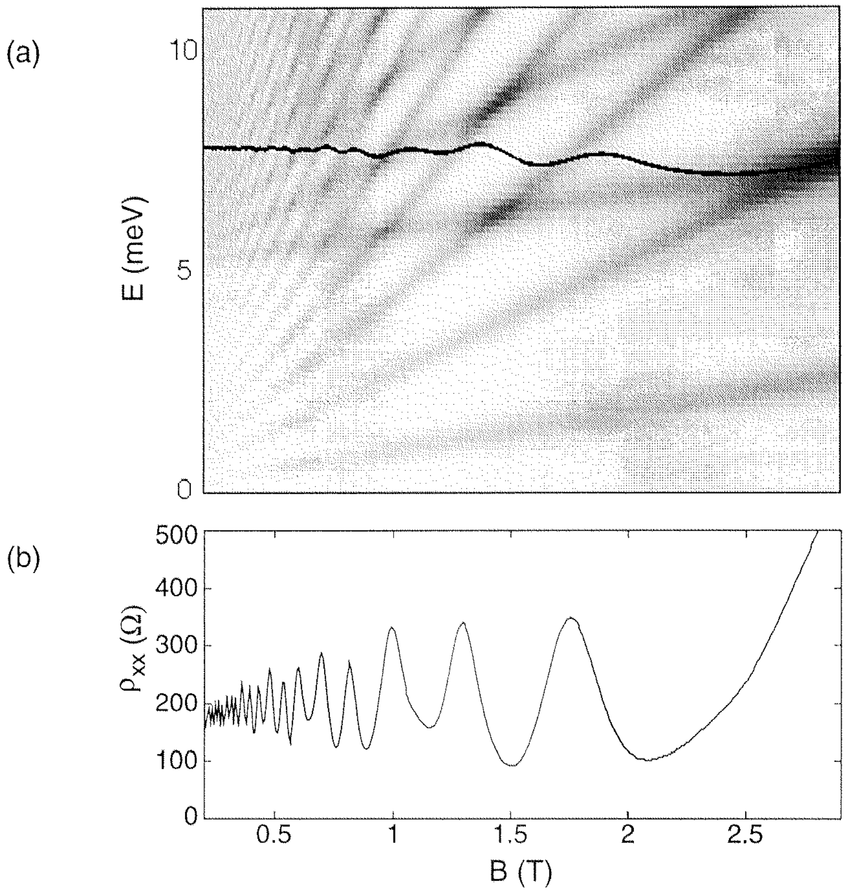

Figure 2.10: (a) Simulation of the Fermi energy and the DOS, indicated in grayscales (darker shadings correspond to higher DOS). The subband densities are $n_0 = 2.2 \cdot 10^{15}\,\mathrm{m}^{-2}$ and $n_1 = 0.8 \cdot 10^{15}\,\mathrm{m}^{-2}$. (b) Magnetoresistivity $\rho_{xx}(B)$ for the data calculated in (a).

is the cyclotron frequency, $\omega_c = eB/m^*$. The LL appear in the 2D DOS as discrete peaks, which are smeared out due to disorder (Fig. 2.11). The degeneracy of each LL is given by B divided by the flux quantum h/e. Since more states get available in each LL as the magnetic field is increased, higher LLs are successively depopulated. This gives rise to jumps in the Fermi energy, and several physical properties oscillate with the magnetic field – such as the magnetic susceptibility (de Haas-van Alphen effect) or the resistivity (Shubnikov-de Haas effect).

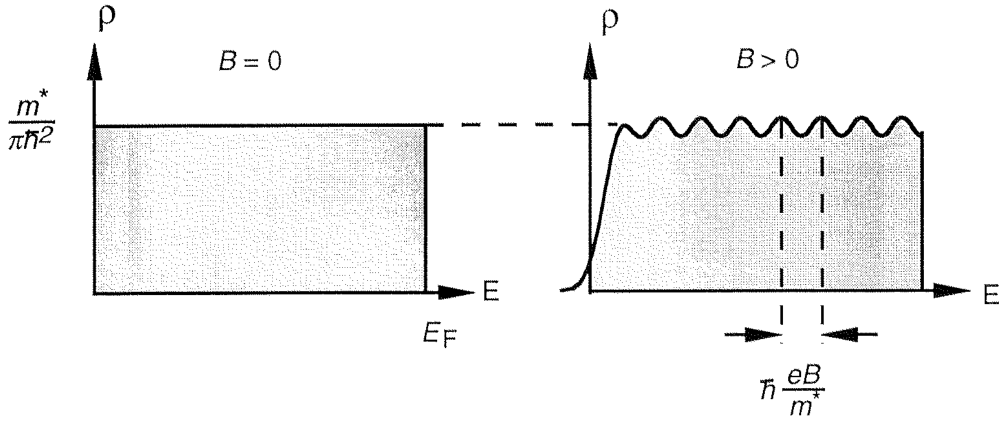

Figure 2.11: Density of states (DOS) for $B = 0$ and for $B > 0$, where the DOS gradually splits into Landau levels.

Each time when the electron density n_H in the system is an integer multiple ν of the LL degeneracy, a LL depletion occurs. In such a situation, the Fermi energy lies in between two LLs, where the DOS is reduced. Due to the Einstein relation $\sigma = e^2\rho(E_F)D$ [34] between conductance, DOS and diffusion constant the conductance is also reduced in between two LLs. This leads to a minimum in the conductance when

$$\nu = \frac{n_H h}{Be}. \tag{2.18}$$

The filling factor ν denotes the number of filled LLs. From this equation we see that the conductance oscillates as a function of $1/B$. Its frequency is proportional to n_H. At higher fields, where the LL spacing is larger than the width of the corresponding DOS-peaks, no states are available in between two LLs, and the conductance is expected to be zero. Because of a finite Hall voltage the resistivity is zero, too. In this simple picture, however, the Fermi energy cannot lie in between two LL's, as there are no states available. Therefore no finite regions with zero resistivity are expected, in contradiction to the experiments. As a consequence, the existence of localized states in the tails of the DOS peaks is assumed. These localized states are explained by disorder and do not contribute to the conductance, but allow the Fermi energy to lie between two LL's. This assumption also explains the finite width of the quantum Hall plateaus. The explanation for the universal values of the Hall resistance plateaus is more complicated.

For a multi-subband system with subband energies E_i, the energy spectrum is given by

$$E_{i\ell} = E_i + \hbar\omega_c(\ell + 1/2), \tag{2.19}$$

where the cyclotron frequency $\omega_c \propto B$ determines the LL splitting. If $E_{i\ell}$ is plotted as a function of B one obtains a LL fan for each subband energy (Fig. 2.10a). The width of a LL peak depends on the electron scattering rate $1/\tau_s$. On the other hand, the DOS determines the screening of the impurities and thus the electron scattering rate. Therefore the DOS distribution has to be determined self-consistently. In the self-consistent Born approximation the width of a LL is approximately proportional to $\sqrt{B}$, and the conductivity σ_{xx} is proportional to the squared DOS at the Fermi energy [35, 36]. Figure 2.10 shows the calculated DOS. Demanding charge conservation for $B = 0$

$$\int_{-\infty}^{E_F} \sum_i \rho_i(E) dE = n_H, \tag{2.20}$$

the Fermi Energy E_F is obtained by summing over the DOS ρ_i of all subbands i. In Fig. 2.10a the calculated E_F is shown for a two-subband system as a function of B. Assuming a Hall resistivity $\rho_{xy}(B)$ which increases linearly with B, the magnetoresistivity ρ_{xx} is obtained by tensor inversion of the σ_{xx} data. Figure 2.10b shows the calculated $\rho_{xx}(B)$ corresponding to the LL fans in Fig. 2.10a. Such calculations explain specific features in measured $\rho_{xx}(B)$ traces, such as the superposition of SdH oscillations of different frequencies or the suppression of quantum-Hall minima when the Fermi energy lies in degenerate LL of different subbands [37, 38, 39, 40].

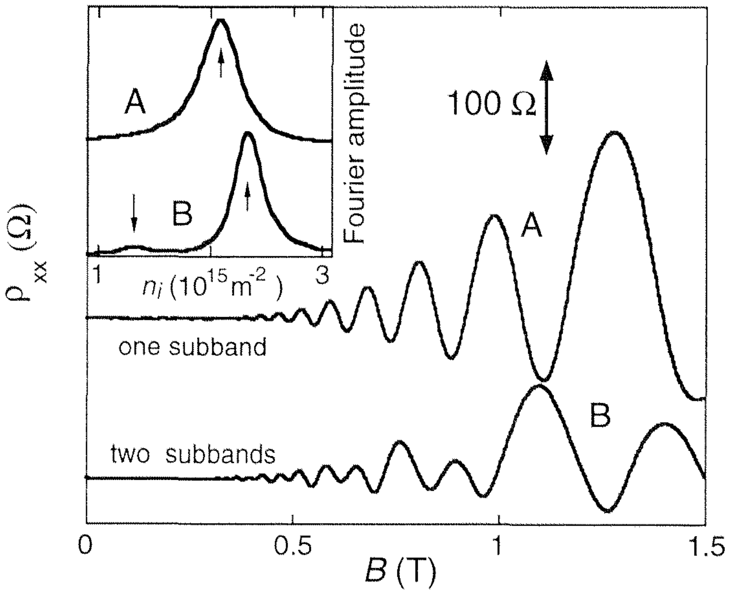

Figure 2.12: Measured SdH-oscillations of the magnetoresistivity ρ_{xx} vs. B at $T = 1.7\,\mathrm{K}$ and for different n_H of $2.1 \cdot 10^{15}\,\mathrm{m}^{-2}$ (A) and $3.6 \cdot 10^{15}\,\mathrm{m}^{-2}$ (B). In case (A), one subband is occupied, in case (B) two of them. The peaks of the Fourier transformation of $\rho_{xx}(1/B)$ shown in the inset give the subband densities n_i. In (B), two peaks are seen (arrows), corresponding to the two occupied subbands. Taken from Ref. [41].

In Fig. 2.10a E_F is almost constant at low B. This is expected for $\hbar\omega_c < \hbar/\tau_s$. In this regime, E_F crosses a LL each time when $E_{i\ell} = E_F$. This condition is fulfilled when

$$\ell + 1/2 = hn_i/2eB. \tag{2.21}$$

The oscillations in $\rho_{xx}(1/B)$ are composed of frequencies proportional to n_i. A Fourier analysis of $\rho_{xx}(1/B)$ reveals the different n_i. An example is shown in Fig. 2.12 with measurements at densities where one and two subbands are occupied.

From the determined n_i, the energy difference $E_F - E_i$ can be calculated. A comparison of self-consistently calculated energy levels with measured n_i at different gate voltages convincingly demonstrates that the analysis of SdH oscillations is an accurate tool to investigate the energy spectrum. Figure 2.13 shows such a comparison, taken from Ref. [41].

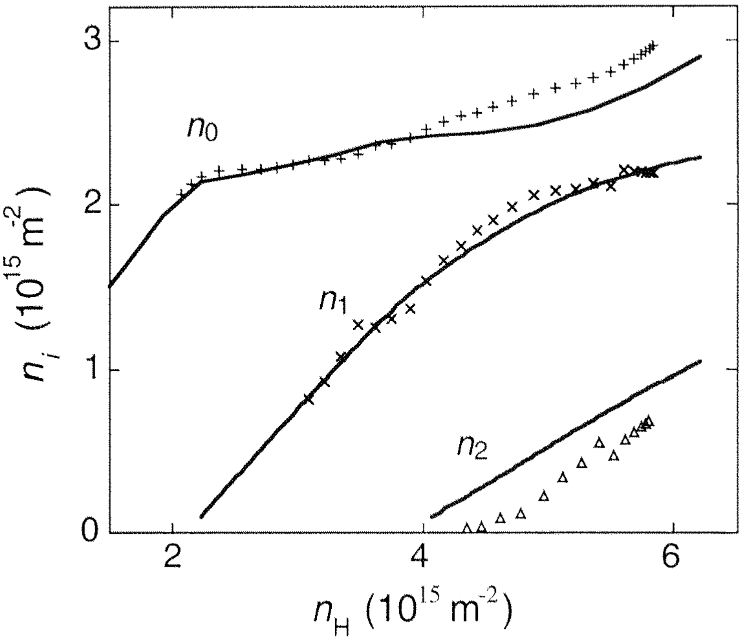

Figure 2.13: Measured subband densities n_i (symbols) for different n_H controlled by U_{fg} and fixed $U_{bg} = 0.0$ V. The sample has a potential spike with $x = 0.1$ inserted. The subband densities n_0 and n_1 are obtained from a Fourier-analysis of $\rho_{xx}(1/B)$, n_2 from $n_2 = n_H - n_0 - n_1$. The lines display self-consistently calculated subband densities for different n_H, also controlled with the front gate voltage, similar to the experiment. No fit parameters were used. Taken from Ref. [41].

Note that with transport measurements the difference of energy levels to the Fermi energy is determined, not individual subband energies. However, if two subband densities are known, their difference is proportional to the difference of the corresponding subband energies:

$$n_i - n_j = \frac{m^*}{\pi\hbar^2}(E_j - E_i). \tag{2.22}$$

Energy spectroscopy with transport experiments is based on this equation. In addition to subband energies, even electron probability distributions can be measured. This is demonstrated in chapter 3.4.

We now turn our attention to experimental data. Fig. 2.14 shows measurements of $\rho_{xx}(B)$ and $\rho_{xy}(B)$ for different front gate voltages U_{fg}. The back-gate electrode was grounded for this measurement. The temperature was 1.7 K. Various aspects of multi-subband transport can be discussed with the help of this plot.

First of all we observe that the slope of the Hall-resistance decreases with increasing U_{fg}. Because of $\rho_{xy} = eB/n_{\mathrm{H}}$, this directly reflects the increase of n_{H} with U_{fg}.

The quantum character manifests itself in the Hall plateaus at fields $B > 1\,\mathrm{T}$ which lie at positions $h/e^2\nu$, where ν is an integer filling factor. Weak spin-split plateaus (odd ν) are observed only at $\nu = 3$ and $\nu = 5$. Parallel to plateaus in ρ_{xy}, minima in ρ_{xx} appear, which are close to zero for higher fields ($B > 2\,\mathrm{T}$).

A striking feature appears at $U_{\mathrm{fg}} = -220\,\mathrm{mV}$. The low-field magnetoresistance increases with B. The reason is the population of a second subband. It is shown in chapter 4.1.4 that such a feature is expected for two-subband transport with different subband densities and different subband mobilities.

For $U_{\mathrm{fg}} > -220\,\mathrm{mV}$, the SdH oscillations are composed of two frequencies reflecting the two subband densities. At higher fields, we observe a missing QH plateau at $\nu = 4$ for $U_{\mathrm{fg}} = -220\,\mathrm{mV}$ and at $\nu = 6$ for $U_{\mathrm{fg}} = -160\,\mathrm{mV}$. Simultaneously to those situations, the minimum in ρ_{xx} is lifted. This suppression was explained as a consequence of degenerated LLs originating from different subbands [42, 43, 40]. We will come back to this explanation when we observe a similar effect in ballistic quasi-one dimensional channels where an energy degeneracy at the Fermi energy leads to suppression of conductance plateaus (chapter 7).

2.6 Tuning the Electron Gas

With voltages applied to the front- and back gate electrodes of the PQW, the electron sheet density n_{H} and the position Δz of the electron distribution along the z-axis can be tuned independently. In the first section, we examine how the density is tuned, while in the second section measurements and calculations of the displacement Δz are presented.

2.6.1 Density Tuning

A basic relation between gate voltage and electron sheet density can be derived in a simple model, which is described here. The PQW is embedded between a front- and a back gate electrode (Fig. 2.15). The electron gas forms a slab of finite thickness and electron sheet density n_{H}. A voltage U_{fg} applied between the front gate and the electron gas induces a surface charge σ_f on the front gate surface. In analogy, U_{bg} induces σ_{b} on the back gate electrode. The surface charges can be related to the gate voltages through the capacities C_{f} and C_{b}. With d_f being the separation between the front gate and the frontside boundary of the electron slab (Fig. 2.15), one obtains

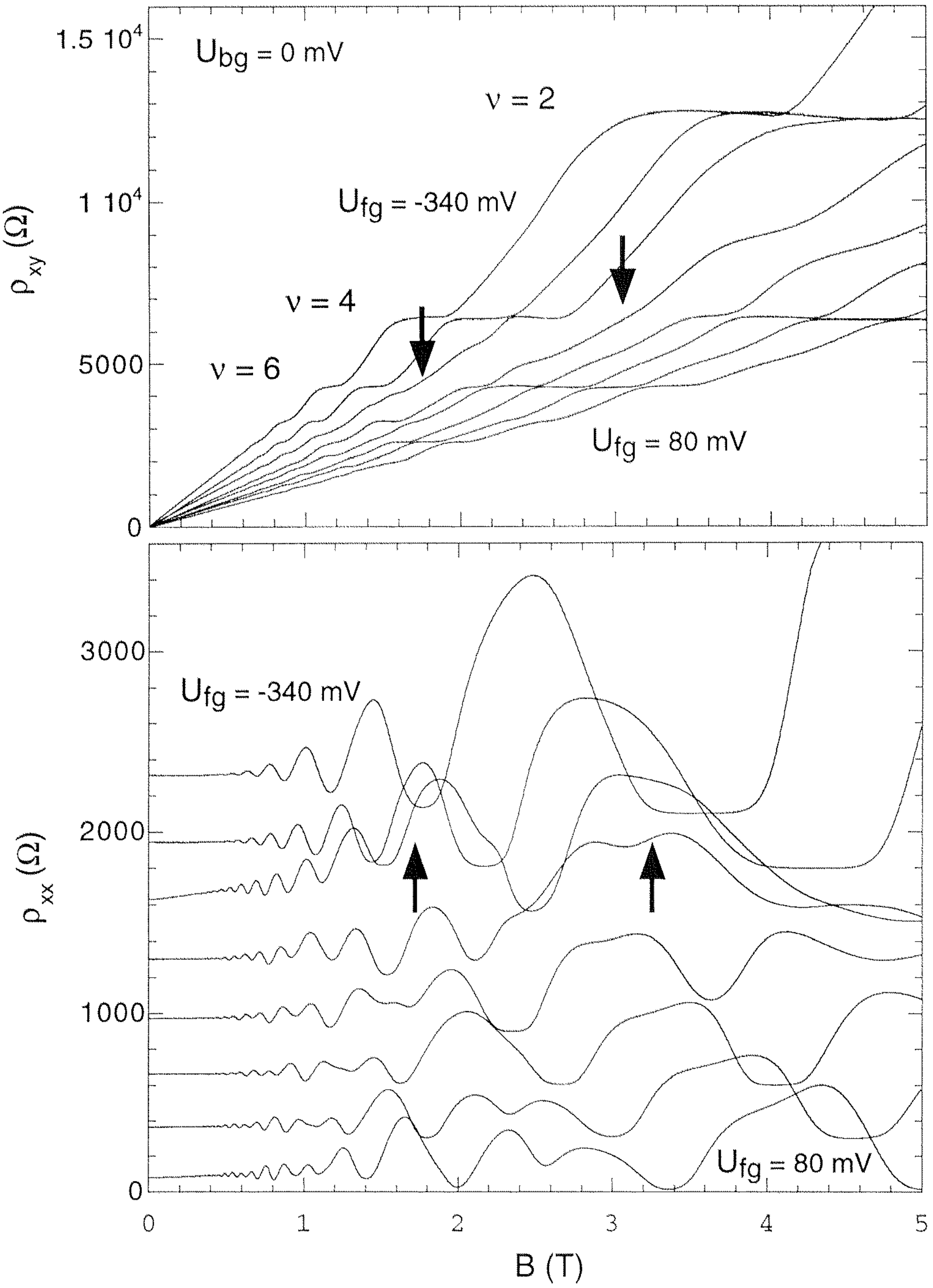

Figure 2.14: Hall- and magnetoresistivity measured at $T = 1.7\,\mathrm{K}$ on sample 6 (x=0.1). U_{fg} was varied between -340 mV and 80 mV in steps of 60 mV, and $U_{\mathrm{bg}} = 0\,\mathrm{mV}$. The arrows indicate suppressed Hall plateaus or suppressed minima in the magnetoresistivity.

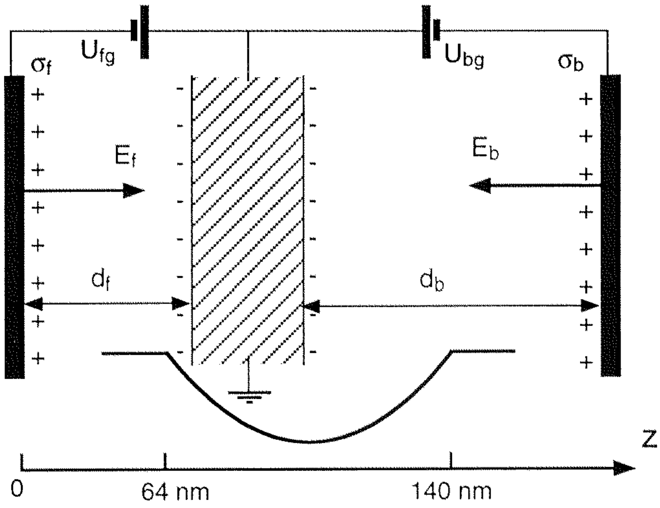

Figure 2.15: PQW between two capacitor plates, an adequate model to describe the tuning of electron sheet density in the well and the electron distribution displacement.

$\sigma_\mathrm{f} = \epsilon\epsilon_0 U_\mathrm{fg}/d_\mathrm{f}$. Charge conservation demands

$$e(n_\mathrm{H} - n_\mathrm{D}) = \sigma_f + \sigma_b = \epsilon\epsilon_0 \left(\frac{U_\mathrm{fg}}{d_\mathrm{f}} + \frac{U_\mathrm{bg}}{d_\mathrm{b}} \right). \tag{2.23}$$

Here, n_D is a contribution from the positively charged donor atoms between the capacitor plates. This expression for n_H describes the measured dependencies of n_H on U_fg and U_bg very accurately. Figure 2.16 shows measurements of $n_\mathrm{H}(U_\mathrm{fg})$. The fitted slopes of $5.4 \cdot 10^{15}\,\mathrm{m}^{-2}\mathrm{V}^{-1}$ (one occupied subband, low density) and $8.1 \cdot 10^{15}\,\mathrm{m}^{-2}\mathrm{V}^{-1}$ (high density) correspond to a d_f of 133 nm and 89 nm, respectively (assuming a permittivity of the AlGaAs layers between the gate and the electron gas of $\epsilon = 13$). This makes sense since both values lie inside the well (which extends from $z = 64\,\mathrm{nm}$ and $z = 140\,\mathrm{nm}$). For one occupied subband, the front side of the electron gas lies in the back side of the well. This is in agreement with self-consistent calculations, where it was found that the first subband starts to get populated in the back side of the well (section 2.4.2). The value of $d_\mathrm{f} = 133\,\mathrm{nm}$ is slightly too high, which can be explained by the disability of the electron gas to screen the front gate electric field effectively. Therefore the 2DEG model of a metallic slab is of limited validity in the case of one occupied subband, i.e., low electron densities. When the second subband gets populated, the slope increases considerably. This is due to the combination of a more efficient screening and the wider extent of the second wave function towards the front gate.

Measuring the zero-field resistivity, the mobility could be monitored as well, exploitingig the relation $\mu = 1/ne\rho_{xx}$ (Fig. 2.16). For low densities, μ increases with gate voltage and thus with n_H. At the cross-over from one to two occupied subbands at $U_\mathrm{fg} \approx 250\,\mathrm{mV}$, the mobility decreases and above -200 mV increases again. The dip in mobility is caused by an opening of an additional scattering channel, namely intersubband scattering. Due to a decreasing probability of large-angle scattering at higher densities, the mobility increases again, until at $U_\mathrm{fg} \approx 50\,\mathrm{mV}$ it decreases monotonically. There a third subband is occupied, and intersubband scattering again

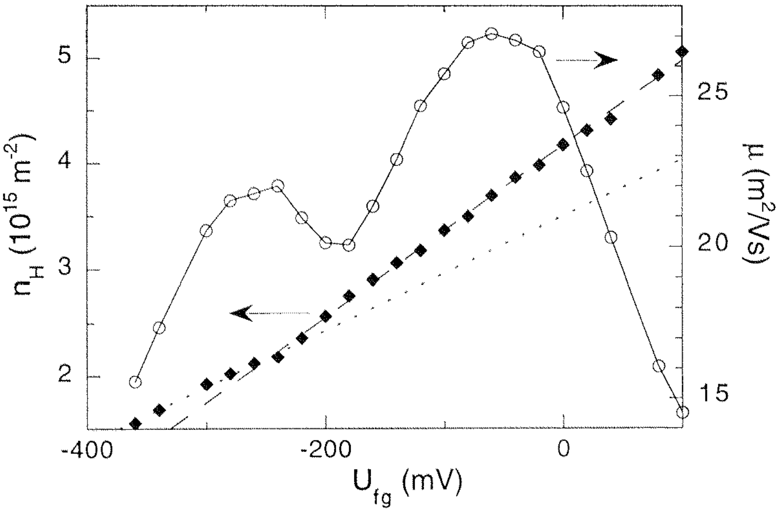

Figure 2.16: Hall density n_{H} and mobility μ of the electron gas in a PQW as a function of the front gate voltage U_{fg}. Also indicated are the fitted slopes for $n_{\mathrm{G}}(U_{\mathrm{fg}})$ of $8.1 \cdot 10^{15}\,\mathrm{m}^{-2}\mathrm{V}^{-1}$ (dashed) and $5.4 \cdot 10^{15}\,\mathrm{m}^{-2}\mathrm{V}^{-1}$ (dotted).

modifies the mobility behavior.

2.6.2 Displacing the Electron Gas

An important property of a PQW is that the superposition of the well potential with a linear potential results in a parabola of the same curvature, but with a spatially displaced energy minimum. By applying voltages to the gate electrodes, the electron gas is displaced along the z direction. In order to maintain a certain sheet density n_{H}, both front- and back gate are used to tune the displacement. In this section a quantitative model is described which gives a relation between the applied gate voltages and the displacement Δz of the electron gas.

We use the same capacitor-model as in the previous section. The surface charges σ_f and σ_b on the gates produce electric fields. The total field pointing towards the back gate is given by

$$E = \frac{\sigma_{\mathrm{f}} - \sigma_{\mathrm{b}}}{2\epsilon\epsilon_0}. \tag{2.24}$$

This field corresponds to a constant potential gradient, which adds to the parabola. If a linear potential $U_0(z) = eEz$ is superimposed on $U(z) = m^*\Omega^2 z^2/2$, the curvature of the parabola remains the same, whereas the potential minimum is displaced by

$$\Delta z = \frac{eE}{m^*\Omega^2}. \tag{2.25}$$

Expressed in terms of the surface charges on the gates, one obtains

$$\Delta z = \frac{e(\sigma_{\mathrm{f}} - \sigma_{\mathrm{b}})}{2\epsilon\epsilon_0 m^*\Omega^2}. \tag{2.26}$$

Using $\sigma_{\mathrm{f}} = \epsilon\epsilon_0 U_{\mathrm{f}}/d_{\mathrm{f}}$, one obtains for the displacement per front gate voltage

$$\frac{d}{dU_{\mathrm{fg}}}\Delta z = \frac{e}{2m^*\Omega^2 d_{\mathrm{f}}}. \tag{2.27}$$

Depending on the position of the front side of the electron slab (d_{f} between 64 nm and 100 nm), the shift lies between 110 nm/V and 69 nm/V. These values agree with those obtained from self-consistent calculations and the measured values, as presented in the next two sections.

Measurement of Δz

By applying appropriate gate voltages, n_{H} can be kept constant while the electrons are displaced along the growth direction. In the experiment, n_{H} is controlled by measuring the Hall resistance at $B = 0.2\,\mathrm{T}$, where quantum effects are not yet important. What is the relation between the applied gate voltage U_{fg} and the displacement Δz? In the plane spanned by U_{fg} and U_{bg}, the restriction that n_{H} is constant defines lines as shown in Fig. 2.17. From those lines the information on the displacement Δz per gate voltage can be extracted, if one assumes the capacitor relation between the geometric and the electrical variables described in Eq. 2.23.

Equation 2.23 describes the relation between U_{fg}, U_{bg}, d_{f} and d_{b}. At constant n_{H}, the width w of the electron slab is constant. Therefore $d_{\mathrm{f}} + d_{\mathrm{b}} = L$ is fixed, too. If this relation is inserted into Eq. 2.23, one gets

$$U_{\mathrm{bg}} = (L - d_{\mathrm{f}})\left(e\frac{n_{\mathrm{H}} - n_{\mathrm{D}}}{\epsilon\epsilon_0} - \frac{U_{\mathrm{fg}}}{d_{\mathrm{f}}}\right) \approx L\left(e\frac{n_{\mathrm{H}} - n_{\mathrm{D}}}{\epsilon\epsilon_0} - \frac{U_{\mathrm{fg}}}{d_{\mathrm{f}}}\right) \tag{2.28}$$

We write the distance d_{f} between front-gate and electron gas as the sum of the distance d_0 to an electron gas centered in the well and the displacement Δz, $d_{\mathrm{f}} = d_0 + \Delta z$ (Fig. 2.18). The displacement Δz is assumed to be linear in the applied voltage; $\Delta z = \alpha(U_{\mathrm{fg}} - U_{\mathrm{fg}}^0)$, where U_{fg}^0 is the front gate voltage at which the electron distribution is centered in the well. By fitting Eq. 2.28 to experimental data as shown in Fig. 2.17, the coefficient α is obtained. U_{fg}^0 is known from measurements of the subband densities, see chapter 3.3. For the distance d_0 we assumed $d_0 = 1020\,\text{Å} - w/2$, see Fig. 2.18. The 2DEG width w is given by $n_{\mathrm{H}}/n^{3\mathrm{D}}$ (see chapter 2.3). In Table 2.1 the results for different n_{H} are shown and compared to data obtained from self-consistent calculations of the wave functions [44].

The displacement per front-gate voltage increases with the electron density. This is explained by the larger extent of the electron distribution screening the parabolic potential closer to the front gate electrode. Thus the applied voltage drops in a smaller region and the electric field causing the displacement is increased.

Simulation of the Electron Displacement

In a self-consistent calculation, we kept the total carrier density constant and varied U_{fg} and U_{bg}. In Fig. 2.19, the calculated wave functions are shown for a PQW without a potential perturbation for two different gate voltages. In order to obtain $\Delta z(U_{\mathrm{fg}})$, we trace the position of the maximum $\Delta|\varphi|^2 = |\varphi_0|^2 - |\varphi_1|^2$ in the calculation as a function of the applied U_{fg}. We choose the quantity $\Delta|\varphi|^2$ because it can be measured

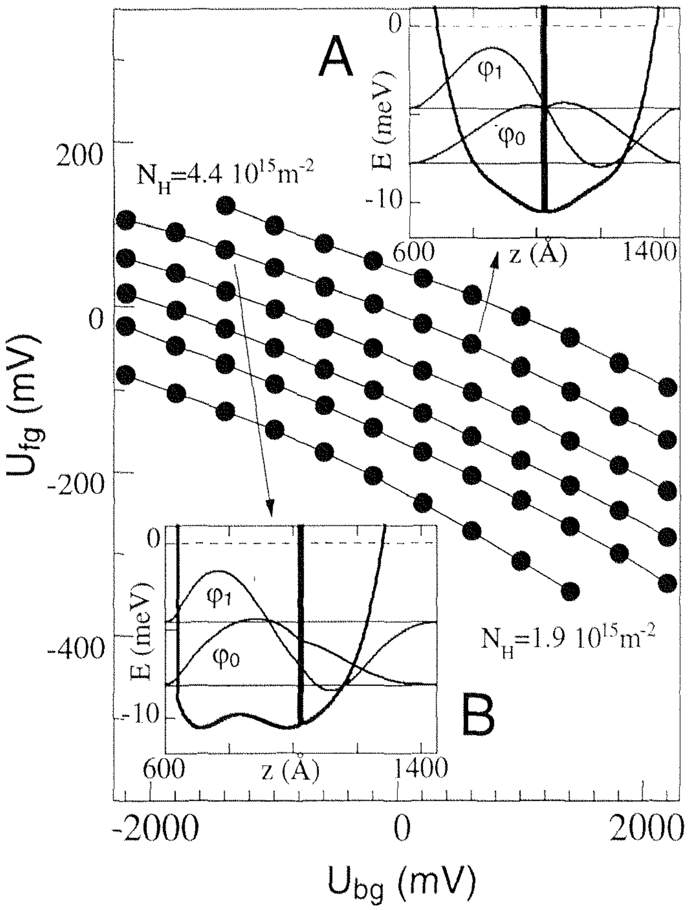

Figure 2.17: Measured contours of constant Hall density n_{H} for sample 2 (lines). The dots correspond to front- and back-gate voltages U_{fg} and U_{bg}, as applied in the experiment. U_{bg} ranges from $-2200\,\mathrm{mV}$ to $2200\,\mathrm{mV}$, the range of U_{fg} varies with U_{bg}. Hall densities are fixed at values between $1.9{\cdot}10^{15}$ m^{-2} and $4.4{\cdot}10^{15}$ m^{-2} in steps of $0.5 \cdot 10^{15}$ m^{-2}. The two inserts show calculated wave functions φ_0 and φ_1, the corresponding subband energies (straight lines), the Fermi Energy (dashed lines) and the screened potential including a potential spike at $n_{\mathrm{H}} = 3.9 \cdot 10^{15}\,\mathrm{m}^{-2}$ for a symmetric situation (A) and with the wave functions shifted towards the front gate (B).

(see chapter 3). An approximately linear relationship $\Delta z(U_{\mathrm{fg}})$ is found, which depends on the total electron density (insert of Fig. 2.19). The obtained values are summarized in Table 2.1.

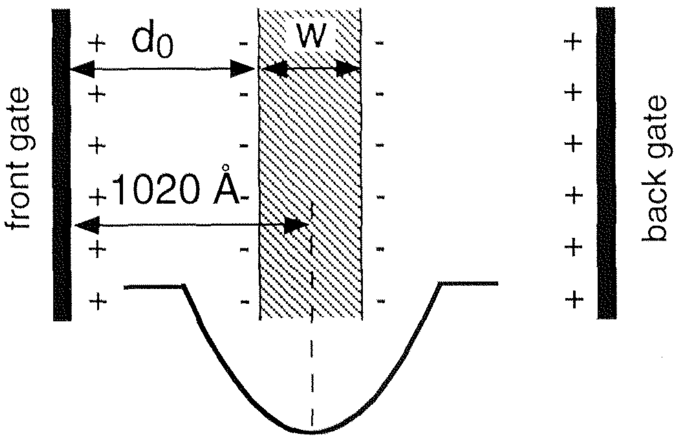

Figure 2.18: PQW between two capacitor plates with a centered 2DEG. The distance d_0 is measured between the front gate and the surface side of the 2DEG, shown here as a slab of width w.

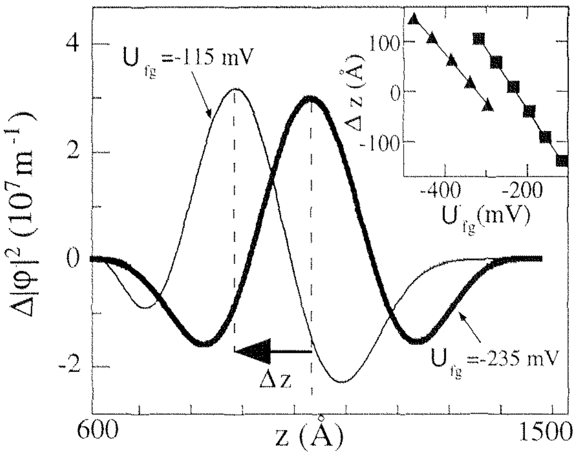

Figure 2.19: Self-consistently calculated $\Delta|\varphi|^2$ at $n_{\mathrm{H}}=3.9\cdot10^{15}\,\mathrm{m}^{-2}$ for two different U_{fg} and U_{bg}. The relative positions Δz of maxima in $\Delta|\varphi|^2$ are traced as a function of U_{fg} (insert) in order to monitor $\Delta|\varphi|^2$ as a function of the spatial coordinate. The insert shows the obtained Δz for $n_{\mathrm{H}}=2.4\cdot10^{15}\,\mathrm{m}^{-2}$ (triangles) and $n_{\mathrm{H}}=3.9\cdot10^{15}\,\mathrm{m}^{-2}$ (rectangles).

Table 2.1: Parameters for fitted $U_{\mathrm{bg}}(U_{\mathrm{fg}})$ of a sample with $x = 0.05$. Measured ($\alpha_{\mathrm{meas.}}$) and calculated ($\alpha_{\mathrm{calc.}}$) values for the electron-gas displacement per front-gate voltage are indicated for different constant Hall densities n_{H}. The fit parameters include the front-gate voltage U^0_{fg} where the electron distribution is centered in the well, the distance d_0 from the front gate to the upper surface of the electron gas, the well width w, the charge density correction n_{D} and the distance L between front and back gate.

n_{H} ($10^{15}\mathrm{m}^{-2}$)	U^0_{fg} mV	d_0 Å	w Å	n_{D} ($10^{15}\mathrm{m}^{-2}$)	L μm	$\alpha_{\mathrm{meas.}}$ (10^3 Å/V)	$\alpha_{\mathrm{calc.}}$ (10^3 Å/V)
2.5	-90	860	321	-1.16	1.48	-0.65±0.05	0.98
3.0	-70	828	385	-0.80	1.44	-0.79±0.05	1.0
3.5	-40	796	449	-0.35	1.39	-0.91±0.05	1.1
4.0							1.2

Chapter 3

Wave Function Spectroscopy

The wave-like nature of massive particles is among the most important findings in the physics of this century. In 1928 Davisson and Germer found that electrons travelling through a crystal lattice exhibit interference phenomena. This was the experimental demonstration of the quantum-mechanical wave-particle duality. Interference which was well-known from optics with visible light, also worked for massive particles! The wavelength attributed to a particle depends on its momentum exactly as de Broglie had postulated in 1923. Since then, the visualization of a particle's wave nature immanent to quantum mechanics has become a fascinating issue. With the discovery of scanning tunneling microscopes, it recently became possible to observe standing-wave patterns on a metallic surface on which atoms different from the substrate material were arranged with monoatomic precision. The interference of the electrons scattered by the foreign atoms generates fascinating patterns. The famous picture of the standing waves scattered at individual atoms arranged in a circle ('quantum corrals') found respect around the world [45, 46].

In some sense, these wave patterns in an electron sea are similar to surface waves broken at rocks in a shallow pool. In this analogy to classical physics, the standing waves arising in an organ pipe correspond to the quantized states in a potential well. Although this is the standard example in many books on quantum mechanics, these waves are difficult to detect experimentally. This has to do with the requirements imposed on the detector. The typical wavelength of electrons confined in a semiconductor quantum well is some tens of nanometers. In order to resolve the shape of the wave function, the resolution of the detector has to be smaller than this size.

But what can we actually measure? The wave functions themselves have no direct physical interpretation. Only the squared modulus of the wave function has the meaning of a probability density distribution. It is this quantity, which we want to detect.

The aim of this chapter is to present a new approach to investigate quantum-mechanical probability density distributions of electrons in a screened wide potential well. We tackle this problem by making use of the possibilities offered by MBE-growth. The probe is a thin sheet of three atomic layers of AlGaAs placed in the center of the quantum well. Making use of the result of first-order perturbation theory that the shift in energy of the electron states due to such a potential spike is proportional to the squared wave function, we simply have to measure the energy shift imposed by the probe to learn something about the wave functions and thus the electron probability at the spike position. Our method is based on low-temperature magnetotransport measurements. We extract the energy shifts from measured subband densities.

The concept is introduced in section 3.1. A brief overview of the experimental details (samples and measurement set-up) is given in section 3.2, followed by the presentation of the measured subband density differences for various samples and sheet densities. In the third section we determine the width w of the electron distribution as a function of the total electron sheet density n_{H}. The purpose of this is to demonstrate the intrinsic property of a PQW that n_{H} divided by w is a constant, corresponding to the 3D electron density. The aim of section 3.4 is to combine the perturbation idea with the idea of displacing the electron distribution (presented in chapter 2.6.2) in order to scan the spatial shape of the squared wave functions. The last section gives an outlook on future experiments. Part of the results presented in this chapter has been published in Ref. [47].

3.1 Concept of Wave Function Spectroscopy

Wave functions of intentionally modified surface states on metals have been probed using the scanning tunneling microscope [45]. In semiconductors, various attempts to measure the wave function of confined states have been undertaken. In particular, the wave function Fourier spectrum of bound states of Si doping layers located in the quantum well of a double-barrier resonant tunneling diode were measured by resonant magnetotunneling [48]. Extending this idea to an array of quantum wires, it was shown in Ref. [49] that the magnetotunneling differential conductance is a full representation of the 1D wave functions in k-space.

In a more direct approach wave functions are measured by analyzing the energy shift of quantized states due to an inserted, highly-localized potential perturbation. In this way, wave functions of electrons confined in semiconductor quantum wells [50] and in surface states of metals [51] have been investigated.

In order to probe probability densities with interband optical transitions in Ref. [50], the conduction band as well as the valence band states had to be considered, and the probability density distribution of electrons and holes were assumed to be equal. Additional complications result from light-hole- and heavy-hole-transitions.

The concept we use for probing the potential-well wave function was introduced in Ref. [50] and is based on first-order perturbation theory. A narrow potential barrier at the position z_0 within the PQW described by $U_0\delta(z-z_0)$ shifts the quantum-mechanical eigenstates $\varphi_i(z)$ with energies E_i in first-order perturbation theory according to (see Fig. 3.1)

$$E_i' = E_i + U_0|\varphi_i(z_0)|^2. \tag{3.1}$$

Measuring the shifted energies on many samples with different spike positions z_0 and comparing them to an unperturbed sample, the probability density distribution $|\varphi_i(z_0)|^2$ for different subbands i was mapped out in Ref.[50]. In our samples, the spike position is fixed. The electron distribution itself can be displaced along the growth

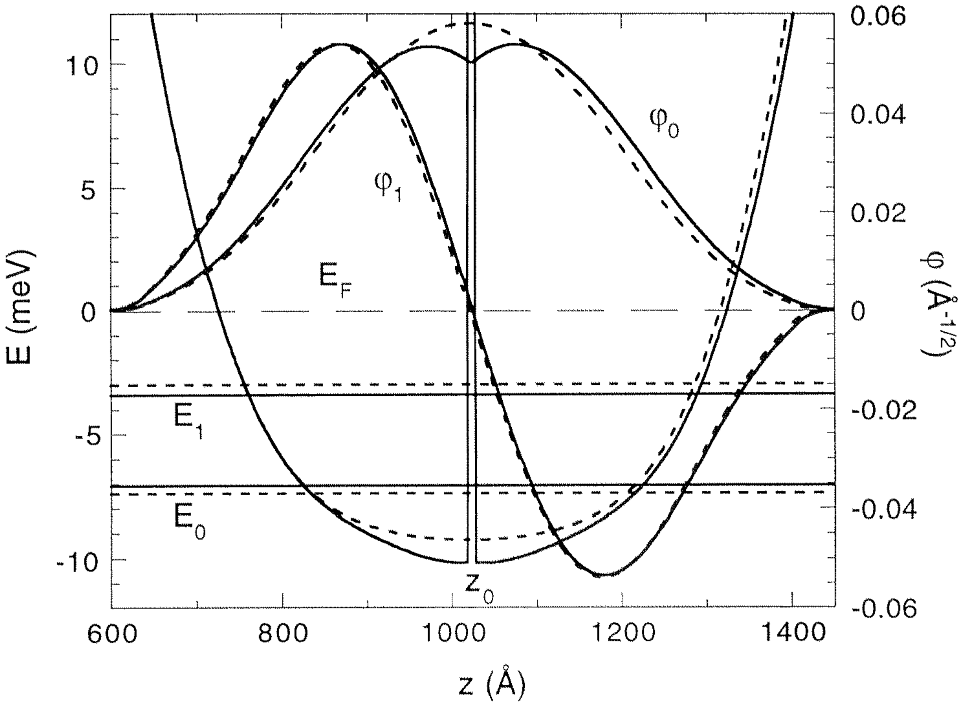

Figure 3.1: Self-consistent potential, subband energies and electron probability-density distributions for a sample without (dashed) and with a 9 Å thick $Al_{0.1}Ga_{0.9}As$-spike inserted in the center of the well at z_0 (lines). With spike, the well is 9 Å wider, which leads to the spatial displacement of the potential on the right side. The energies are indicated relatively to the Fermi energy.

direction with respect to the spike by applying electric fields across the parabola. Thus the unaltered shape of the spatially shifted wave functions can be probed at one spike position in the same sample.

We determine the single-particle energies of the screened PQW by measuring Shubnikov-de Haas oscillations of the longitudinal resistivity. The frequencies of the SdH oscillations yield the subband electron densities n_i (see chapter 2.5.2). Based on the energy independent density of states $\rho = m^*/\pi\hbar^2$ of a two-dimensional system (m^* = effective electron mass), we obtain the difference of the Fermi energy E_F to the respective subband energy level E_i'. In order to eliminate E_F, which itself depends on the subband energy levels, one subtracts two subband densities, n_i and n_j. Therefore, transport experiments measure differences of subband energies $E_i' - E_j' = \frac{\pi\hbar^2}{m}(n_j - n_i)$. According to Eq. (3.1), the influence of the potential spike is then written as

$$E_i' - E_j' = E_i - E_j + U_0(|\varphi_i(z_0)|^2 - |\varphi_j(z_0)|^2). \tag{3.2}$$

We obtain the difference of squared wave functions by comparing energy differences of two samples with different spike strengths U_a and U_b:

$$|\varphi_i(z_0)|^2 - |\varphi_j(z_0)|^2 = \frac{\pi\hbar^2}{m^*} \frac{(n_j - n_i)_{U_a} - (n_j - n_i)_{U_b}}{U_a - U_b} \tag{3.3}$$

The denominator $U_a - U_b$ is a well known growth parameter determined from the amount of Al in the potential spike. With this approach we have developed a method to measure differences in probability densities of occupied conduction band sublevels, based on low temperature magnetotransport experiments.

3.2 Experimental Details

A set of four different samples has been grown as discussed in chapter 2.2. The evaluated samples are numbered 15, 18, 21, and 22 (see Appendix C). In sample 15 the unperturbed parabolic potential is realized. In the other samples, a three monolayers thick $\mathrm{Al}_x\mathrm{Ga}_{1-x}\mathrm{As}$ potential spike was inserted in the center of the PQW, with $x = 0.05$, 0.1 and 0.15, respectively. The spike potential is described by $U\delta(z - z_0)$. With a spike width of 8.5 Å, an Al content x and a potential height of $x \cdot 790$ meV, we obtain $U = x \cdot 6720$ Å·meV. These potential perturbations are sufficiently weak to be treated in first-order perturbation theory.

Magnetotransport measurements have been carried out in a dilution refrigerator at temperatures below 100 mK. The electron density were varied between $1 \ldots 5 \cdot 10^{15}\,\mathrm{m}^{-2}$ by applying voltages U_{fg} and U_{bg} between the electron gas and the front- and back-gate electrodes, respectively. Typical electron mobilities are around $15\,\mathrm{m}^2/\mathrm{Vs}$, as obtained from the resistance at zero magnetic field. SdH-oscillations can typically be observed above 0.2 T.

Here we concentrate on the case of two occupied subbands. For the experimental realization of our idea, we have displaced the electron distribution inside the well by applying appropriate gate voltages, keeping the Hall density n_{H} constant, as obtained from the low field Hall effect.

3.3 Width of the Electron Distribution

If the wave functions are centered in the well, the lowest-subband wave function φ_0 has its maximum at the spike position, whereas the antisymmetric φ_1 vanishes at z_0. According to perturbation theory (Eq. 3.1), the energy shift of the E_1 subband is zero and that of the E_0 subband is given by $U_0|\varphi_0(z_0)|^2$. Away from this symmetric situation, $|\varphi_0(z_0)|^2$ decreases, whereas $|\varphi_1(z_0)|^2$ increases. This means that E_0 decreases and E_1 increases. Thus in the symmetric situation, the two lowest subbands are closest in energy and repel each other if the electron distribution is displaced. For centered wave functions, the electron probability $|\varphi_0(z_0)|^2$ at the spike position z_0 is obtained directly by a measurement of the spike-induced change of the subband energy difference. For the electrons displaced from the centered situation, $|\varphi_1(z_0)|^2$ is nonzero, and the difference of the two probability densities is obtained. This case is discussed in section 3.4. Here we concentrate on the centered situation.

Since the wave functions are normalized and localized over a width w, its amplitude must be proportional to $\sqrt{1/w}$. By measuring $|\varphi_0(z_0)|^2$, we can thus determine the width of the electron distribution. In the following, such measurements at different n_{H} are presented. Furthermore we investigate how $|\varphi_0(z_0)|^2$ decreases as the sheet density is increased. We can thus establish that the width w increases linearly with the 2D electron density n_H, i.e. that the 3D electron density $n^{3D} = n_\mathrm{H}/w$ is constant.

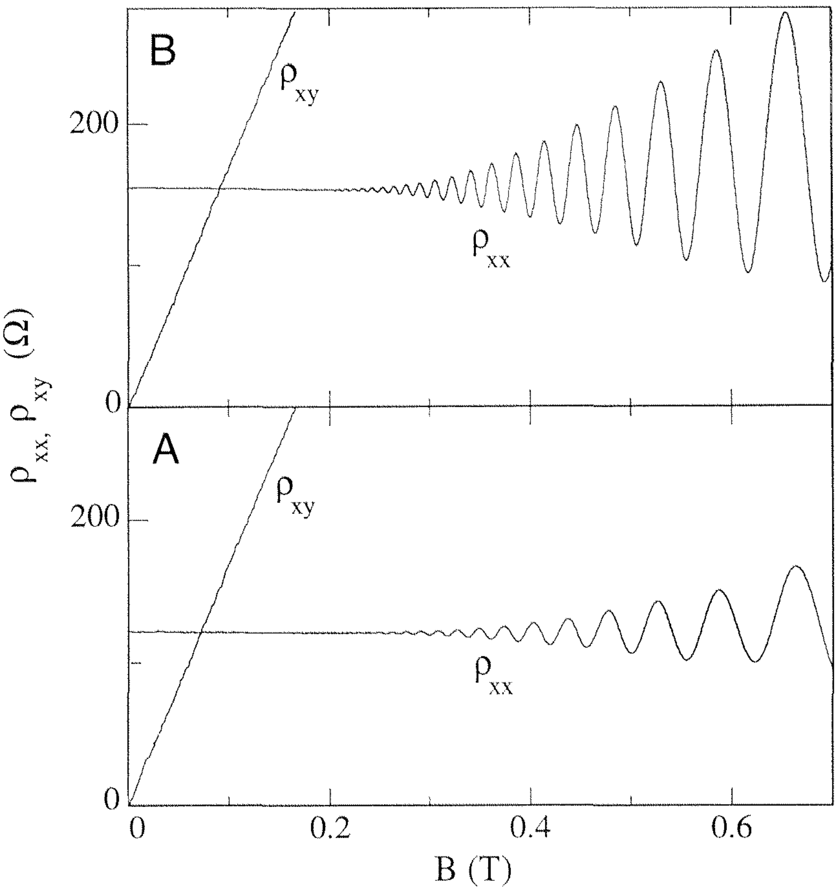

Figure 3.2: Measured magnetoresistivities ρ_{xx} and Hall resistivities ρ_{xy} are displayed for the two sets of gate voltages (A) and (B) as defined in Fig. 2.17. The Hall densities are equal, but the electron distributions are displaced along the growth direction.

In Fig. 2.17, contour lines of constant n_H in the U_fg-U_bg plane have been shown for sample 2. Two sets of gate voltages have been denoted by A and B corresponding to a balanced electron distribution (A) and a distribution displaced towards the front gate (B). In Fig. 3.2 we show corresponding measurements of $\rho_{xx}(B)$ and $\rho_{xy}(B)$. The Hall resistivities for the two sets increase linearly with B with the same slope, reflecting the equal Hall densities n_H. SdH oscillations can be observed in $\rho_{xx}(B)$. These were recorded for each pair of U_fg and U_bg along a line of constant n_H (symbols in Fig. 2.17). The subband density n_0 of the ground state can be evaluated most accurately from a Fourier transformation. The density n_1 is then determined using $n_1 = n_\mathrm{H} - n_0$. At constant n_H, the difference of the probability density $\Delta|\varphi|^2 = |\varphi_0(z_0)|^2 - |\varphi_1(z_0)|^2$ in Eq. (3.3) is proportional to the differences of $n_1 - n_0$ for two spike strengths.

Figure 3.3 shows measurements of $n_1 - n_0$ at different sheet densities n_H and for samples 1-4 with different spikes (described by its Al content $x = 0.0, 0.05, 0.1$ and 0.15, respectively). The individual curves display maxima at approximately the same U_fg for each x. At such a peak, a maximum amount of electrons stays in the upper subband, i.e., n_0 is lowest. From Eq. 2.22, it can be seen that this corresponds to a minimum in the energy difference $E_1 - E_0$, which is — as discussed above — the

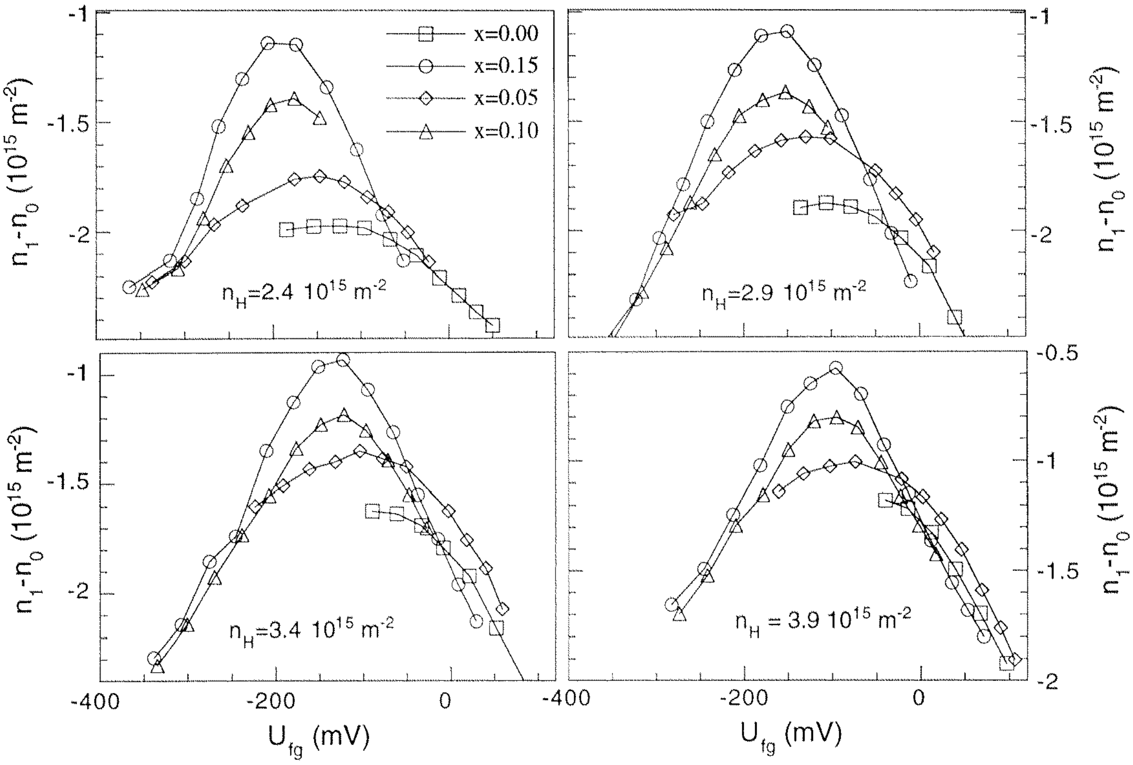

Figure 3.3: Measured $n_1 - n_0$ as a function of U_{fg} for $n_{\mathrm{H}} = 2.4 \cdot 10^{15}\,\mathrm{m}^{-2}$, $2.9 \cdot 10^{15}\,\mathrm{m}^{-2}$, $3.4 \cdot 10^{15}\,\mathrm{m}^{-2}$ and $3.9 \cdot 10^{15}\,\mathrm{m}^{-2}$. U_{bg} was adapted to fix n_{H}. Each measurement was performed on four samples with different potential spikes described by their Al content x.

indication of a balanced situation where the wave functions are centered in the well. The difference of two curves at this balanced situation gives the density difference due to the spike alone. From such differences, the energy shift can be determined. Following Eq. 3.3, we directly obtain $|\varphi_0(z_0)|^2$ by dividing the difference of two curves in Fig. 3.3 by the spike strength difference $\Delta U = \Delta x \cdot 6720\,\text{Å} \cdot \mathrm{meV}$ and the DOS. In Fig. 3.4 the obtained data is summarized. The error bars refer to deviations between different pairs of samples. A linear fit through the origin gives a slope of $130\ \text{Å}/10^{15}\,\mathrm{m}^{-2}$. In order to relate the width w of the electron gas to the amplitude of $|\varphi_0|^2$, assumptions about the shape of the wave functions have to be made. In the case of a deep square well of width a, the amplitude is given by $2/a$, such that $a = 2/|\varphi_0|^2$. The width w of the sinusoidal wave function can be defined as $w = a/2$, such that $w = 1/|\varphi_0|^2$. Thus the slope fitted in Fig. 3.4 corresponds to w/n_{H}. This value agrees with the designed $1/n^{3D} = 1.3 \cdot 10^{-23}\,\mathrm{m}^3$.

3.4 Scanning the Wave Function

Here we demonstrate that one-electron probability density distributions of PQWs in the presence of electron-electron interactions can be probed by magnetotransport measurements. In section 3.1 of this chapter we probed the difference of the electron probability density between two occupied subbands at the position of a highly localized and well-defined potential spike. In this section we show how we can scan

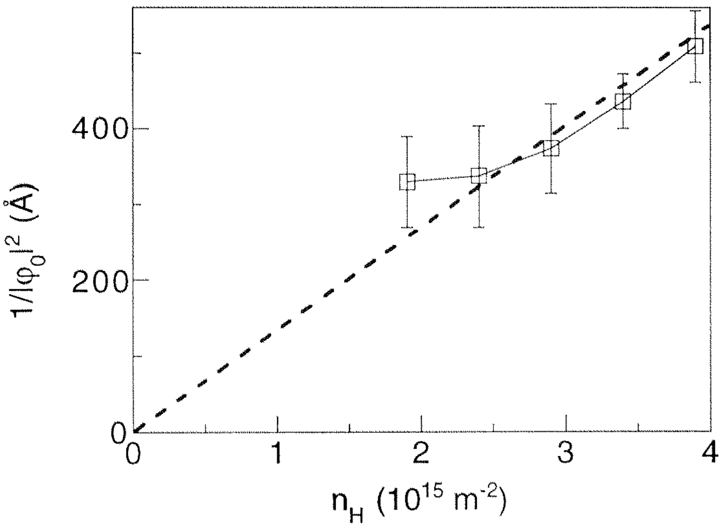

Figure 3.4: Measured $|\varphi_0(z_0)|^{-2}$ vs $n_{\rm H}$ (symbols). The dashed line is a linear fit to the data crossing the origin, corresponding to a linear increase of the 2DEG width with $n_{\rm H}$. The deviations for low $n_{\rm H}$ are because the effective potential has no flat bottom anymore.

the profile of the probability density distribution by displacing the wave functions through the spike. This is done by applying voltages to the front and back gates. Because the curvature of the parabolic potential remains unaffected by the superposition of a constant electric field, the electron wave functions are merely displaced. This statement remains valid in the presence of electron screening.

The measurements of $n_1 - n_0$ presented in Fig. 3.3 contain all the information we need to extract the probability density distribution. The distinct maxima in $n_1 - n_0$ get more pronounced for larger spike strength x. The difference in $n_1 - n_0$ for two samples with different spikes is smaller at higher densities. This is due to the fact that the width of the wave functions increases with density leading to a reduced amplitude of the wave functions at the spike positions.

According to Eq.(3.3), the data in Fig. 3.3 can be used directly to plot $\Delta|\varphi|^2$ as a function of the gate voltages. For this purpose, we interpolated the data in order to subtract unequally spaced data points from different samples. The central result is shown in Fig. 3.5, where all combinations of data from samples 2,3 and 4 are shown (symbols) for two different Hall densities.

Due to the measured relation between the wave-function displacement Δz and the gate voltage $U_{\rm fg}$ (Table 2.1), we can map the measured $\Delta|\varphi|^2$ as a function of spatial coordinate instead of gate voltage, and compare them to the calculated wave functions. The upper axis of Fig. 3.5 indicates the obtained Δz. The solid line corresponds to the calculated spatial probability density distributions. Note that there is no fit parameter. The data provides clear evidence that differences of single particle probability densities are measured. With increasing electron density, the screening of the parabolic potential becomes more pronounced and the wave functions spread out. Simultaneously, the amplitude of the wave functions is reduced due to their normalization. Both features are observed in the presented data (Fig. 3.5) and are

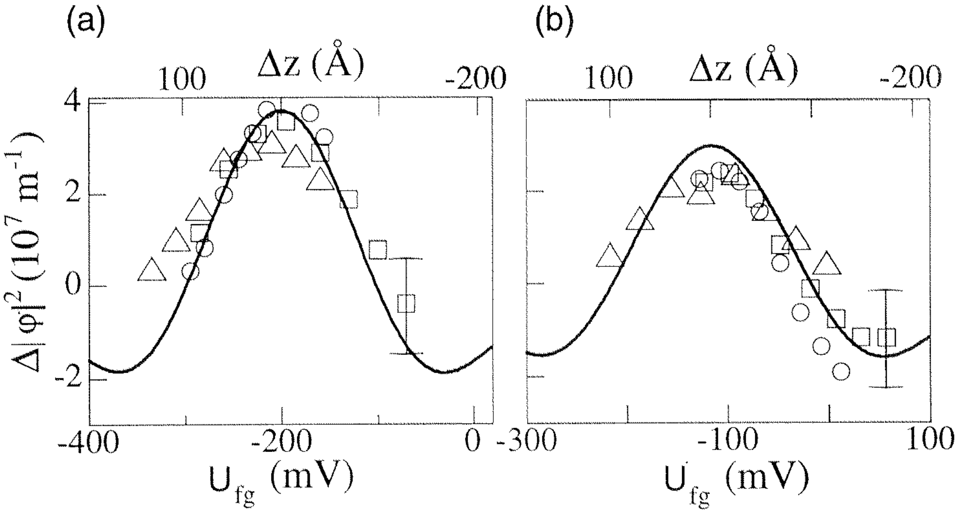

Figure 3.5: Measured (symbols) and calculated (solid lines) differences of probability density distributions $\Delta|\varphi|^2$ of the two lowest subbands for (a) n_H=2.4·10^{15} m^{-2} and (b) n_H=3.9·10^{15} m^{-2}. The data are obtained by subtracting interpolated values of $n_1 - n_0$ from Fig. 3.3. Triangles correspond to differences from samples with $x = 0.10$ and $x = 0.15$, circles from those with $x = 0.05$ and $x = 0.10$ and rectangles to $x = 0.05$ and $x = 0.15$. The error bars correspond to an estimated error of 2·10^7 m^{-1}. The front-gate voltages U_fg are linearly transformed to positions Δz (upper x-axis) as obtained from a capacitor model.

solely due to electron-screening of the parabolic potential.

3.5 Discussion and Conclusions

The method introduced is based upon the validity of first-order perturbation theory. Calculations show that in our samples with a three monolayers thick potential spike, the second-order contribution is at least five times smaller than the first order, even for the spike with $x = 0.15$. Also, the the spike-induced change in the self-consistent potential leads to small energy corrections. Experimentally, the accuracy is mainly limited by the measured Hall- and subband densities. Thereby the range of measured SdH oscillations in $1/B$ determines the resolution of the measured subband densities (for a discussion of the error induced by the Fourier transformation of SdH data, see Ref. [23]). One contribution to the error results from deviations in the electron sheet density from n_H due to multisubband effects. These are found to be small because the low-field Hall resistance is linear with magnetic field for all measured gate voltages. Deviations from sample to sample must be considered as well. From our data it can be deduced that they are mainly restricted to small displacements in gate voltages, which are not corrected in our analysis. Keeping in mind that the four samples were grown on different wafers, this confirms the perfect control of sample growth conditions. The upper limit for the error in n_H is estimated to be 1·10^{14} m^{-2}, giving an error in n_0 which is about half of this value. This corresponds to an error of $2{\cdot}10^7\,\mathrm{m}^{-1}$ in $\Delta|\varphi|^2$ (error bar in Fig. 3.5).

Due to the parabolicity of the as-grown potential, the shape of the electron distribution is maintained along a line of constant n_H in Fig. 2.17. This is true as long as the displaced electron distribution does not touch the hard walls surrounding the PQW. For the parabola investigated, the electron distribution can be approximated classically by a rectangular function of width $w \approx 510\,\mathrm{Å}$ at a density of $4{\cdot}10^{15}\mathrm{m}^{-2}$. At this density the electron distribution can thus still be moved ± 125 Å away from the center, without changing its shape. Quantum mechanically the wave functions belonging to different subbands have different widths and reach into the hard walls of the PQW. Thus a displacement of the wave functions from the center of the PQW will result in small modifications of individual wave functions. Due to its larger spatial extent, φ_1 is altered more than φ_0. This leads to modifications of $\Delta|\varphi|^2$ far away from the center of the electron distribution, whereas $\Delta|\varphi|^2$ remains mainly unaffected in the center (Fig. 2.19). Therefore the assumption of a pure displacement of wave functions is reasonable around the symmetric situation.

In conclusion, we have presented a method to locally probe differences of one-electron probability densities of electrons in a screened potential well. This has been done in a transport experiment at different electron sheet densities. Although in principle the method can be applied to any kind of potential well using a large number of samples, in the special case of a PQW, the spatial distribution of probability density differences can be mapped out with only two samples. We have demonstrated that in PQWs, the spatial distribution can be scanned by displacing the wave functions without changing their shape. Our experimental results are in excellent agreement with self-consistent subband calculations.

The wave function spectroscopy introduced in this chapter may also be reversed. Suppose the wave functions are known by self-consistent calculation. Then the unknown potential of an object can be measured. In this way for instance the potential of a layer of self-assembled quantum dots [52] could be determined. Due to strain of the InAs dots embedded in GaAs, the effective potential is modified. The experiment would allow to test theoretical models of this strain-induced potential change. This experiment is currently being performed in our group.

Chapter 4

Scattering Times in Parabolic Quantum Wells

In this chapter we discuss the relevant scattering mechanisms an electron experiences in PQWs at low temperatures, where both optical- and acoustic-phonon scattering are negligible. The dominant mechanism is scattering by the ionized dopants located in the layers on both sides of the PQW. This kind of scattering is an elastic process since the energy-transfer from the electron to the impurity is negligible due to the small electron mass. The momentum relaxation of the electrons determines the conductivity. Elastic scattering rates are obtained from the measured sample resistance. Theoretically, the conductivity is calculated from the relation between the current and the electric field, as it is obtained from the solution of the Boltzmann equation, where the transition rate of electrons scattered from an initial state i to a final state f needs to be known. In conventional 2DEGs at low temperatures, the initial and final states are both in the same subband. In a multi-subband systems as PQWs, also intersubband transitions have to be considered.

In the first section, we summarize how to calculate the scattering times, including a brief overview on screening in a multiple subband system, and a presentation of the different scattering mechanisms involved. In principle, the mobilities of individual subbands are obtained from the measured magnetic-field dependence of the resistivity. This is explained in the third section. Experiments measuring the Drude and the single-particle scattering times of the individual subbands are discussed in the fourth section. There we employ the wave function displacement introduced in chapter 2.6.2, in order to learn more about the spatial arrangement of the scatterers.

4.1 Calculation of Scattering Times

4.1.1 Fermi's Golden Rule

We describe how the single-particle scattering time is calculated in the one-subband case. The scattering rate $1/\tau_s$ of a particle subjected to the potential Φ is calculated using Fermi's Golden Rule:

$$\frac{1}{\tau_s} = \frac{2\pi}{\hbar} \sum_f |\langle f|\Phi|i\rangle|^2 \delta(E_f - E_i). \tag{4.1}$$

The wave functions of the initial state i and final state f are composed of the subband wave functions $\varphi(z)$ in z-direction and plane waves $A^{-1/2}e^{i\mathbf{k}_{\|}^{i,f}\mathbf{r}_{\|}}$ in x- and y-direction, where $\mathbf{k}_{\|}^{i,f}$ is the in-plane wave vector and $\mathbf{r}_{\|} = (x, y)$ the in-plane coordinate. The calculation of the matrix element involves an integration over $\mathbf{r}_{\|}$ corresponding to a Fourier transformation of Φ, which becomes a function of $\mathbf{q} = \mathbf{k}_{\|}^{f} - \mathbf{k}_{\|}^{i}$. There remains an integration over z:

$$\langle f|\Phi|i\rangle = \int \varphi^*(z)\varphi(z)dz \underbrace{\int e^{-i\mathbf{q}\mathbf{r}_{\|}}\Phi(\mathbf{r}_{\|}, z)d\mathbf{r}_{\|}}_{\Phi(\mathbf{q},z)} \frac{1}{A}, \tag{4.2}$$

This matrix element is the integral of the in-plane Fourier-transformed potential $\Phi(\mathbf{q}, z)$ times the subband wave functions. It can in most cases be divided into a form factor $F(\mathbf{q})$ and the z-independent contribution from the potential, $\Phi(\mathbf{q})$. Without any spatial correlation between the N individual scatterers, the averaged square of the matrix element is proportional to N:

$$\left\langle |\langle f|\Phi|i\rangle|^2 \right\rangle = \frac{N}{A} F(\mathbf{q})^2 |\Phi(\mathbf{q})|^2. \tag{4.3}$$

The final form for the scattering rate is obtained by replacing the sum over the final states f in Eq. 4.1 by an integral over the angle ϑ between $\mathbf{k}_{\|}^{i}$ and $\mathbf{k}_{\|}^{f}$, which is related to $q = |\mathbf{q}|$ by $q = \sqrt{2k_F^2(1 - \cos\vartheta)}$:

$$\frac{1}{\tau_s} = \frac{m}{2\pi\hbar^3} \int_0^{2\pi} d\vartheta \left\langle |\langle f|\Phi(q,\vartheta)|i\rangle|^2 \right\rangle. \tag{4.4}$$

The time τ_s describes the time an electron travels without being scattered. It is weighted uniformly over all ϑ. However, electrons which are scattered by a small angle contribute less to a resistance modification than large-angle scattering events. In order to obtain the Drude scattering time τ_D, the integrand of Eq. 4.4 has to be weighted by the factor $1 - \cos\vartheta$. This follows from the solution of the linearized Boltzmann equation, where the electron distribution in an electric field is considered.

4.1.2 Electron Screening

At low temperatures, the mobility of a 2DEG is limited by electron scattering due to the electric field of remote ionized impurities. The electrons do not feel the full Coulomb potential of the dopants. The spatially varying electric field is screened by the electron gas. In remotely doped 2DEGs, the separation of the dopants from the electron gas leads to a weak, slowly varying scattering potential[1]. In this section we describe how the screened electrostatic potential is calculated.

---

[1] Here, 'weak' means that the electrostatic potential induces a charge density which can be linearized with respect to the applied potential.

We regard a point charge separated by a distance d from the potential well. In general, the screening by an electron gas is described by introducing two electrostatic potentials [53]. The first, Φ^{ext} arises solely from the point charge, while the second, Φ is the full physical potential due to the impurity as well as the electron gas. Similarly, n_{ext} and n are the external and the full charge density, respectively. The charge density n_{ind} induced by the external charge is given by $n_{\text{ind}} = n - n_{\text{ext}}$. In analogy to the relation between the electric displacement $\mathbf{D}$ and the electric field $\mathbf{E}$, a dielectric constant $\epsilon(\mathbf{r}-\mathbf{r}')$ is defined, such that

$$\Phi^{\text{ext}}(\mathbf{r}) = \int d\mathbf{r}' \epsilon(\mathbf{r}-\mathbf{r}')\Phi(\mathbf{r}). \tag{4.5}$$

The relation between Φ and the induced charge density is given by the polarization P:

$$n_{\text{ind}}(\mathbf{r}) = \int d\mathbf{r}' P(\mathbf{r}-\mathbf{r}')\Phi(\mathbf{r}'). \tag{4.6}$$

Using $n_{\text{ind}} = n - n_{\text{ext}}$ and writing the potential Φ^{ext} as a function of the external charge n_{ext} by using the Greens function $v(\mathbf{r}-\mathbf{r}')$ of the Poisson equation, one obtains

$$\epsilon(\mathbf{r}-\mathbf{r}') = \delta(\mathbf{r}-\mathbf{r}') - \int d^3\mathbf{r}'' v(\mathbf{r}-\mathbf{r}'')P(\mathbf{r}'-\mathbf{r}''). \tag{4.7}$$

For two-dimensional systems it is convenient to Fourier-transform the above equations in the coordinates of the two-dimensional plane, as is suggested by the form of Eq. 4.2. Then Φ_{ext} becomes

$$\Phi^{\text{ext}}(\mathbf{q}, z) = \int dz' \epsilon(\mathbf{q}, z - z')\Phi(\mathbf{q}, z'). \tag{4.8}$$

The polarization can be calculated in first-order perturbation theory from the wave functions $\varphi_i(z)$ [54, 55] and is given in the Random Phase Approximation (RPA) by

$$P(\mathbf{q}, z, z') = -\sum_{ij} \Pi_{ij}^{\text{RPA}}(\mathbf{q})\varphi_i(z)\varphi_j^*(z)\varphi_i^*(z')\varphi_j(z'), \tag{4.9}$$

with the static electron density-density correlation function

$$\Pi_{ij}^{\text{RPA}}(\mathbf{q}) = \frac{2}{A}\sum_{\mathbf{k}_\parallel} \frac{f(E_{i\mathbf{k}_\parallel}) - f(E_{j\mathbf{k}_\parallel+\mathbf{q}})}{E_{i\mathbf{k}_\parallel} - E_{j\mathbf{k}_\parallel+\mathbf{q}}}. \tag{4.10}$$

The diagonal terms Π_{ii}^{RPA} were calculated by Stern [56]. The off-diagonal elements were described in Refs. [57, 58]. It is important to note that Π_{ij}^{RPA} is not zero for unoccupied subbands j, if subband i is occupied. Therefore also unoccupied subbands may contribute to the screening of the scattering potential, although they are not involved in the solution of the Boltzmann transport equation (at zero temperature). But how can a non-occupied subband contribute to screening? In the matrix formalism introduced here, we consider the response of an electron system to a perturbing potential, which usually originates from positively charged donors outside the 2DEG

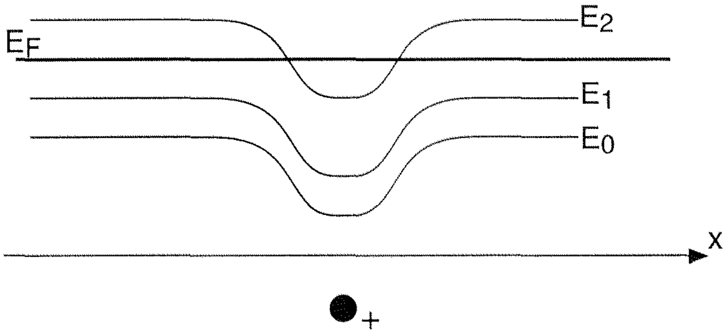

Figure 4.1: Higher subbands may also contribute to screening, as it is illustrated here in a two-subband system, where locally three subbands are occupied due to positively charged scatterers.

layer. The subband energies are bent downwards at the position of the charge, as illustrated in Fig. 4.1. Generally unoccupied subbands may be pulled below the Fermi energy locally.
Introducing the matrix elements $\Phi_{ij}(\mathbf{q}) = \int dz'\varphi_i^*(z)\varphi_j(z)\Phi(\mathbf{q},z)$, one obtains the matrix equation [54, 59]

$$\Phi_{ij}^{\mathrm{ext}}(\mathbf{q}) = \sum_{lm} \epsilon_{ij,lm}(\mathbf{q})\Phi_{lm}(\mathbf{q}), \tag{4.11}$$

with the dielectric function given by

$$\epsilon_{ij,lm}(\mathbf{q}) = \delta_{il,jm} + \int\int dz dz' \Pi_{ij}^{\mathrm{RPA}}(E_{\mathrm{F}})\varphi_l(z')\varphi_m^*(z')\varphi_i^*(z)\varphi_j(z)v(\mathbf{q}, z - z'). \tag{4.12}$$

The Fourier-transformed Greens function is given by

$$v(\mathbf{q}, z - z') = \frac{e^2}{2\epsilon\epsilon_0 q} e^{-q|z-z'|}. \tag{4.13}$$

Inserting this equation into Eq. 4.12, one obtains the final form for the dielectric matrix

$$\epsilon_{ij,lm}(\mathbf{q}) = \delta_{il,jm} + \frac{e^2}{2\epsilon\epsilon_0 q} F_{ij,lm}(q)\Pi_{ij}^{\mathrm{RPA}}(E_{\mathrm{F}}), \tag{4.14}$$

with the Coulomb form factor $F_{ij,lm}(q)$ given by

$$F_{ij,lm}(q) = \int\int dz dz' \varphi_l(z')\varphi_m^*(z')\varphi_i^*(z)\varphi_j(z)e^{-q|z-z'|}. \tag{4.15}$$

In order to obtain the screened potential Φ from the external potential Φ^{ext}, Eq. 4.11 has to be inverted. This means that the inverse dielectric matrix $\epsilon^{-1}_{ij,lm}$ has to be found. Then, the matrix element Φ_{ij} of the screened potential can be calculated with

$$\Phi_{ij}(\mathbf{q}) = \sum_{lm} \epsilon^{-1}_{ij,lm}(\mathbf{q}) \Phi^{\text{ext}}_{lm}(\mathbf{q}). \tag{4.16}$$

This formalism is a good approximation of screening in a multi-subband system, if the wave functions φ_i are known. The equations above assume the same dielectric constants in AlGaAs and GaAs. General expressions for the form factor for special geometries with varying dielectric constants were derived in Ref. [60]. Experiments on silicon inversion layers [61] and GaAs-AlGaAs heterojunctions [58] with two occupied subbands showed good agreement with this theory. The matrix-RPA formalism was also applied to multi-subband δ-doped systems with up to 6 occupied subbands [62]. A simpler approximation is the Thomas-Fermi approximation in two dimensions, where the induced charge is proportional to the DOS and to Φ:

$$n_{\text{ind}}(\mathbf{q}, z) = -e^2 \frac{m}{\pi \hbar^2} \Phi(\mathbf{q}, z) \delta(z). \tag{4.17}$$

With this surmise, the screened potential Φ becomes

$$\Phi(\mathbf{q}, z) = \frac{1}{1 + \frac{2}{a_B q}} \Phi^{\text{ext}}(\mathbf{q}, z), \tag{4.18}$$

where a_B is the effective Bohr radius ($a_B = 100$ Å for GaAs).

4.1.3 Scattering Mechanisms

This section gives an overview of the scattering potentials for the different scattering mechanisms. Besides Coulomb scattering, we also mention scattering by individual Al- and Ga- atoms in the AlGaAs alloy as well as scattering at the rough interfaces between the well and the surrounding AlGaAs. However, these two mechanisms are found to play a minor role in the determination of the overall scattering rate in PQWs.

Coulomb Scattering

Here we consider electron scattering by ionized impurities. The unscreened scattering potential of a single ionized impurity located at $\mathbf{r} = (0, 0, z_0)$ is given by

$$\Phi^C(\mathbf{r}) = -\frac{e^2}{4\pi\epsilon\epsilon_0} \frac{1}{|\mathbf{r} - \mathbf{r}_i|}. \tag{4.19}$$

The two-dimensional Fourier transform of the scattering potential is given by

$$\begin{aligned} \Phi^C(\mathbf{q}, z) &= \int dz' \frac{e^2}{2\epsilon\epsilon_0 q} e^{-q|z-z'|} \delta(z' - z_0) && (4.20) \\ &= \frac{e^2}{2\epsilon\epsilon_0 q} e^{-q|z-z_0|}. && (4.21) \end{aligned}$$

Thus the transition matrix element reads

$$\left\langle |\Phi_{ij}^{\mathrm{C}}(q)|^2 \right\rangle = \left(\frac{e^2}{2\epsilon\epsilon_0 q} F_{ij}(q, z_0) \right)^2 \frac{N}{A}, \tag{4.22}$$

where $F_{ij}(q, z_0) = \int_{-\infty}^{\infty} dz \varphi_j^*(z) \varphi_i(z) e^{-q|z-z_0|}$ is the Coulomb form factor.
In the PQW samples, ionized impurities are located on both sides of the well, and two contributions have to be considered.

Alloy Scattering

Alloy scattering refers to the scattering present in alloys due to the random distribution of component atoms among the available lattice sites [63]. In a square well where the electrons reside in the ternary compound $\mathrm{Al}_x\mathrm{Ga}_{1-x}\mathrm{As}$, the averaged squared scattering potential is given by [63, 64, 65]

$$\left\langle |\Phi_{ij}^{\mathrm{A}}(q)|^2 \right\rangle = x(1-x) \frac{a_l^3}{4} (\delta V)^2 \frac{3}{2} \frac{1}{w}, \tag{4.23}$$

where a_l^3 is the alloy unit cell ($a_l = 4.65\,\text{Å}$), δV the conduction band offset between AlAs and GaAs (750 meV), and w the width of the potential well.
For a PQW, where x varies continuously along the well, the term $x(1-x)$ is replaced by the Form factor $\int dz \varphi_i^*(z) \varphi_j(z) x(z)(1-x(z))$. Using Eqs. 4.4 and 4.23, we estimate the single-particle alloy scattering rate to be $1.8 \cdot 10^{10}\mathrm{s}^{-1}$, assuming $x = 0.05$ and $w = 76\,\mathrm{nm}$.

Interface Roughness Scattering

Boundaries between semiconductor layers are never perfectly flat. Interface roughness contributes to the scattering rate. In the case of a quantum well, a simple picture considers the variation of the quantum well energies as a function of the variation of the well width. The scattering rate is proportional to this energy variation. For a square-well potential of width w the averaged squared matrix element of the random interface roughness potential is [66, 67, 68]

$$\left\langle |\Phi_{ij}^{\mathrm{IR}}(q)|^2 \right\rangle = \frac{2\pi^5 \Delta^2 \Lambda^2 \hbar^4}{m^{*2} w^6} e^{-q^2 \Lambda^2/4}. \tag{4.24}$$

The parameter Δ denotes the amplitude of the well width fluctuations and Λ is the correlation length of the fluctuations. We see that the interface roughness potential decreases with the well width as $1/w^6$. Assuming $\Delta = 5\,\text{Å}$ (two monolayers) and $\Lambda = 300\,\text{Å}$ [69] gives for a $w = 76\,\mathrm{nm}$ wide PQW a scattering rate of $1.7 \cdot 10^8\mathrm{s}^{-1}$, which is small compared to the alloy scattering rate. The values for both, alloy and interface-roughness scattering, are small compared to the Coulomb contribution, as found experimentally (chapter 4.2.3) and by calculations (chapter 4.2.5).

4.1.4 Scattering Times in a Two-Subband Quantum Well

The question arises how the mobility in different subbands of a PQW is characterized. By using Ohm's law $j = \sum_i \sigma_i E$ one can attribute individual conductivities σ_i to each subband i. The Drude scattering times τ_i and subband mobilities $\mu_i = e\tau_i/m^*$ are obtained from the conductivities using the Drude result $\sigma_i = n_i e^2 \tau_i(B)/m^*$ with a magnetic-field dependent scattering time $\tau_i(B)$ (e,m^* electron charge and effective mass).

In a magnetic field, the conductivity σ_i and thus $\tau_i(B)$ decrease like a Lorentzian ($\tau_i = \tau_i(B=0)$):

$$\tau_i(B) = \frac{\tau_i}{1 + \omega_c^2 \tau_i^2}, \tag{4.25}$$

which is easily verified by inverting the resistivity tensor given by

$$\begin{aligned} \rho_{xx,i} &= \frac{m}{n_i e^2 \tau_i} && (4.26) \\ \rho_{xy,i} &= \frac{B}{n_i e}. && (4.27) \end{aligned}$$

The total conductivity is simply $\sum_i \sigma_i$. The resistance $\rho_{xx}(B)$ is obtained by inversion of the conductivity matrix. For small B, the resistance increases quadratically with the magnetic field, i.e. $\rho_{xx}(B) = \rho_{xx}(0)(1 + aB^2)$ [70] with

$$a = \frac{n_0 \tau_0 n_1 \tau_1 (\tau_0 - \tau_1)^2 e^2}{m^2 (n_0 \tau_0 + n_1 \tau_1)^2}. \tag{4.28}$$

From this so-called positive magnetoresistance the scattering times τ_i of a two-subband system can be extracted [71, 70, 72].

The possibility of intersubband scattering increases the phase space for final states. This enhances the scattering probability and thus decreases the mobility, which was first observed in Refs. [73, 74]. The solution of the Boltzmann equation taking intersubband scattering into account has been given by Siggia [54]. In most cases the subband scattering times do not depend on B in the usual way, i.e. $\tau_i(B)$ is not given by Eq. 4.25 anymore. This important fact was first mentioned by Zaremba [75]. Accordingly, the positive magnetoresistance is not given by Eq. 4.28 anymore. In his model based upon the Boltzmann equation, Zaremba takes intersubband scattering into account explicitly. This leads to a modified B-dependence of $\tau_i(B)$, which can be written as [75]

$$\tau_i(B) = \mathrm{Re}\left(\sum_j (\mathbf{K} + i\omega_c \mathbf{1})^{-1}_{ij} k_j / k_i \right), \tag{4.29}$$

where the k_i are the Fermi wave vectors, $k_i = \sqrt{2\pi n_i}$, $\omega_c = eB/m$, and $\mathbf{K}$ the scattering matrix defined by

$$\begin{aligned}\mathbf{K} &= \begin{pmatrix} K_1 & K_3 \\ K_3 & K_2 \end{pmatrix} \\ &= \begin{pmatrix} P_{00}^{(0)} - P_{00}^{(1)} + P_{10}^{(0)} & -P_{10}^{(1)} \\ -P_{10}^{(1)} & P_{11}^{(0)} - P_{11}^{(1)} + P_{10}^{(0)} \end{pmatrix}.\end{aligned} \tag{4.30}$$

The coefficients $P_{nm}^{(i)}$ are related to the transition rates $P_{nm}(\vartheta) \propto |\langle n|\Phi(\vartheta)|m\rangle|^2$ between subband states n and m and scattering angle ϑ by Fourier transformation in ϑ. $P_{ij}^{(0)}$ is the transition rate integrated over the allowed scattering vectors, while in $P_{ij}^{(1)}$ the integrand is multiplied by $\cos\vartheta$. Both transition rates are generalized expressions of the one-subband case in Eq. 4.4. The difference $P_{ii}^{(0)} - P_{ii}^{(1)}$ corresponds to the single-subband Drude scattering rate, where the matrix element of the scattering potential is weighted by $(1 - \cos\vartheta)$. Transforming Eq. 4.29, one obtains

$$\tau_i(B) = \frac{K_1(K_2^2 + \omega_c^2) + K_3(K_3^2 - \frac{k_1}{k_2}K_2K_3 - K_1K_2 + \omega_c^2)(k_2/k_1)}{(K_1^2 + \omega_c^2)(K_2^2 + \omega_c^2) + K_3^2(K_3^2 + 2\omega_c^2 - 2K_1K_2)} \tag{4.31}$$

In the special case $K_3 = 0$, Eq. 4.31 reduces to the independent-subband case of Eq. 4.25. Note that in the diagonal elements $K_{1,2}$, also the isotropic part of intersubband scattering is included. It was shown that intersubband scattering cannot be neglected for our PQW samples and K_{12} cannot be assumed to be small [76, 77]. With n_i known, Eq. 4.29 allows a fit to $\rho_{xx}(B)$, with K_1, K_2 and K_3 being the fit parameters [75] (Fig. 4.2a).

4.2 How Does Elastic Scattering Vary Across a PQW?

In this section, we study the elastic scattering times of electrons in two subbands of a PQW. This is done at constant electron sheet density, but different positions of the electron distribution along the growth direction. We find that the scattering times obtained by magnetotransport measurements decrease as the electrons are displaced towards the well edges, although the lowest-subband density increases. By comparing the measurements with calculations of the scattering times of a two-subband system, new information on the location of the relevant scatterers and the anisotropy of intersubband scattering is obtained. It is found that the scattering time of electrons in the lower subband depends sensitively on the position of the scatterers, which also explains the measured dependence of the scattering on the carrier density. The measurements indicate a segregation of scatterers from the substrate side towards the quantum well during growth [78].

4.2.1 Introduction

The striking success of Ga[Al]As semiconductor heterostructures originates from the extremely high mobilities obtained in these materials. One key ingredient for the fabrication of such samples is modulation doping, where dopants and electrons are spatially separated. At low temperatures, impurity scattering, alloy scattering and interface roughness scattering limit the electron mobility [79, 65]. If more than one subband is occupied, intersubband scattering takes place in addition[54, 59, 73, 80].

Information on the relevant scattering processes is usually obtained by measuring how single-particle (τ_s) and Drude scattering times (τ) vary with carrier density n_H. For two-dimensional electron gases (2DEGs) realized in AlGaAs heterostructures, it is found that impurity scattering is dominant. Due to screening, one finds $\tau \propto n_H^\gamma$, with γ between 1 and 1.5, depending on the distance between the dopants and the 2DEG [79].

In a two-subband system with subband densities n_0 and n_1, the Drude scattering times τ_i of subband i are usually found to increase monotonically with n_i [71, 75]. Recent results show that in a parabolic quantum well (PQW), τ_0 may also slowly decrease, i.e. $\gamma < 0$, when a second subband is occupied [76, 77]. In the following, we investigate this unusual dependence and show that it may be due to a certain arrangement of the ionized impurities.

4.2.2 Experimental

The inset of Fig. 4.2a shows the structure of the sample. In the center of the well, a three monolayer thick $Al_{0.05}Ga_{0.95}As$ layer forms a potential spike. The experiments were carried out with standard Hall-bar geometries at temperatures of 100 mK. Four-point measurements using a current of 10 nA at a frequency of 13 Hz were performed with a magnetic field B applied perpendicular to the electron gas.

Figure 4.2a shows a measurement of the magnetoresistivity $\rho_{xx}(B)$ at $n_H = 2.9 \cdot 10^{15}\,\mathrm{m}^{-2}$. From the low-field magnetoresistivity, τ_0 and τ_1 are obtained by fitting to the two-subband model described in section 4.1.4.

We measured $\rho_{xx}(B)$ at $n_H = 2.9 \cdot 10^{15}\,\mathrm{m}^{-2}$ (controlled by the low-field Hall voltage) and different positions of the electron distribution along the growth direction (Fig. 4.2b). The electrons were displaced by applying voltages U_{fg} (U_{bg}) between the front (back) gate electrode and the electron gas.

Variations of both amplitude and period of the Shubnikov-de Haas (SdH) oscillations with changing V_{fg} are clearly visible. The amplitude at a fixed magnetic field decays as the wave functions are displaced towards the substrate. This corresponds to a decreasing τ_s[80, 81]. An analysis of τ_s is presented in section 4.5.

As described in chapter 2.6.2, we find the displacement Δz per front gate voltage by fitting U_{bg} as a function of U_{fg} at constant n_H to a capacitor model. For $n_H = 2.9 \cdot 10^{15}\,\mathrm{m}^{-2}$, we obtain a displacement of 1000 Å/V[41]. Thus we can plot the data as a function of Δz instead of gate voltages.

From the SdH frequency we evaluate $n_0(\Delta z)$ (Fig. 4.3a). A minimum occurs in n_0 at $U_{fg} \approx -130\,\mathrm{mV}$ and is related to the narrow potential spike in the center of the PQW. The spike leads to subband energy shifts depending sensitively on the electron distribution along the growth direction. A displacement of the electrons thus changes n_0 and n_1. The difference between the two lowest subband energies is minimal when the wave functions are centered with respect to the spike. Therefore, the minimum in n_0 provides the reference for the location of the wave functions in growth direction[47], where $\Delta z = 0$.

4.2.3 Determination of Drude Scattering Times

By fitting the magnetoresistance data with Eq. 4.29, we evaluated τ_0 and τ_1 for different Δz (Fig. 4.3a). The lower-subband scattering time τ_0 is found to be larger than τ_1. Both τ_0 and τ_1 show a maximum as a function of Δz. The maximum in τ_1 occurs where the wave functions are centered, i. e. $\Delta z = 0$.

Assuming a decrease of τ_i with decreasing n_i due to screening ($\gamma > 0$), we expect a minimum in τ_0 at $\Delta z = 0$, which disagrees with the measurement. On the other hand, the scattering rate depends on the distances from the relevant scatterers [82]. For $\Delta z = 0$, the electrons are as far away as possible from the ionized impurities, which gives rise to large τ_i. The fact that τ_0 is large around $\Delta z = 0$ indicates that the density-dependence is weaker than the dependence on the distance to the relevant scatterers. In contrast to the n_0 subband, both, n_1 and τ_1 have a maximum at $\Delta z = 0$. The relative change of n_1 with Δz is larger than that of n_0. Hence, τ_1 is more strongly influenced by its density dependence than by Δz, which explains the coincidence of the maximum in τ_1 with $\Delta z = 0$.

The maximum of τ_0 is shifted towards the surface, indicating stronger scattering on the substrate side. Although this could be explained by assuming more dopants than expected from the MBE growth protocol, we can exclude this, because the total amount of Si brought on the wafer was measured accurately. However there might be segregation of dopants on the substrate side towards the PQW during growth, which would enhance scattering significantly.

Additional insight can be gained by studying the spatial variation of the matrix elements K_i (Fig. 4.6a). Usually, Drude scattering times are insensitive to small-angle scattering. For intersubband scattering, K_3 contains the part of the scattering rate weighted by $\cos\vartheta$. This gives information about the amount of small-angle intersubband scattering. Since almost no structure in K_3 is observed, while K_1 increases stronger on the substrate side, large-angle scattering must be higher on the substrate side. In order to increase large-angle scattering of Coulomb scatterers with fixed density, the distance to the electron gas has to be diminished. This happens if scatterers segregate towards the electron gas.

4.2.4 Determination of Single-Particle Scattering Times

The single-particle scattering time τ_s determines the width of the Landau levels and thus the amplitude of the oscillations in the DOS in the presence of a magnetic field. From the amplitude of the SdH oscillations, τ_s from the lower-energy subband is obtained by fitting the amplitude $\Delta\rho$ of the SdH-oscillations by [80]

$$\frac{\Delta\rho}{\rho_{xx}(0)} = -4 D_T \left(2\pi^2 \frac{k_B T}{\hbar\omega_c}\right) e^{\frac{-\pi}{\tau_s \omega_c}}, \tag{4.32}$$

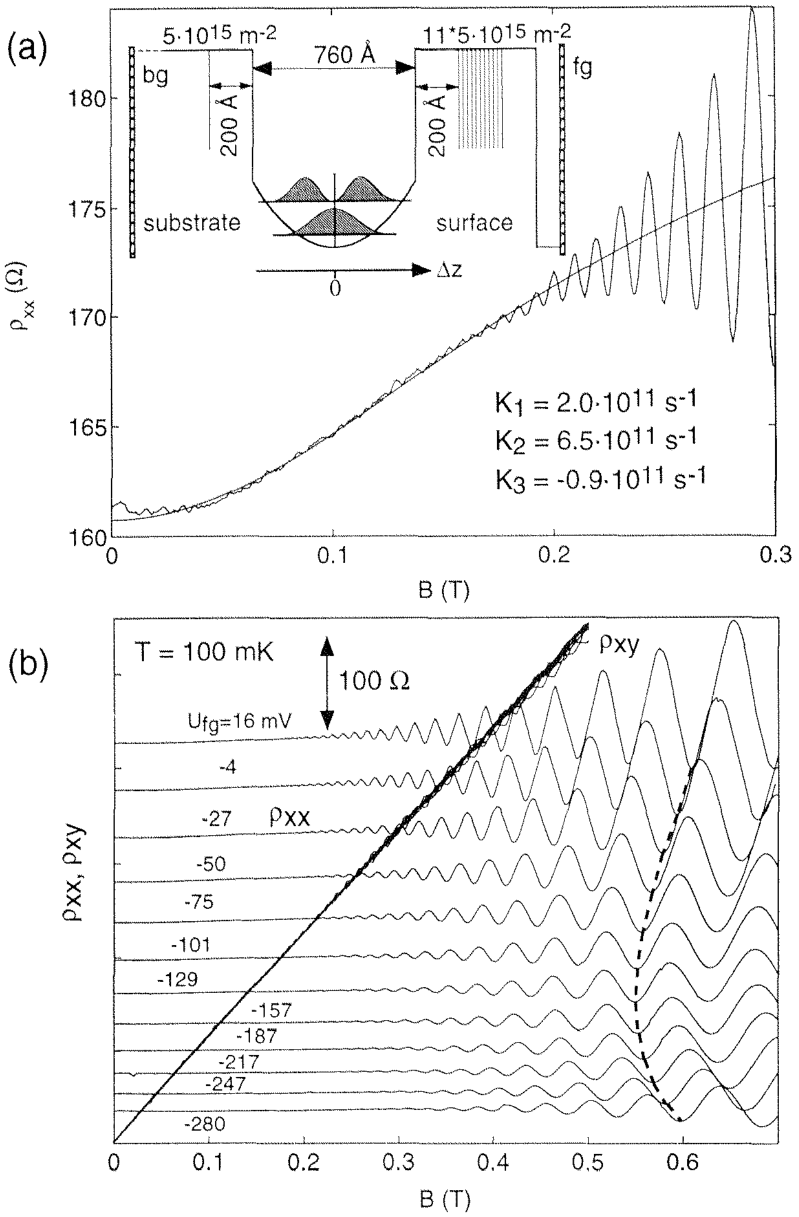

Figure 4.2: (a) Fit of $\rho_{xx}(B)$ for U_{fg}=-50 mV (U_{bg}=+1000 mV) to the two-subband scattering model. Inset: schematic sample layout along the growth direction. (b) Set of measured $\rho_{xx}(B)$ for different electron positions along the growth direction at $n_{\text{H}} = 2.9 \cdot 10^{15}\,\text{m}^{-2}$. Values for U_{fg} are indicated, and U_{bg} is varied between -2.2 V (top) and +2.2 V (bottom) in steps of 0.4 V. Subsequent data are offset for clarity by 50 Ω. From top to bottom, the electron distribution is displaced towards the substrate. The data for ρ_{xy} fall on top of each other since n_{H} is constant. One set of minima corresponding to the same filling factor in the lower subband are connected by a dashed line.

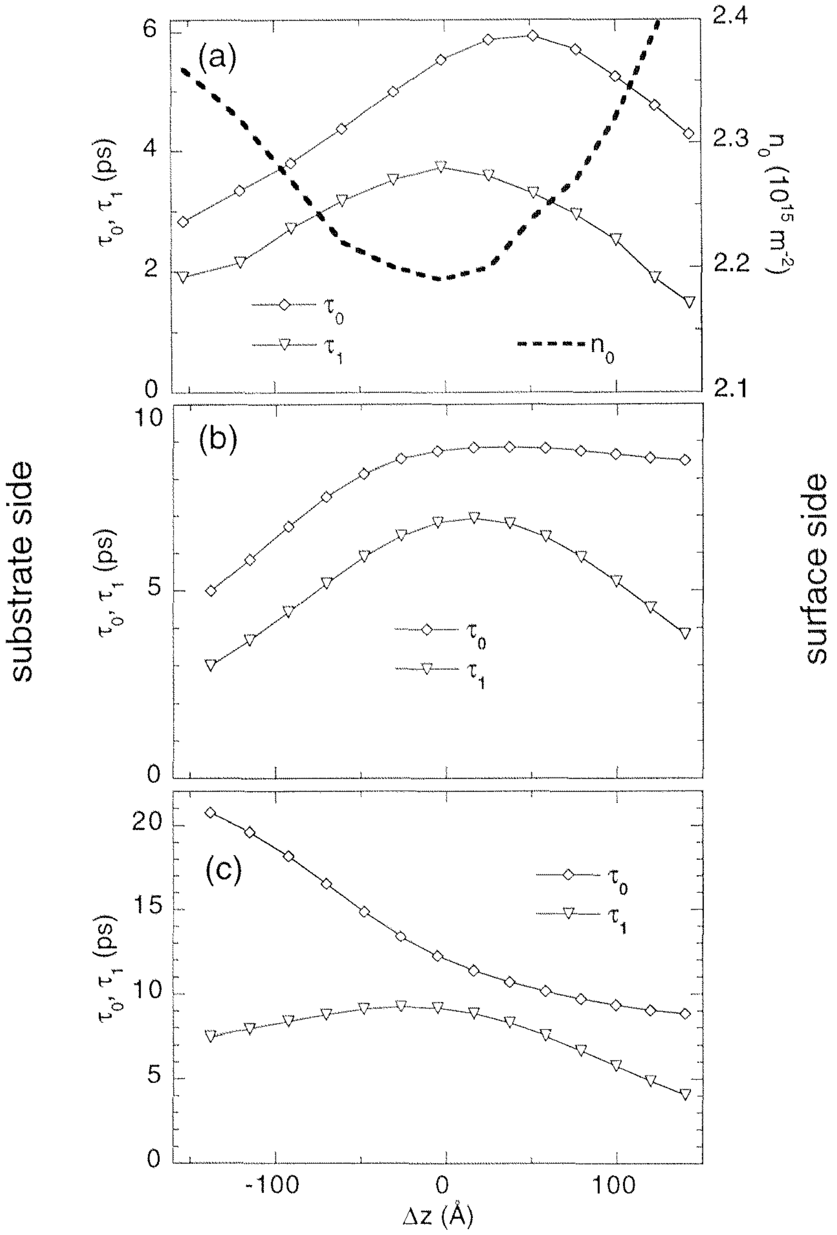

Figure 4.3: (a) Measurement of τ_0, τ_1 and n_0 vs Δz at $n_H = 2.9 \cdot 10^{15}\,\mathrm{m}^{-2}$. (b) Calculated scattering times for a scattering distribution where $1.5 \cdot 10^{15}\mathrm{m}^{-2}$ of dopants are shifted from the substrate side towards the PQW, showing good agreement with the measured data. (c) The same calculations as in (b), but with the dopants as in the growth protocol.

where the Dingle term is $D_T(X) = X/\sinh X$. At low temperatures T and high magnetic fields, the Dingle term approaches unity. Figure 4.4 shows a logarithmic plot of the left side of Eq. 4.32 divided by the Dingle term, as a function of $1/B$, for a measurement on a PQW. In this representation, the SdH amplitude decays as $\log 4 - \pi/\tau_s\omega_c$, i.e. linearly with $1/B$. From the slope of the linear curve one obtains τ_s. Because the SdH-oscillations are due to the subband $i = 0$, we interpret the obtained τ_s as the single-particle scattering time of the $i = 0$ subband. Single-particle scattering times for two occupied subband have been determined in a 2D heterjunction structure [83].

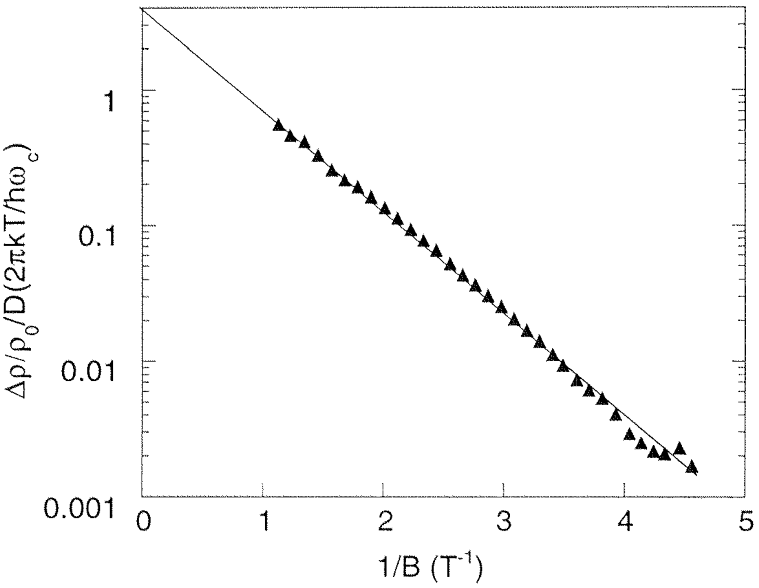

Figure 4.4: Dingle plot: logarithm of the SdH-amplitude divided by the Dingle term (Eq. 4.32), as a function of the inverse magnetic field. Taken for $U_{\mathrm{bg}} = 600\,\mathrm{mV}$ and $U_{\mathrm{fg}} = -157\,\mathrm{mV}$ (sample 21, $x = 0.05$). The slope of the linear fit determines the single-particle scattering time τ_{s0}.

An analysis of τ_s is presented in Fig. 4.5. In the measured data we observe a decrease of τ_s, as the wave functions are displaced from the front gate side to the back gate side, where nominally less ionized impurities are located. This indicates once more that on the back-gate side there either have to be more scatterers, or the scatterers are closer to the PQW than expected. The values for τ_s are about ten times smaller than the Drude scattering times τ_0. Because in τ_0 the forward scattering events are counted less than in τ_S, this means that electrons in the PQW are scattered predominantly by small angles ϑ. This is explained by the flat potential produced by the remote ionized impurities. In calculations the ratio τ_0/τ_s typically reaches values of 100. It has been shown by Coleridge [84] that spatial correlation of small-angle scattering events can significantly increase the single-particle scattering time compared to calculated values, while the change in the Drude scattering time is less pronounced.

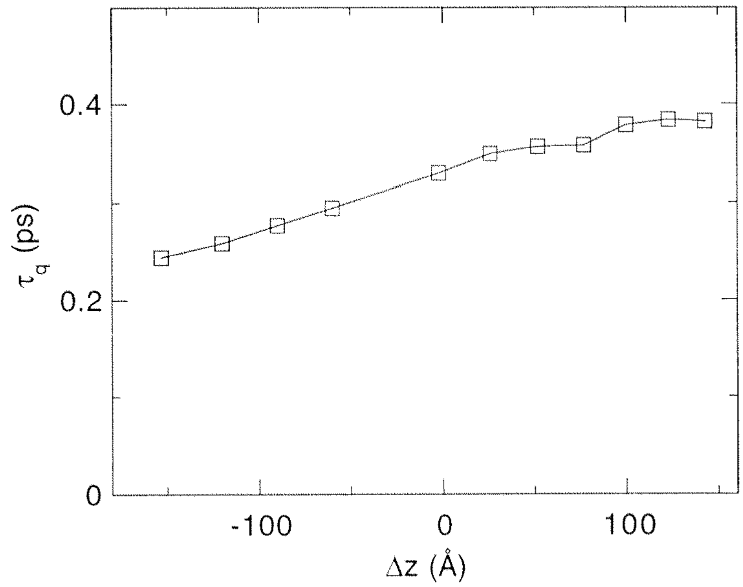

Figure 4.5: Measured τ_s for different positions of the electron gas across the quantum well. Towards the back-gate side, τ_s monotonically decreases, indicating that there have to be more scattereres or the scatterers are located closer to the well than on the front-gate side.

4.2.5 Calculation of the Scattering Times

As we will show, a calculation of the τ_i supports the assumption of segregated Si atoms. The matrix elements of the scattering potential were obtained by numerical integration using self-consistently calculated wave functions. Then the transition rates $P_{nm}^{(i)}$ were calculated by integrating the squared matrix elements over the allowed scattering vectors. Screening was included in the Thomas Fermi approximation. In Appendix A we compare Thomas Fermi screening with the RPA formalism introduced in section 4.1.2. We find that Thomas Fermi screening gives results similar to RPA screening if a third virtually occupied subband is taken into account. For the two-subband RPA formalism, the results clearly differ. Because of limited computing time, we present here the Thomas Fermi results here.

The τ_i were calculated from Eq. 4.29. Besides Coulomb scattering, we included alloy scattering and interface roughness scattering in the calculation. We found that the scattering rate is dominated by Coulomb scattering. Therefore the other scattering mechanisms could be neglected the in the calculations presented in the following.

Initially, two layers of Coulomb scatterers were included. The dopants on the surface side were gathered in a single δ-layer 300 Å above the well, with a concentration of $N_1 = 3 \cdot 10^{16}\,\mathrm{m}^{-2}$. The second layer is the doping layer 200 Å below the well ($N_2 = 2.8 \cdot 10^{15}\,\mathrm{m}^{-2}$). These values correspond to half of the nominal Si concentration brought on the wafer during the MBE-growth, qualitatively accounting for deep donors and non-ionized impurities. Figure 4.3c shows the obtained scattering times. As one would expect for this donor configuration, τ_0 monotonically increases as the electrons are displaced towards the substrate side, which is not in agreement with the measured data (Fig. 4.3a).

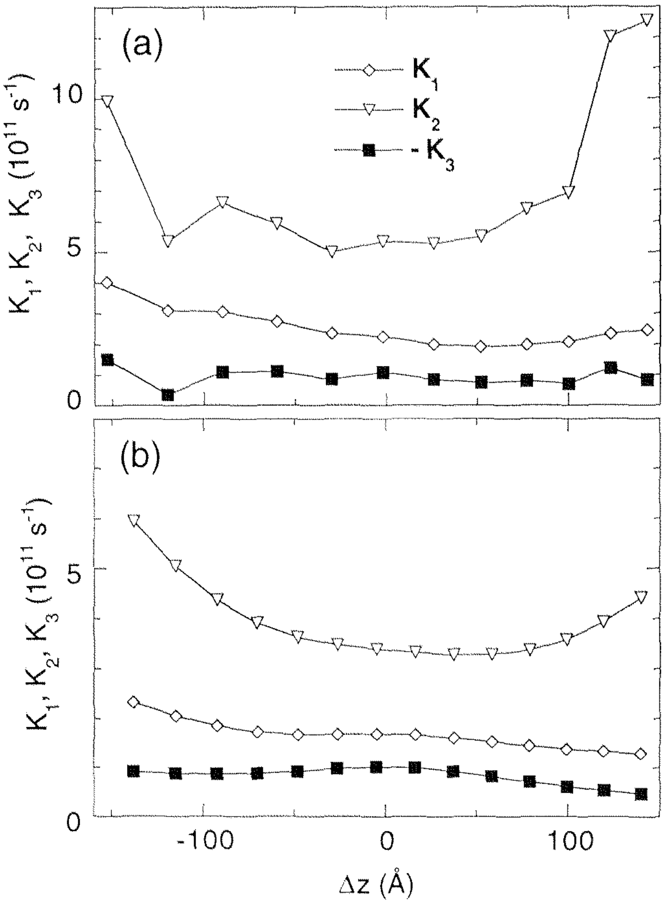

Figure 4.6: Measured (a) and calculated (b) K_1, K_2 and $-K_3$. In (b), ionized impurity scattering was modeled as in Fig.4.3c.

In order to take segregated Si atoms into account, we placed $N_3 = 1.5 \cdot 10^{15}\,\mathrm{m}^{-2}$ scatterers at the edge of the well on the substrate side, and reduced N_2 by the same amount (Fig 4.3c). As in the experiment, we obtain a maximum in τ_0 displaced towards the surface side and a maximum of τ_1 at $\Delta z = 0$. At the surface side, τ_0 decreases only slowly, saturating at a value comparable to the simulation with $N_3 = 0$. It is the balance between the monotonically decreasing τ_0 shown in Fig. 4.3c, and the range and strength of the extra layer, which determines the exact shape of $\tau_0(\Delta z)$

The calculated scattering times are about 50 percent larger than the measured ones. It is well-known that for PQWs calculations overestimate the scattering times. Possible explanations are size-effect scattering from the edges of the electron gas [85] or enhanced background impurities due to the greater reactivity of Al with oxygen and carbon-containing molecules in the MBE chamber. In addition, the calculated values depend on how screening of the scattering potential is implemented and which concentration of ionized impurities is assumed. We did not attempt to simulate τ_i accurately. Here only the qualitative behavior, in particular its spatial dependence, is of importance.

The calculated K_i nicely reproduce the experimental data (Fig 4.6b).

4.2.6 Density-Dependence of the Scattering Times

With this strong evidence for segregated scatterers at the substrate side of the well, we come back to the previously unexplained structure in the density-dependence of τ_i [77]. In this experiment, U_{bg} was kept fixed, while U_{fg} and therefore n_{H} was changed. In Fig. 4.7, the measured and calculated values for τ_0, τ_1, n_0 and n_1 are shown. In the measurement, τ_0 slightly decreases as n_1 gets populated. In the calculation, the additional scattering layer gives rise to a weak increase of τ_0 with n_{H} when the second subband is occupied (large symbols), whereas a steep decrease results in the case of no additional layer (small symbols). Thus the additional scatters are responsible for the slope of $\tau_0(n_{\mathrm{H}})$. Since n_{H} is driven by V_{fg}, the electron distribution expands towards the surface side with increasing n_{H}. Thus the scatterers on both sides of the well compete and determine the shape of $\tau(n_{\mathrm{H}})$. As discussed above, for small n_1, τ_1 is not so sensitive to additional scatterers, which is reflected in similar values obtained from the two simulations shown in Fig. 4.7b.

4.2.7 Conclusions

In conclusion, we have presented an investigation of Drude scattering times in a modulation-doped multi-subband quantum well. Using front- and back gate voltages, the position of the electron distribution and the subband densities were tuned. The Drude scattering times of individual subbands were measured. It was found that τ_0 is dominated by the distance of the 2DEG to the impurities and not by its density dependence. Its behavior could therefore be used to locate additional scatterers at the substrate edge of the well, which are presumably due to segregation of dopants during growth. The measured scattering times could be qualitatively reproduced in a calculation assuming that half of the substrate-side donors have diffused to the edge

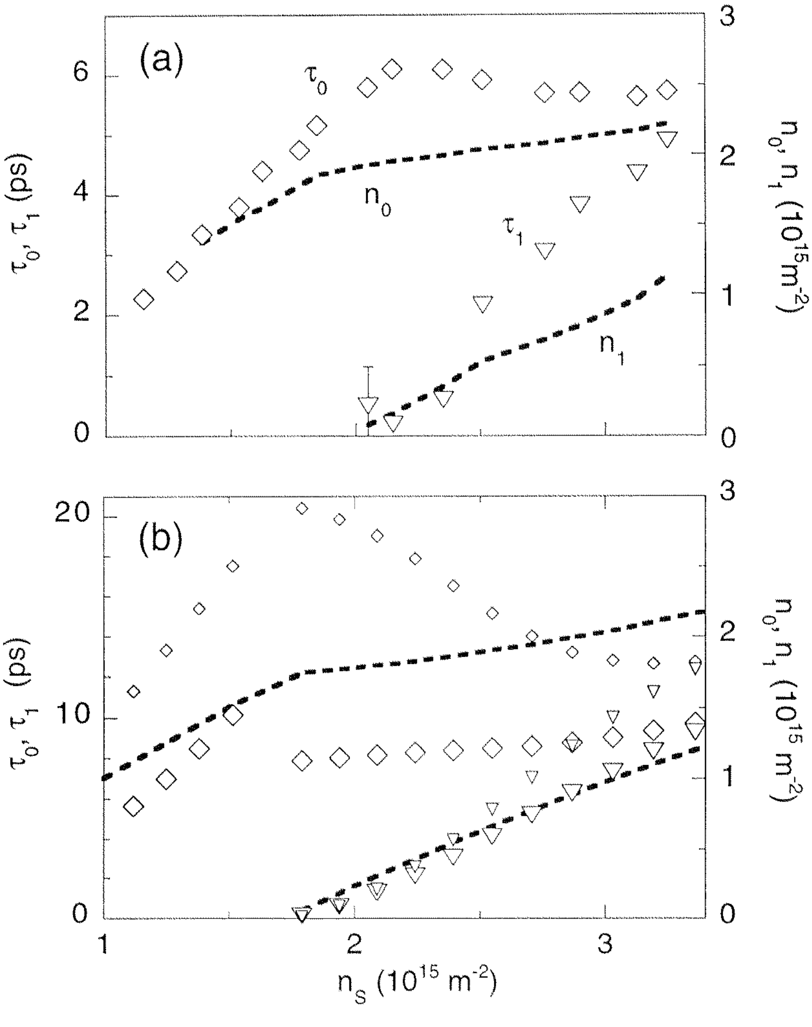

Figure 4.7: Measurements (a) and calculation (b) of scattering times (symbols) and subband densities (lines) vs n_{H}. In (b), small symbols are calculated without, large symbols with additional impurities at the substrate side of the well. The jumps at the population of the second subband comes from the non-continuous DOS which modifies screening abruptly.

of the well. Using these results, previous measurements of the density dependence of τ_0 could be explained. While obtained for a PQW, the presented method of investigating the scattering times as a function of the electron-gas position might yield further information on scatterers in other types of samples.

Chapter 5

Phase-Coherent Transport

In this chapter, we present measurements of weak localization (WL) and universal conductance fluctuations (UCF), two effects arising from phase-coherent electron transport. Contrary to inelastic scattering processes, correlations in the quantum-mechanical phase of electrons are not destroyed by elastic impurity scattering. This leads to phase-coherent transport over a length l_ϕ, which can be significantly larger than the elastic scattering length l_{el}. The coherence of a quantum-mechanical system is a prerequisite for quantum computing, a topic which has been discussed a lot recently [86, 87, 88].

The WL and UCF effect manifest themselves as quantum interference corrections to the Drude resistivity, which are important at low temperatures. With the PQW system, we can investigate the phase-coherence length at the crossover from a two- to a three-dimensional electron gas.

5.1 Phase-Coherence Length

In the description of electron transport by the Boltzmann equation, the electrons are assumed to move along classical trajectories between two scattering events. If interference of scattering from different centers cannot be neglected, the motion of electrons is described by quantum-mechanical waves with a phase ϕ oscillating in time and space. This phase is well-defined as long as no scattering events modify the energy of the electron. The loss of phase is called decoherence. A length scale l_ϕ is defined, which measures the distance an electron travels until its ability to interfere with itself is lost. Imagine two Feynman paths [89] starting at point A and ending at point B. The ability of the two paths to interfere at point B is lost if the fluctuation of the acquired phase shifts is larger than say 2π. It is important that the environment randomizes the interfering particle's phase in an unpredictable way. The phase ϕ at point B is a statistical variable, which can be characterized by a distribution function $P(\phi)$. The phase-coherence length l_ϕ is defined such that on paths with a length l_ϕ the width of $P(\phi)$ – the variance of the phase ϕ – is 2π.

Elastic scattering of electrons by impurities and defects does not contribute to decoherence at low temperatures, because no energy transfer to the defect is possible [90]. However under certain conditions, if an internal degree of freedom as spin is involved, dephasing can occur in the absence of any inelastic process, as was pointed out in Ref. [91]. Thus inelastic processes as scattering of electrons with other electrons or spin-flip-processes are mainly responsible for decoherence. An electron needs the time $\tau_\phi = l_\phi^2/D$ to travel the distance l_ϕ diffusively (D is the diffusion constant). Theoretically it is found that the phase-coherence time τ_ϕ increases with decreasing temperature as $\tau_\phi \propto 1/T^p$, where p varies between 0.5 and 3 [92, 91, 93, 94]. However many experiments show a saturation of τ_ϕ at low temperatures, which has been ascribed to residual heating of the electron gas by the environment or by spin-flip scattering processes due to magnetic impurities. Only recently these two mechanisms could be clearly excluded [95]. A new, but controversial theory was proposed, where electron scattering by zero-point fluctuations of the intrinsic electromagnetic environment explains the low-temperature saturation of τ_ϕ [95, 96]. An alternative explanation was proposed by Altshuler which is based on dephasing by an external microwave field [97].

Theories describing the behavior of τ_ϕ as a function of the electron density do exist for strictly 2D electron motion and for the case of 3D motion like in thin metal films [98, 99]. To our knowledge no work has been done to investigate the influence of intersubband scattering on phase coherence. We therefore investigate what happens to phase coherence if a second subband is populated, i.e. at the crossover from 2D to 3D.

We focus on two effects due to phase coherence, which can be used to measure τ_ϕ:

- At $B = 0$, there is a peak in $\rho_{xx}(B)$. This is the so-called weak-localization (WL) peak.
- The conductance fluctuates as a function of some external parameter, like U_{sg} or B (universal conductance fluctuations, UCF).

Making use of these two effects, we present in the two following sections investigations of phase-coherent transport in PQWs.

5.2 Weak Localization

Weak localization is observed in the magnetoresistivity of 2DEGs at low temperatures. Around $B = 0$ a peak in $\rho_{xx}(B)$ occurs (Fig. 5.1). The explanation for this relies on phase coherence leading to an enhanced backscattering probability due to time-reversal invariance of pairs of clockwise and anticlockwise paths [92, 100, 34]. This coherent backscattering leads to a reduction of the diffusion constant and correspondingly to a reduced conductivity. The conductivity reduction at $B = 0$ due to coherent backscattering is denoted by $\Delta\sigma_0$. It depends on the channel width W. For one occupied subband, $W > l_\phi$ and for $\tau_{\text{el}} \ll \tau_\phi$ an expression for $\Delta\sigma_0$ is obtained [34]:

$$\Delta\sigma_0 = -\frac{e^2}{2\pi^2\hbar} \ln\left(1 + \frac{\tau_\phi}{\tau_{\text{el}}}\right). \tag{5.1}$$

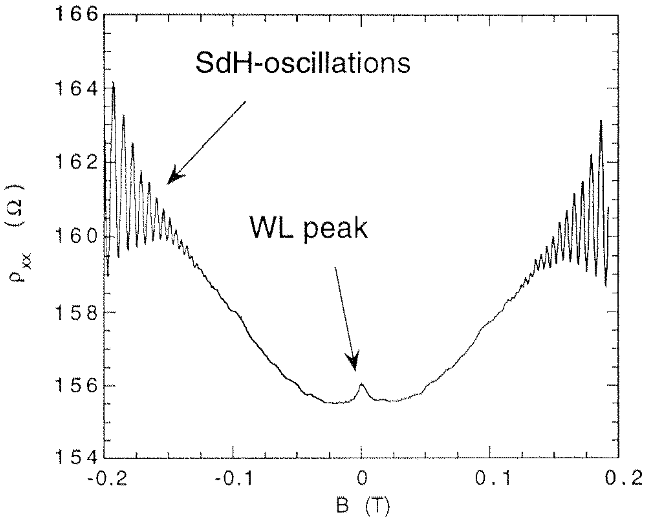

Figure 5.1: Weak-localization peak in the magnetoresistance measured on a PQW in the two-subband regime at $T = 100\,mK$.

The conductance reduction increases logarithmically with τ_ϕ and is of order e^2/h. A magnetic field breaks the symmetry of time-reversed paths, and the enhanced backscattering disappears successively with increasing field. The conductance increases to its classical value. A typical field can be derived, at which the WL peak disappears. Consider a loop over which an electron propagates phase-coherently. Let the loop length be L. The area enclosed by the loop is $F \approx L^2$. A magnetic flux through this area shifts the electron phases with respect to each other by $2\oint e\mathbf{A}ds/h = 2eBF/h$. Interference is lost if the phase shift gets larger than unity, i.e. $F > h/2eB$. The stronger the magnetic field, the smaller are the loops which still contribute to WL, until finally the conductance reaches its classical value. On the other hand, loops which are larger than the phase-coherence length $l_\phi = \sqrt{D\tau_\phi}$ do not contribute. Thus if the field reaches a value ΔB where loops of size smaller than l_ϕ^2 start to loose their phase, the conductance starts to increase. The condition for this is given by

$$F \approx l_\phi^2 = D\tau_\phi < \frac{h}{2e\Delta B} = \frac{l_B^2}{2}. \tag{5.2}$$

By measuring the magnetoresistivity peak, information about the phase-coherence time τ_ϕ is obtained:

- The peak-height is proportional to the logarithm of τ_ϕ: $\Delta\sigma_0 \propto \ln(1 + \tau_\phi/\tau_{\mathrm{el}})$.
- The width ΔB of the peak is given by $\Delta B \propto 1/D\tau_\phi$.

For arbitrary magnetic fields, a formula can be derived [92], which describes the exact shape of $\rho_{xx}(B)$ for given τ_ϕ and τ_{el}. We tried to fit magnetoresistance data of a PQW with this formula [76]. A parabolic background in the magnetoresistance attributed to electron-electron interaction had to be considered [34]. Figure 5.2 shows a fit of

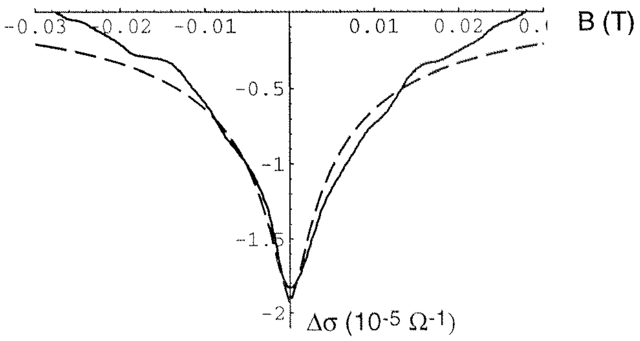

Figure 5.2: Fit of the WL conductivity correction $\Delta\sigma(B)$ for sample 21 with $x = 0.05$, $U_{\mathrm{bg}} = 0\,\mathrm{mV}$ and $U_{\mathrm{fg}} = -340\,\mathrm{mV}$.

the WL peak in $\sigma_{xx}(B)$ measured for $n_{\mathrm{H}} = 1.2 \cdot 10^{15}\,\mathrm{m}^{-2}$. The obtained value for τ_ϕ is 14 ps, the elastic scattering time $\tau_{\mathrm{el}} = 2.6\,\mathrm{ps}$. The quality of the fits deteriorated when we went to higher densities. The formula describing $\sigma(B)$ is not strictly valid any more for two reasons:

- With increasing density the elastic scattering time τ_{el} might increase stronger than τ_ϕ, we are thus no longer in the regime $\tau_{\mathrm{el}} \ll \tau_\phi$.
- The system is not strictly 2D any more at the crossover from one to two populated subbands.

As there is no theory describing $\rho_{xx}(B)$ that takes intersubband scattering into account and is valid for $\tau_{\mathrm{el}} \approx \tau_\phi$, we have concentrated on the evaluation of the height $\Delta\sigma_0$ and width[1] ΔB of the WL-peak. Going from one to two occupied subbands, we have observed a change in both quantities (Fig. 5.3). First we discuss the density-dependence for one occupied subband ($U_{\mathrm{fg}} < -220\,\mathrm{mV}$):

- The peak height $\Delta\sigma_0$ increases with density. If $\Delta\sigma_0$ is proportional to $\ln(1 + \tau_\phi/\tau_{\mathrm{el}})$, this means that τ_ϕ increases faster than τ_{el}, i.e. if $\tau_{\mathrm{el}} \propto n_{\mathrm{H}}^k$ then $\tau_\phi \propto n_{\mathrm{H}}^{k'}$ with $k' > k$.
- The width ΔB slightly increases for $U_{\mathrm{fg}} < -220\,\mathrm{mV}$. Because D increases with n_{H}, this would signify that τ_ϕ is decreasing with n_{H} if $\Delta B \propto 1/D\tau_\phi$. This is in contradiction to the interpretation of the $\Delta\sigma$ data.

Both the width and the height decrease with subband density if a second subband is populated ($U_{\mathrm{fg}} > -220\,\mathrm{mV}$), again giving contradictory results for τ_ϕ. To sum up, we observed a change in the behavior of the WL-peak at the crossover from one to two occupied subbands. Both the width and the height of the peak increase with density for one occupied subband, and decrease for two occupied subbands. No conclusions can be drawn on the magnitude of the dephasing time τ_ϕ because there is no appropriate theory available.

---

[1] ΔB was defined by $\Delta\sigma(\Delta B) = \Delta\sigma_0/2$.

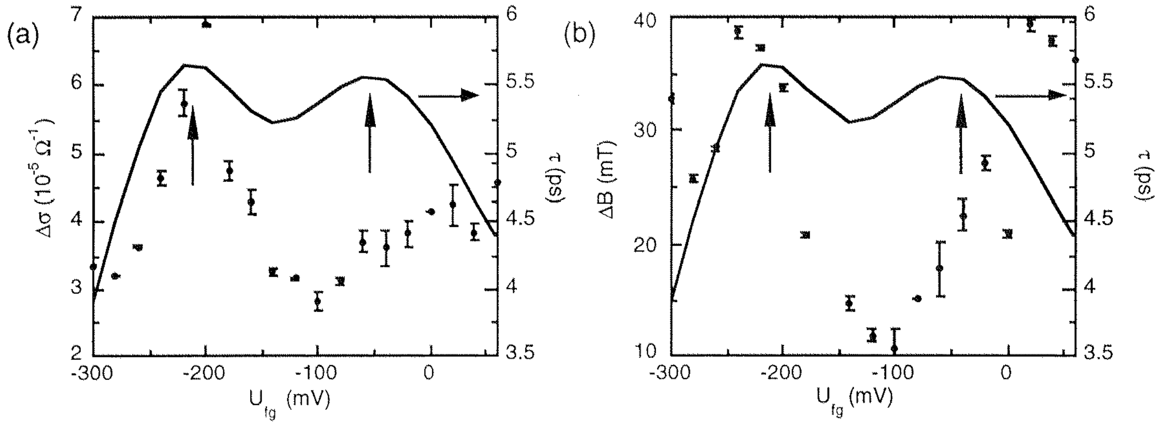

Figure 5.3: Measured height $\Delta\sigma_0$ (a) and width ΔB (b) of WL peak (symbols) vs U_{fg}, measured at $U_{\mathrm{bg}} = 0\,\mathrm{V}$ on sample 21 with $x = 05$. The lines connect measured mobility data points (right axis), which indicate the occupation of the second and third subband (arrows).

5.3 Universal Conductance Fluctuations

Quantum interference effects lead to significant sample-to-sample fluctuations in the conductance for samples that differ only in the positions of their respective scatterers. Experimentally it is difficult to compare conductance fluctuations among different samples. More conveniently a magnetic field is applied to one sample, as a small change in magnetic field has a similar effect on the interference pattern as a change of the sample impurity configuration. The magnitude of the conductance fluctuations is characterized by the standard deviation of the conductance G

$$\Delta G = \left\langle (G - < G >)^2 \right\rangle^{1/2} . \tag{5.3}$$

Such universal conductance fluctuations (UCF) are observed in the magnetoresistance of 2DEGs if the sample is not very much larger than l_ϕ. The magnitude ΔG is of order e^2/h at $T = 0$ [98, 101], irrespective of the sample conductance G.

PQWs enable to tune the electron density of the system and thus to investigate UCF with one to three occupied electric subbands. Here, the transition from one to two occupied subbands, which represents a dimensional crossover from a pure 2D system to an intermediate regime between 2D and 3D, is particularly interesting [105, 106]. The experiments presented here have been carried out within a Diploma thesis of M. Huberty [103].

5.3.1 Theory

Unlike the WL reduction of backscattering due to phase coherence, the interference between paths contributing to UCF are reduced statistically when many phase-coherent sections of a sample are put in series. Thus the fluctuation magnitude decreases if the distance L between two voltages probes is made larger. If the width W of the sample is smaller than l_ϕ, the root-mean-square magnitude of the conductance fluctuations can be written in the form

$$\Delta G = \frac{e^2}{h}\left(\frac{C_1 l_\phi}{L}\right)^{3/2}, \tag{5.4}$$

where C_1 is of order unity and a function of the typical length scales of the sample, i.e. the elastic scattering length l_{el}, the channel width W and the channel length L [34]. In principle, the dependence of $\Delta G \propto l_\phi^{3/2}$ allows the determination of l_ϕ, however the value of C_1 has to be known to evaluate l_ϕ quantitatively.

Similarly to the width of the WL peak, a correlation field ΔB_c can be defined. For ΔB larger than ΔB_c, the fluctuating conductance at field B is uncorrelated with the conductance at $B + \Delta B$. For $T = 0$ and $W < l_\phi$, one obtains [102]

$$\Delta B_c = \frac{h}{eWC_2 l_\phi}. \tag{5.5}$$

With both, ΔB_c and ΔG, the phase-coherence length l_ϕ can be evaluated from measured $\rho_{xx}(B)$ traces.

5.3.2 Experimental setup and data evaluation

Figure 5.4 shows the geometry of the sample we used (sample 43D1). The length L between two voltage probes varies between $1.5\,\mu$m and $11\,\mu$m. The Hall bar width W is $2\,\mu$m. We also fabricated samples with $W = 1\mu$m, where, however, the voltage probes were pinched off and no transport measurements were possible. The samples were structured using e-beam lithography. In the first step, a front gate was defined, serving as a self-aligned etch-stopper for the following mesa-etching step. Thus gate and Hall-bar could be aligned very precisely.

Figure 5.5 shows a measurement of the density and mobility of a sample. The mobility is reduced by a factor of about two compared to the values for wider Hall bars, indicating the influence of the edges.

We measured magnetofluctuations in the conductance of PQW samples which we can establish as UCF. In a magnetic field perpendicular to the 2DEG, we were able to extract very reasonable estimates of the fluctuation amplitudes and correlation fields. Fig. 5.6a shows an example of a measurement of $\rho_{xx}(B)$. The data has been fitted by a polynomial of power 6. In Fig. 5.6b, the difference of the background and the measured resistance is presented. Via matrix inversion, the fluctuations in G are obtained (Fig 5.6c). The amplitude ΔG is found to be proportional to $L^{-3/2}$ [103], indicating that $l_\phi > W = 2\mu$m. The observed correlation field is about

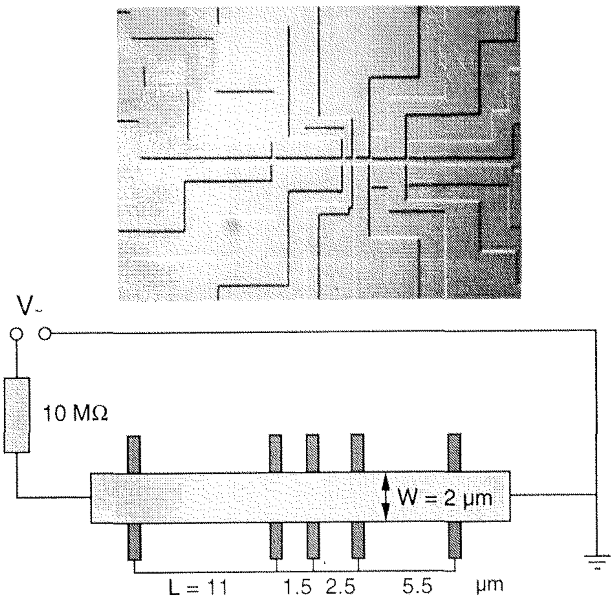

Figure 5.4: Photograph and scheme of the $2\,\mu$m thick UCF sample.

5 mT, independent of the sample size L. Very crude estimates of the length l_ϕ can be made from this data, shown in Fig. 5.7.

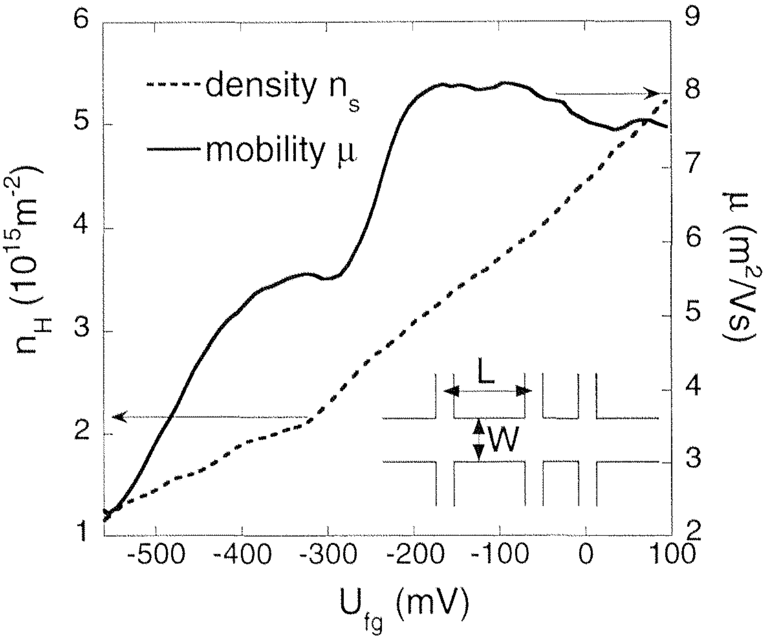

Figure 5.5: Electron sheet density and mobility as a function of U_{fg}.

Fig. 5.7 summarizes the magnitudes of $C_1 l_\phi$ and $C_2 l_\phi$ as obtained from correlation fields and fluctuation amplitudes. The numerical prefactors C_1 and C_2 probably depend on the gate voltage. The relevant length scales l_{el}, l_ϕ and W are all comparable. Theories exist only for asymptotic regimes, where different length scales can be well separated. In the intermediate regime, the prefactors C_1 and C_2 are expected to depend sensitively on changes in the decisive length scales. For $l_\phi > W$, a flux cancellation effect leads to additional structure in the prefactors [104].

The quantity $C_i l_\phi$ displays a dip at the second-subband occupation threshold and a strong increase at higher densities. This resembles the behavior of l_{el}. Possible explanations are [105, 106]

- The dependence of C_1 and C_2 is dominated by l_{el}.
- In the two-subband regime two channels fluctuate independently. This gives rise to an enhancement of the conductance-fluctuation amplitude.
- The phase-coherence length is influenced by electron-electron scattering, which on the one hand reduces τ_ϕ due to an increased phase space for scattering events, and on the other hand modifies screening, which may lead to a decrease of the scattering rate.

More theoretical work considering electron-electron intersubband scattering is needed to account for the observed dependencies.

In field orientations between the perpendicular and the in-plane case, the fluctuations scale with the perpendicular field component for one occupied subband. For two and three occupied subbands, this scaling disappears for large in-plane fields, which indicates a 2D/3D dimensional crossover [103].

Near the in-plane orientation and in-plane, we observe conductance fluctuations which depend on the in-plane component of the field. The fact that UCF is observed in a 2DEG with an in-plane field can be explained in two ways:

- For more than one subband occupied, the electrons can scatter between subbands, which enables motion along the z-direction. The electron system is in an intermediate regime between 2D and 3D, where flux-enclosing loops in an in-plane field configuration are possible.
- At magnetic fields where the magnetic length l_B is smaller than w, motion is essentially three-dimensional. This is due to the magnetic confinement which localizes the wave functions at z-positions which depend on the longitudinal momentum k_y (see inset of Fig. 5.8b) [107].

The typical loop size reduces from $l_\phi W$ to wW, such that the correlation field is expected to increase by $W/w \approx 2000/50 \approx 40$, see Eq.5.5. At the same time, the fluctuation amplitudes are smaller than in a perpendicular field. This is because an intersubband scattering event is needed for a closed loop, which is usually less probable than an intrasubband scattering event.

In Fig. 5.8a, measurements of the magnetoresistance R are shown for in-plane magnetic fields $B_{||}$ between 0 and 8 T. Dips in the magnetoresistance are related to subband depletions [74]. At $U_{\mathrm{fg}} = 130\,mV$, two dips are clearly resolved (arrows), and a weak third dip is observed (dashed arrow), indicating a partially populated fourth subband. In the different field regimes, we have different subbands occupied and can analyze the UCF quasi-period and amplitude.

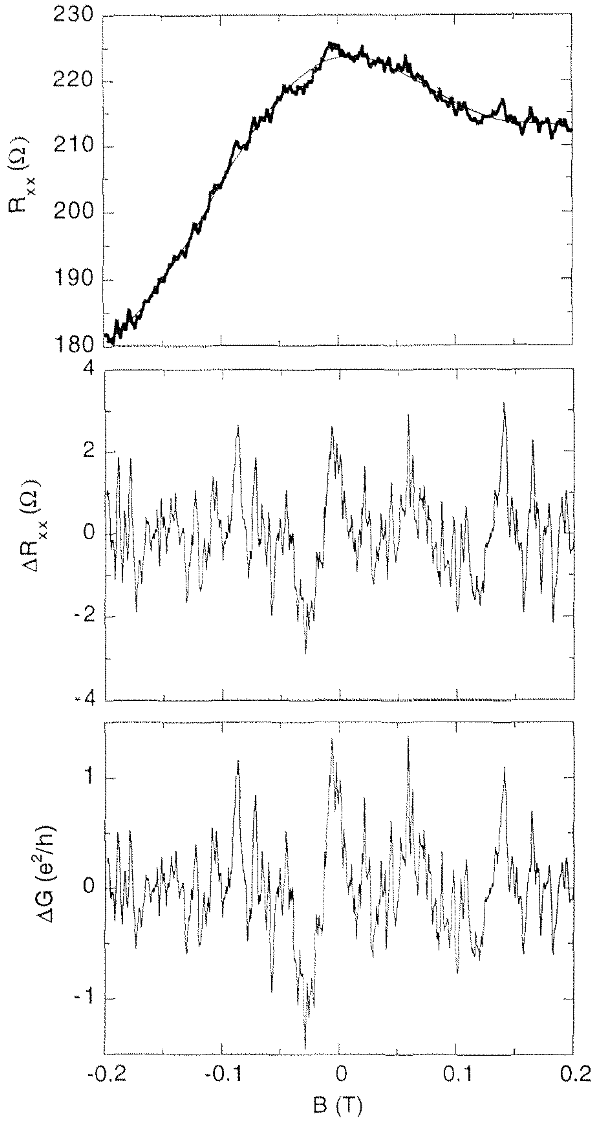

Figure 5.6: (a) Measured $\rho_{xx}(B)$ exhibiting UCF on top of a slowly varying background (smooth line). (b) Residuum ΔR of the polynomial fit shown in (a). (c) Calculated ΔG from ΔR through matrix inversion.

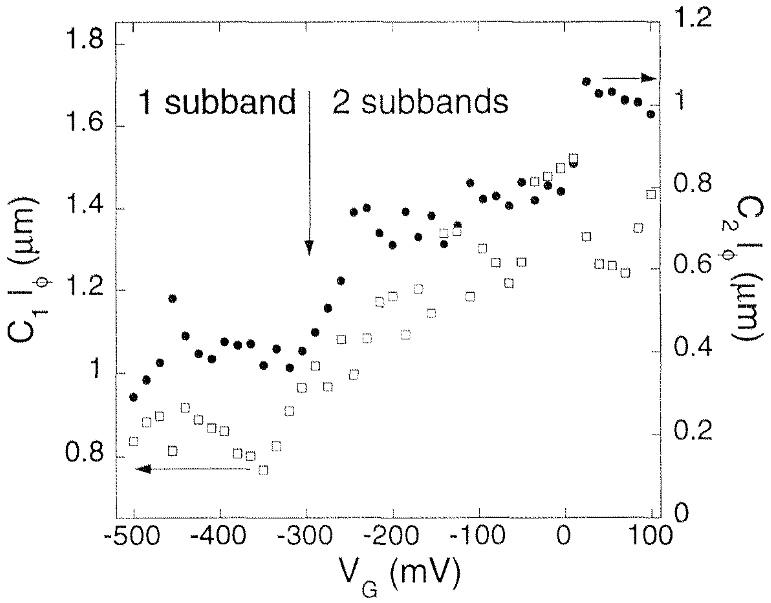

Figure 5.7: Phase coherence length as determined from the UCF amplitude δG $(C_1 l_\varphi)$ and from the correlation field ΔB_c $(C_2 l_\varphi)$. The resulting values have been averaged over different contact pairs.

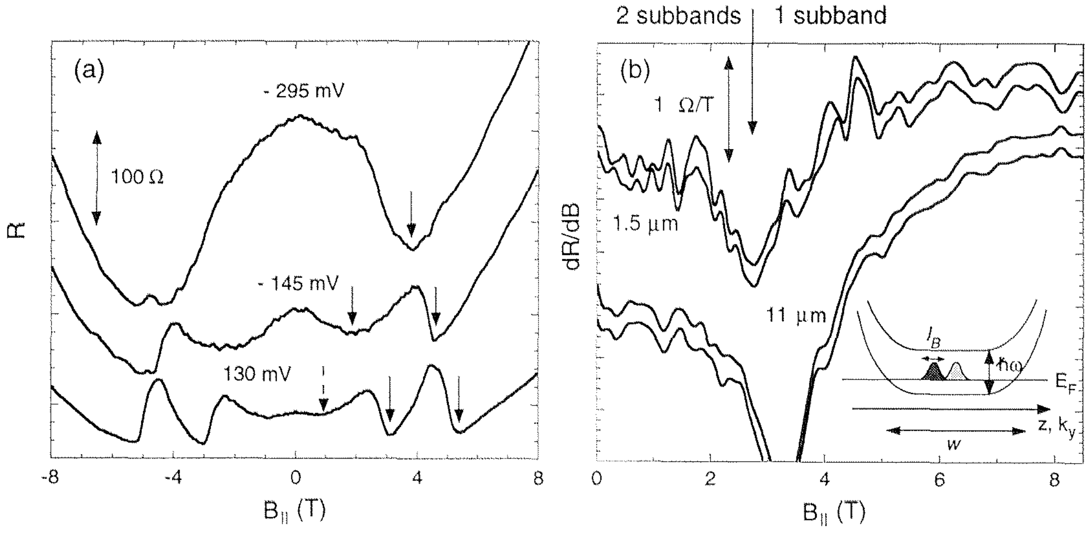

Figure 5.8: (a) Magnetoresistance R vs $B_\parallel$ for three different U_{fg}. The indicated dips denote field positions where 2D subbands are depopulated. (b) Differential magnetoresistance at $U_{\mathrm{fg}} = -295\,\mathrm{mV}$ for two contact lengths, with two different measurements for each length. The curves were smoothed and offset for clarity. At $B_\parallel = 0$, two subbands are occupied. Above 3.5 T the upper subband is emptied due to a diamagnetic shift. UCF can still be observed. The inset explains how electrons can move along the z-direction for one occupied subband and high magnetic fields.

In Fig. 5.8b, we plotted the differential magnetoresistance for $U_{\mathrm{fg}} = -295\,\mathrm{mV}$. Quasi-periods of about 1 T are recognizable, which is by a factor of about 30 larger than in perpendicular fields[2] and agrees with our expectations.

5.4 Conclusions

We have investigated the WL and UCF effects in an electron gas at the crossover from two to three dimensions. For a strictly 2D system ($n_{\mathrm{H}} = 1.2 \cdot 10^{15}\mathrm{m}^{-2}$), we have found from the WL correction $\tau_\phi = 14\,\mathrm{ps}$ ($\tau_{\mathrm{el}} = 2.6\,\mathrm{ps}$), corresponding to $l_\phi = 0.64\,\mu\mathrm{m}$ ($l_{el} = 0.39\,\mu\mathrm{m}$). At the crossover to three dimensions the length scales l_ϕ, l_{el} and W are not well separated and no theory exists to relate the resistivity corrections to the phase-coherence length l_ϕ. We therefore have described the measured characteristics of the resistivity corrections. Both the height $\Delta\sigma_0$ and width ΔB of the WL peaks increase with n_{H} until a second subband starts to get populated, where both quantities decrease with n_{H}.

From the UCF amplitudes and quasi-periods, we calculated the values $C_1 l_\phi$ and $C_2 l_\phi$ defined in Eqs. 5.4 and 5.5. Both quantities generally increase with n_{H}. At the occupation threshold of the second subband, the increase of $C_i l_\phi$ is retardet but catches up at higher densities. The occupation of the second subband therefore manifests itself in both of the investigated quantum-interference phenomena.

---

[2] A quasi period is about 6 times larger than ΔB_c. The quasi-periods in the perpendicular case are about 30 mT.

Chapter 6

Subband Densities and in-Plane Magnetic Field

We learned how electrons in a 2DEG behave if they are exposed to a perpendicular magnetic field. SdH-oscillations in the magnetoresistivity allowed us to determine the electron densities of different subbands and draw conclusions on the energy structure (chapter 2.5.2). Here, we look into what happens if the magnetic field is applied parallel to the 2DEG. There are two principal effects arising from such an in-plane field:

- The subband energy levels are diamagnetically shifted. The shift is proportional to the extension of the wave functions and results from the additional magnetic confinement $m^*\omega_c^2 z^2/2$ along the z-direction.
- The dispersion relation is modified in the in-plane direction. This leads to a distortion of the Fermi surfaces and consequently to a modified DOS. For multi-subband systems, the Fermi surfaces of the individual subbands may even separate in k-space, leading to anomalies in transport quantities [108].

Both effects – diamagnetic shift and Fermi-surface distortion – lead to a carrier redistribution among the subbands. If a perpendicular B-component is applied in addition, the SdH-oscillations give a measure for the subband densities n_i. This way we have investigated the dependence of n_i on a weak in-plane magnetic field as a function of the tunable shape of the well potential. We have measured a strong carrier redistribution between the subbands, which cannot be explained by the diamagnetic energy shift alone. We give an explanation based on individual magnetic-field dependent density of states in different subbands. The measured carrier redistribution is quantitatively reproduced by a calculation of the energy structure considering the in-plane field in second-order perturbation theory. The results presented in this chapter have been published in Ref. [109]. The data has been obtained for the diploma thesis of Beat Ruhstaller [110]. Some measurements have been repeated in semester works done by L. Roschier and M. Huberty.

6.1 Introduction

An electron system confined in one spatial dimension with an additional magnetic field is a textbook example that allows to study the behavior of quantum mechanical energy levels and wave functions in detail. If the magnetic field is oriented perpendicular to the plane of the electron system, the Hamiltonian can be separated with respect to the in-plane and perpendicular motion. Therefore the Landau quantum numbers and subband quantum numbers are independent of each other and level degeneracies occur at certain magnetic fields [40]. In the case of a parabolic confining potential, the Hamiltonian can be solved analytically for any orientation of the magnetic field [111, 112]. For arbitrary confining potentials one relies on perturbative approaches. A lot of theoretical [113 - 122]. as well as experimental work has been done in this field [123 - 125, 108]. Here, we focus on the importance of second order perturbation theory for a small – but arbitrarily oriented – magnetic field. In particular, we find a strong redistribution of the subband electron densities due to an in-plane magnetic field, which we quantitatively explain by a subband-dependent density of states.

In a PQW with plasma frequency Ω, the in-plane field has two effects: The energy levels are diamagnetically shifted proportional to $(1+\omega_c^2/\Omega^2)^{(1/2)}$, and the dispersion relation of the in-plane electron motion is modified, which can be described by a magnetic-field dependent effective mass [114, 121, 125]. For a PQW, the effective mass is $m^*(1+\omega_c^2/\Omega^2)^{(1/2)}$. Thus the two-dimensional density of states (DOS) depends on the in-plane magnetic field.

Experimentally, the electron densities n_i of the subbands i in the presence of an in-plane magnetic field $B_{||}$ can be determined by analyzing Shubnikov-de Haas (SdH) oscillations in a transport measurement. In the case of one occupied subband, the diamagnetic shift of the subband energy has no influence on the measured subband density. However, the modified effective mass can be determined by measuring the temperature dependence of the SdH-oscillations[126, 127] or by optical experiments[125]. Only if more than one subband is populated, the diamagnetic energy shift may lead to a redistribution of subband densities. The parallel-field dependence of n_i has been measured for heterojunctions [124] and for parabolic quantum wells[127]. In Ref. [127], measurements of a PQW were compared with the analytical solution of the parabolic confining potential, although the effective potential is closer to a rectangular well. In order to relate the measured $n_i(B_{||})$ to the diamagnetic energy shift, a perturbative expression for the diamagnetic shift was considered in Ref. [123] and [124]. However, the varying DOS was not taken into account. As was pointed out by Ref. [118], the varying DOS can have a significant effect on the depopulation of the upper subband.

In this chapter, we present measurements confirming that the influence of the $B_{||}$-dependent DOS on the measured subband densities is dominant over the diamagnetic shift in the considered PQWs. We have measured $B_{||}$-dependencies of subband densities in a wide PQW with tunable electron sheet density and potential symmetry. The effect of these parameters on n_i is studied for small $B_{||}$. The data is compared to a perturbative calculation of the energies to second order, using self-consistently

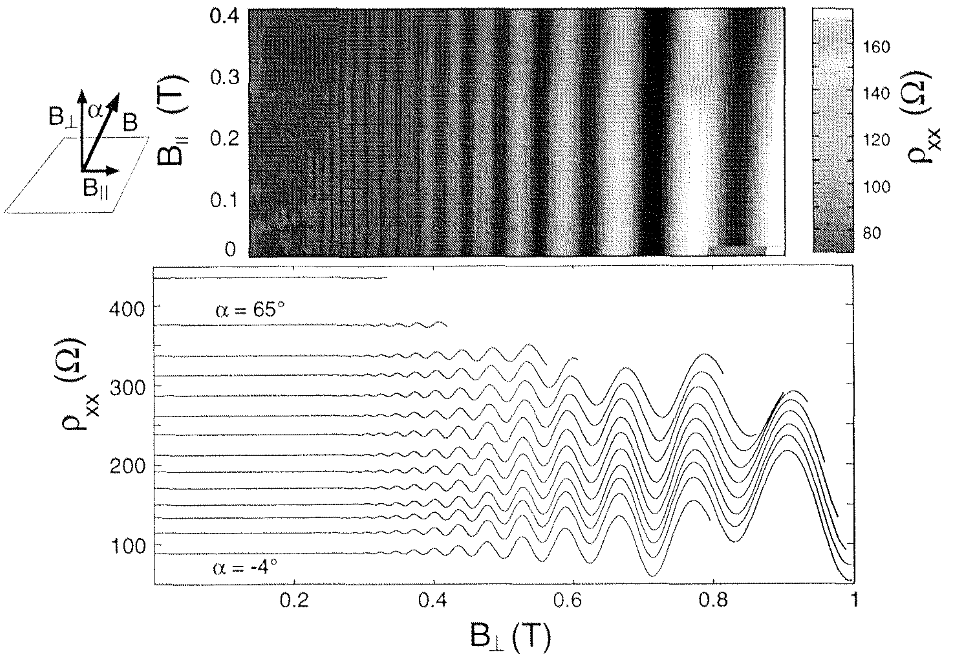

Figure 6.1: Measured magnetoresistances ρ_{xx} as a function of the perpendicular field $B_\perp$ for different tilt angles α between -4° and 65°. The ρ_{xx}-values are offset for clarity. The upper part of the figure shows a contour plot of the same data as a function of $B_{||}$ and $B_\perp$. Darker regions correspond to smaller ρ_{xx} (the grey scale is indicated on the right side). A small deviation of the minimum position to higher $B_\perp$ is observed with increasing $B_{||}$.

calculated wave-functions at $B = 0$ as a basis. The first-order term determines the diamagnetic shift, whereas distortions of the Fermi sphere are due to the second-order term. As we will show, the latter effect on n_i is of the same order of magnitude as the diamagnetic shift. It may even dominate the $B_{||}$-dependence of n_i in the case when the DOS in the individual subbands differ. By applying a front-gate bias, we experimentally control the difference between the subband-dependent DOS and study its influence on the measured subband densities.

6.2 Experiment

In order to increase the asymmetry induced by the front-gate bias, the measurements were taken on sample no 18 with a 3 monolayer thick $\mathrm{Al}_{0.15}$ $\mathrm{Ga}_{0.85}$As-spike situated in the center of the well.

The sample was mounted on a revolving stage. Measurements were performed at 1.7 K. The tilt angle α between the sample normal and the direction of the magnetic field was determined by scaling both the Hall resistance ρ_{xy} and the Shubnikov-de Haas (SdH)-minima in the magnetoresistance ρ_{xx} to $\cos\alpha$ (with the sample being in the single-subband regime). We estimate the accuracy of the obtained angle α to be better than 0.2 degrees.

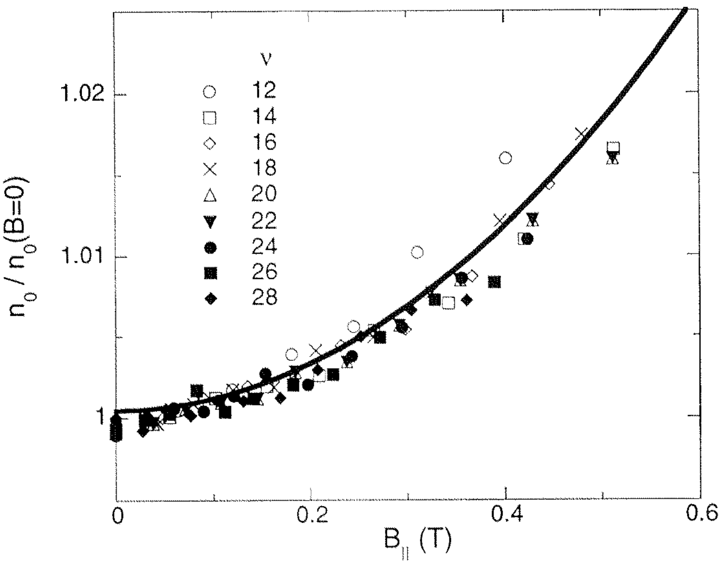

Figure 6.2: Density of the lowest subband n_0 normalized to the density $n_0(B_{||} = 0)$ as a function of the in-plane field, as obtained from measurements presented in Fig. 6.1. For the determination of n_0, filling factors of the E_0-subband between 12 and 28 and tilt angles between -4° and 65° have been evaluated.

In the case of two occupied subbands E_0 and E_1 (densities n_0 and n_1), the SdH-minima do not scale with $\cos\alpha$ anymore. In a weak perpendicular field $B_\perp$, ρ_{xx} is periodic in $1/B_\perp$ with a frequency proportional to n_0. The oscillation due to the E_1-subband is weak and not observed for low densities n_1 (Fig. 6.1). If the sample is tilted by an angle α, the degeneracy of each Landau level is still determined by $B_\perp$. Analyzing the $B_\perp$- positions of even filling factors allows one to determine n_0 in tilted fields.

Figure 6.1 shows measured traces of ρ_{xx} plotted as a function of the perpendicular magnetic field $B_\perp = B\cos\alpha$ with the tilt angle α as a parameter. As there is no spin-splitting observed at low magnetic fields, each minimum in $\rho_{xx}(B_{||})$ corresponds to an even E_0-subband filling factor ν_0, which is deduced from the ρ_{xx}-trace at $\alpha = 0$. The subband density $n_0 = e\nu_0 B_\perp/h$ is determined by the $B_\perp$-position of such a minimum. In Fig. 6.2, we present n_0 as a function of the in-plane field $B_{||}$ by using $B_{||} = B_\perp \tan\alpha$. Several filling factors ν_0 between 12 and 28 and tilt angles α between -4° and 65° have been evaluated. In the case of two occupied subbands, n_0 generally increases with $B_{||}$, corresponding to a depletion of the upper subband[124, 128]. We limit the discussion to small magnetic fields $B_{||}, B_\perp < 1\,\mathrm{T}$. To first order, the increase of n_0 is quadratic in $B_{||}$. We therefore introduce the coefficient

$$\gamma = dn_0/dB_{||}^2, \tag{6.1}$$

which we determine from a parabolic fit to the measured data.

Although we are interested only in the small-B behavior here, the subband densities can also be measured for higher $B_{||}$. Above some field B_d, all electrons from the upper

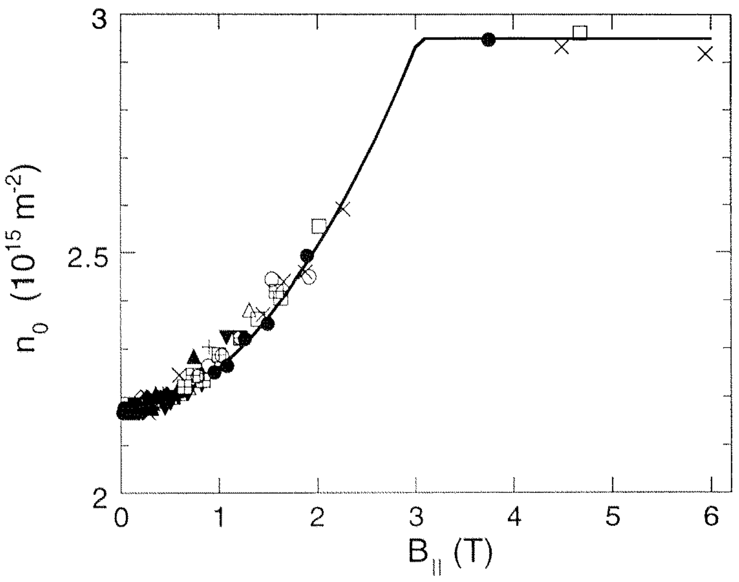

Figure 6.3: Measured n_0 vs $B_{||}$ for a sample with $x = 0.05$, $U_{\mathrm{bg}} = 0\,\mathrm{mV}$ and $U_{\mathrm{fg}} = -150\,\mathrm{mV}$ (corresponding subband densities of $n_1 = 2.15 \cdot 10^15\,\mathrm{m}^{-2}$ and $n_2 = 0.8 \cdot 10^15\,\mathrm{m}^{-2}$.

subband have settled in the lower subband, the density of which then remains constant (and equal to the total sheet density n_{H}). Fig. 6.3 shows such a measurement. The data has been fitted by a parabola for $B_{||} < 2.5\,\mathrm{T}$. This is motivated by the analytical solution for a parabolic confinement [111, 112]. From the fit, a depletion field of 2.3 T is determined. We refer to the depletion field in the discussion of universal conductance fluctuation in an in-plane magnetic field (chapter 5.3).

The variation of γ (Eq. 6.1) with the total density and the symmetry of the well is of interest here. For this purpose, measurements as presented in Fig. 6.2 were performed for different front-gate biases U_{fg}. The total sheet density n_{H} increases with U_{fg} and the electron distribution moves closer to the sample surface. Figure 6.5 presents the measured γ, plotted as a function of n_{H}. Note that the potential symmetry also changes with n_{H}, due to the inserted potential spike and the boundaries of the well. Up to densities around $n_{\mathrm{S}} = 3.0 \cdot 10^{15}\,\mathrm{m}^{-2}$, γ increases and reaches a maximum value of $1.7 \cdot 10^{14}\,\mathrm{m}^{-2}\mathrm{T}^{-2}$.

In the following section, we compare the data to a perturbative calculation of the diamagnetic shift and the DOS, and to the analytical solution for a parabolic confining potential. Only if the $B_{||}$-dependence of the DOS – obtained by the second-order term of the perturbation calculation – is included, the calculation can account for the measured γ.

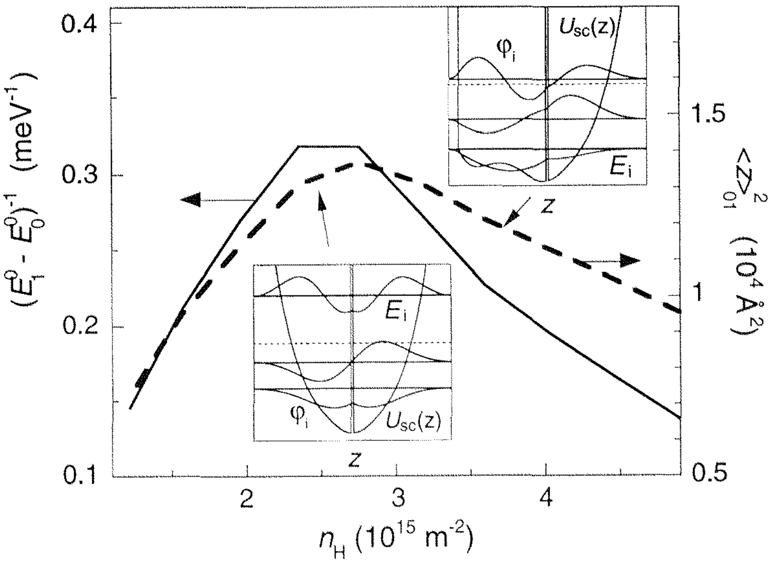

Figure 6.4: Calculated values for $(E_1^0 - E_0^0)^{-1}$ and $\langle z \rangle_{10}^2$ for different sheet densities n_H. The dominating contribution to γ originating from the second-order term is proportional to $\langle z \rangle_{10}^2/(E_1^0 - E_0^0)$. The insets show at two different n_H the self consistent potential U_sc, the wave functions φ_i^0 and the energy levels E_i^0 for subbands $i = 0, 1, 2$. The Fermi energy is indicated as a dashed line.

6.3 Comparison with theory

6.3.1 First order perturbation theory

In the following we calculate the energy spectrum of a two-dimensional electron system subjected to an in-plane field $B_\|$. The perpendicular field does not have to be included in the calculation, as we use small fields, where the Landau-ladder is smoothed out to an approximately constant DOS. A perturbative calculation of the effective cyclotron mass m^* in tilted fields is presented in Ref. [125], where the $B_\|$-dependence of m^* originates from a shift in Landau-level separation due to the coupling Hamiltonian. The effective mass obtained from the Landau-level spacing is equivalent to that considering the dispersion modification due to an in-plane field.

With the magnetic field $B_\|$ along the x-direction described by $\mathbf{A} = (0, -B_\| z, 0)$, the momentum operator p_z in z-direction, the elementary charge e and electron effective mass m^*, the Hamiltonian of non-interacting electrons mobile in the x-y plane and confined in the z-direction by a potential $U(z)$ takes the form

$$H = \underbrace{\frac{p_z^2}{2m^*} + U(z)}_{H_0} + \frac{\hbar^2 k_x^2}{2m^*} + \frac{\hbar^2 k_y^2}{2m^*} + \underbrace{\frac{e^2 B_\|^2}{2m^*} z^2 + \frac{e B_\| \hbar k_y}{m^*} z}_{H'} . \tag{6.2}$$

The wave function is separated into plane waves along the x- and y-direction (wave numbers k_x and k_y) and the solution $\phi_i(z, k_y)$ to $H_0 + H'$ with energy $E_i(k_y)$. The total energy is given by $E_i(k_x, k_y) = E_i(k_y) + \hbar^2(k_x^2 + k_y^2)/2m^*$. Non-degenerate perturbation theory is applied to the eigenstates of H_0 with energies E_i^0 and wave functions φ_i^0, treating H' as being a small perturbation (small in-plane fields $B_\|$). The first-order correction to the energy results in

$$\begin{aligned} E_i(k_x,k_y) \quad &\approx \quad E_i^0 + \frac{\hbar^2 k_x^2}{2m^*} + \frac{\hbar^2 (k_y - k_0)^2}{2m^*} \\ &\quad + \frac{e^2 B_\|^2}{2m^*}(\langle z^2\rangle_{ii} - \langle z\rangle_{ii}^2), \end{aligned} \tag{6.3}$$

where $\langle\ldots\rangle_{ij}$ denotes the matrix elements corresponding to the wave functions ϕ_i^0 and ϕ_j^0, respectively, and $k_0 = eB_\|\langle z\rangle_{ii}/\hbar$. The diamagnetic shift in energy [113] is quadratic in $B_\|$ and proportional to $\langle z^2\rangle - \langle z\rangle^2$. The magnitude of the shift increases with subband number i due to the increasing spatial extent of higher subband wave functions. Additionally, the Fermi surface is displaced in x-direction by k_0. This displacement has no influence on the DOS and the effective mass m^*. We now calculate the magnetic-field dependence of the subband density $n_0 = m^*/\pi\hbar^2(E_\mathrm{F} - E_0)$, which is given by the $B_\|$-dependence of E_0 and E_F. The Fermi energy E_F depends on $B_\|$ due to the rearrangement of subband densities. In the following, we assume that two subbands E_0 and E_1 are occupied ($E_\mathrm{F} > E_0, E_1$). With $\Delta n = n_0 - n_1|_{B_\|=0}$, we obtain for $\gamma = dn_0/dB_\|^2$

$$\gamma = \Delta n \cdot \frac{\delta}{2} \tag{6.4}$$

with

$$\delta = \frac{e^2}{2m^*}\frac{\langle z^2 - \langle z\rangle^2\rangle_{11} - \langle z^2 - \langle z\rangle^2\rangle_{00}}{E_1^0 - E_0^0}. \tag{6.5}$$

By solving the Poisson- and Schrödinger equations for our PQW self-consistently, we find the wave functions φ_i^0 and energies E_i^0 for different gate biases. The consistency of these values can be checked by comparing the obtained E_i^0 with the measured subband densities n_i at zero in-plane field, divided by the DOS[40]. If the calculated φ_i^0 and E_i^0 are inserted into Eq. (6.4), one obtains values for γ which are up to 7 times smaller than the measured ones (Fig. 6.5).

6.3.2 Second-order term and subband-dependent DOS

In order to calculate the modification of the effective mass, we have to take into account second-order perturbation theory. The linear term in k_y (Eq. 6.2) becomes quadratic in the second-order perturbation, which modifies the dispersion along this direction. Neglecting powers of $B_\|$ larger than two, and considering only contributions to the perturbation sum from neighboring subbands, leads to the following corrections to $E_i(k_x,k_y)$:

$$E_i''(k_y) = -\frac{\hbar^2 k_y^2}{m^*}\beta_i B_\|^2 \tag{6.6}$$

with

$$\beta_0 = \frac{e^2}{m^*}\frac{\langle z\rangle_{10}^2}{E_1^0 - E_0^0}$$

$$\beta_1 = \frac{e^2}{m^*} \frac{\langle z \rangle_{21}^2}{E_2^0 - E_1^0} - \beta_0. \tag{6.7}$$

This second-order term leads to a modified dispersion relation in y-direction $\hbar^2 k_y^2 / 2m_y^*$ with $m_y^* = m^*/(1 - 2\beta_i B_\parallel^2)$, whereas the x-direction parallel to $B_\parallel$ remains unaffected. The Fermi disc is distorted to an ellipse. This can be accounted for by a modified, subband-dependent effective mass[114, 118]

$$m_i^* = \sqrt{m_x^* m_y^*} \approx m^*(1 + \beta_i B_\parallel^2). \tag{6.8}$$

Therefore the DOS ρ_i depends on $B_\parallel$, and on the subband index i:

$$\rho_i = \rho(1 + \beta_i B_\parallel^2). \tag{6.9}$$

In the equations above we assumed that $\beta_i B_\parallel^2 \ll 1$, which is a prerequisite for the applicability of perturbation theory. The parameter β is proportional to the ratio of the Landau energy $\hbar e B_\parallel / m^*$ to the subband energy difference, as well as on $\langle z \rangle_{10}^2 / l_{B_\parallel}^2$, with the squared magnetic length $l_{B_\parallel}^2 = \hbar / e B_\parallel$. Thus both, the Landau energy compared to the subband difference, and the off-diagonal z-matrix element compared to the magnetic length, have to be small for the applicability of perturbation theory. In the approximation used here, the subband-dependent correction to the DOS varies quadratically with the in-plane field. In the description of the subband density, we therefore have to be careful in converting the energy levels to subband densities. The subband densities are written as $n_i = \rho_i(E_F - E_i)$. With $n_\mathrm{H} = n_0 + n_1$ we obtain for γ:

$$\gamma = \Delta n \left(\frac{\delta}{2} + \frac{\beta_0 + \beta_1}{4} \right) + n_\mathrm{H} \frac{\beta_0 - \beta_1}{4}. \tag{6.10}$$

In the first term we recognize the first-order result of Eq. (6.4), with δ replaced by $\delta + (\beta_0 + \beta_1)/2$. As we will show in the next section, this corresponds to a doubled value in the case of a parabolic confining potential. Because of the increase in DOS with $B_\parallel^2$, the lower subband accommodates more carriers, which gives rise to an increase in n_0 of the same order as from the diamagnetic shift itself.

The second term being proportional to the sheet density n_H and the difference of the DOS-parts β_0 and β_1 cancels out in an exact parabolic potential. For arbitrary potentials, the $B_\parallel$-dependence of the DOS can be quite different for the two subbands, leading to an additional redistribution of the carrier densities between the two subbands. The influence of this term on $n_0(B_\parallel)$ can even dominate.

If we insert the calculated ϕ_i^0 and E_i^0 into Eq. (6.7) and (6.10), we in fact observe strongly different β_i and the second term of Eq. (6.10) dominates the resulting γ (Fig. 6.5). In contrast to the first-order result, this calculation is in good agreement with the experimental values, and perfectly reproduces the maximum around $n_\mathrm{S} = 3.0 \cdot 10^{15}\,\mathrm{m}^{-2}$. For small enough magnetic fields, higher orders in the perturbation series are small corrections to the DOS enhancement and to the diamagnetic shift.

6.3.3 Exact solution for a parabolic potential

In the exact solution for a parabolic quantum well with potential $U(z) = m^* \Omega^2 z^2 / 2$, the subband energy levels for an in-plane field $B_\parallel$ are given by [111, 112] $E_n =$

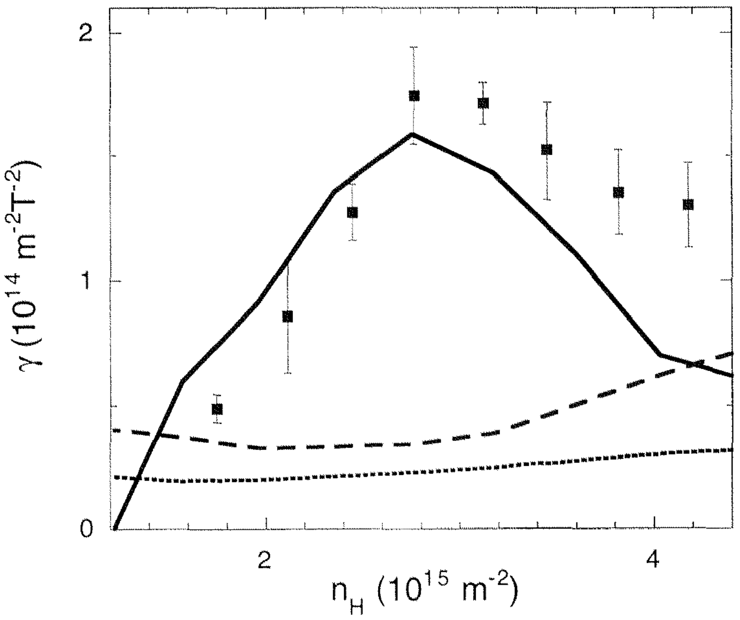

Figure 6.5: Measured $\gamma = dn_0/dB_{\|}^2$ as a function of n_{H} (symbols). Note that n_{H} was varied by applying a front-gate bias, and thus also the symmetry with respect to the potential spike changed with increasing n_{H}. The error bars indicate deviations in γ originating from evaluation with different filling factors. The dotted line corresponds to first-order perturbation theory (Eq. 6.4), the solid line indicates the full second-order calculation, the dashed line is the first term $\Delta n(\delta/2 + (\beta_0 + \beta_1)/4)$, which neglects subband-dependent DOS.

$\hbar(\omega_c^2 + \Omega^2)^{\frac{1}{2}}(n + 1/2)$. The DOS is independent of the subband number and is found to be

$$\rho(B_{\|}) = \rho\left(1 + \frac{\omega_c^2}{\Omega^2}\right)^{1/2}. \qquad (6.11)$$

Thus one obtains for γ

$$\gamma = \rho\hbar\Omega\frac{e^2}{2m^{*2}\Omega^2} \qquad (6.12)$$

Considering that $\langle z\rangle_{10}^2 = \hbar/2m^*\Omega$, $\langle z\rangle_{21}^2 = \hbar/m^*\Omega$ and $\langle z^2\rangle_{11} - \langle z^2\rangle_{00} = \hbar/m^*\Omega$, we exactly recover the result of Eq. (6.7) and (6.9). It is worth noting that in the case of a parabolic potential, perturbation theory up to order $B_{\|}^2$ gives the exact result. Considering Eq. (6.10), we find that $(\beta_0 + \beta_1)/2 = \delta$, and $\beta_0 - \beta_1 = 0$. Thus the second-order result is exactly twice the first-order result of Eq. (6.4), and the term proportional to n_{H} in Eq. (6.10) vanishes.

6.4 Discussion and Conclusions

The data presented in Fig. 6.5 provides evidence that the $B_{\|}$-driven carrier redistribution among the two subbands is dominated by the $B_{\|}$ dependent DOS. We observe a maximum in $\gamma(n_{\mathrm{H}})$ which is due to a subband specific DOS, described by the term in Eq. (6.10) containing $\beta_0 - \beta_1$. Using Eq. (6.7) one finds that

$$\beta_0 + \beta_1 \propto \frac{\langle z \rangle_{21}^2}{E_2^0 - E_1^0}, \tag{6.13}$$

and

$$\beta_0 - \beta_1 \propto \frac{2\langle z \rangle_{10}^2}{E_1^0 - E_0^0} - \frac{\langle z \rangle_{21}^2}{E_2^0 - E_1^0}. \tag{6.14}$$

As an illustration, we consider the calculated wave functions and energy levels for our samples. Since the most important contribution to the carrier redistribution is the $\beta_0 - \beta_1$ term, we present $(E_1^0 - E_0^0)^{-1}$ and $\langle z \rangle_{10}^2$ in Fig. 6.4, plotted as a function of $n_{\rm H}$. Both functions clearly show a maximum at approximately the same position. There, the self-consistently calculated wave functions are centered with respect to the spike. In this situation, the two occupied subbands are symmetric and asymmetric states, with minimum energy difference $E_1^0 - E_0^0$. At the same time, the matrix element $\langle z \rangle_{10}^2$ is maximal. Generally, the inverse energy difference and the squared off-diagonal matrix element respond similarly to a changing external parameter.

We expect a less pronounced maximum for weaker potential spikes. This is confirmed in a measurement on a similar sample (no. 17) with a potential spike described by its Al content $x = 0.05$, where we find a monotonic increase of $\gamma(n_{\rm H})$ (Fig. 6.6). We want to emphasize that even without a potential spike, the subband carrier redistribution is strongly influenced by the DOS contribution proportional to $\beta_0 - \beta_1$.

For arbitrary confining potentials, one has to compare relevant matrix elements and energy differences. In Table 6.1, we present the calculated values for a heterostructure[1], a parabolic potential, a PQW with and without spike, and a double quantum well (DQW)[2]. In order to clarify the relative importance of the diamagnetic shift and the DOS, we split γ from Eq. (6.10) into the two contributions $\gamma_{\rm dia} = \Delta n \delta/2$ and $\gamma_{\rm DOS} = \Delta n(\beta_0 + \beta_1)/4 + n_{\rm H}(\beta_0 - \beta_1)/4$. The weaker the tunneling coupling between the left and the right side of the well, the more important the $\beta_0 - \beta_1$ term becomes. In addition, this term has to be weighted by the total carrier density $n_{\rm H}$ rather than by the subband density difference. In a heterostructure, $\beta_0 - \beta_1$ is negative, which weakens $\gamma_{\rm DOS}$, such that $\gamma_{\rm dia}$ determines the carrier redistribution. The large $\gamma_{\rm DOS}$ for DQW structures is a result of the well-known effective mass change for peanut- and lense-shaped Fermi contours [108].

In conclusion, we have described the $B_{||}$-dependence of the subband density n_0 by an analytical expression, derived from second-order perturbation theory. The comparison with measurements on PQWs gives good agreement for $B_{||} < 1\,{\rm T}$. In contrast to earlier publications [123, 124], our results are not dominated by the diamagnetic shift, but by the influence of $B_{||}$ on the DOS of the two subbands which leads to a redistribution of the carrier densities among the subbands. This explanation was confirmed in measurements where the shape of the confining potential could be controlled.

It should be worthwhile to check this effect by cyclotron resonance experiments, where we expect a pronounced splitting of the absorption because the effective masses in this two-subband system display a different $B_{||}$-dispersion.

---

[1] spacer layer 100 Å, residual acceptor concentration $2.7 \cdot 10^{20}\,{\rm m}^{-3}$, donor layer $6.5 \cdot 10^{15}\,{\rm m}^{-2}$

[2] well width 140 Å, barrier 28 Å as in Ref.[108]

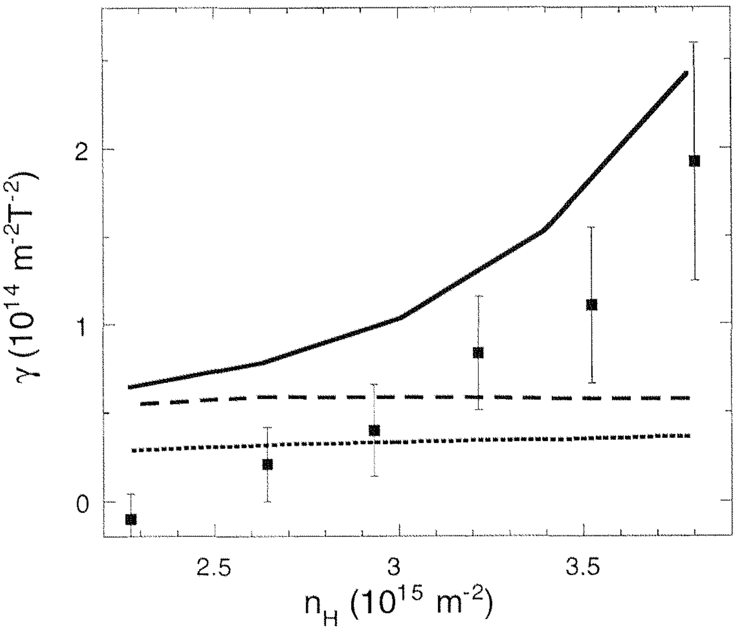

Figure 6.6: Measured values of γ (symbols) for different n_H compared to results from second-order perturbation theory (line) for a sample with a weak potential spike (Al-content x=0.05, width 8.5 Å) centered in the potential well. The error bars correspond to evaluations at different filling factors. The dotted line describes the diamagnetic shift only, the dashed line includes the $\beta_0 + \beta_1$ term.

Table 6.1: Calculated coefficients δ, β_0 and β_1 (in T^{-2}); n_H and $n_0 - n_1$ (in $10^{15}\,\mathrm{m}^{-2}$), and carrier redistribution coefficients γ (in $10^{14}\mathrm{m}^{-2}\mathrm{T}^{-2}$) for a heterostructure, a parabolic potential, a PQW without and with spike as measured, and a double quantum well (DQW). γ is split into the diamagnetic shift part γ_dia (containing δ) and the DOS-part γ_DOS (containing β_0 and β_1). In the DQW and PQW the wave functions are centered in the well.

sample	2δ	$\beta_0 + \beta_1$	$\beta_0 - \beta_1$	n_H	$n_0 - n_1$	γ_dia	γ_DOS
heterostructure	0.013	0.032	-0.027	4.9	4.6	0.15	0.04
parabolic potential	0.024	0.024	0	3.2-9.6	3.2	0.19	0.19
PQW	0.104	0.080	0.058	2.8	1.3	0.34	0.67
PQW+spike	0.128	0.045	0.181	2.8	0.9	0.29	1.37
DQW	0.011	0.001	0.311	5.2	0.4	0.01	4.04

Chapter 7

Ballistic One-Dimensional Systems

An electron system is in the ballistic regime, when its size is smaller than the elastic mean free path l_{el}. The high mobility of 2DEGs allows for ballistic electron transport over several tens of micrometers in AlGaAs heterostructures. Modern lithographic techniques enables to confine a 2DEG into wires and dots with sizes comparable to the electron Fermi wavelength. In such systems quantum-mechanical effects manifest themselves strongly, for example:

- A quantum point contact (QPC) is a 1D system, where a 2DEG is confined laterally by a constriction of a width comparable to the Fermi wavelength [129]. The conductance is quantized in units of $2e^2/h$, which was first observed in 1988 [130, 131] and is attributed to the formation of 1D-subbands (also called modes or quantum channels), each carrying the same current.

- In quantum dots the energy spectrum consists of 0D states [132]. Each state can be occupied by two electrons. The vertical confinement is usually much stronger than the lateral one. Hence only one vertical quantum state is occupied, and the energy spectrum is determined by the lateral confinement. Electron-electron interaction is important and leads to charging effects as the number of electrons is changed, and also to level anticrossing, i.e., the approach and subsequent repulsion of two energy levels instead of a crossing, which can be understood by considering Coulomb-interaction in a Hartree approximation.

Special attention has been paid to the Darwin-Fock [133, 134]-like energy structure of lithographically patterned quantum dots [135, 136] and of self-assembled quantum dots [137] in a perpendicular magnetic field. The energy structure of a quantum dot is related to that of the modes that pass through a QPC. In both systems, the lateral confinement determines the energy spectrum. The electrons in a quantum dot occupy 0D states. Their energies can be probed by tunneling through barriers into the confined region. In a QPC, one direction is not confined, such that a current can flow through a constriction. As we will demonstrate, spectroscopy of single-particle energy levels in the absence of charging effects is possible.

In a conventional QPC, the 2DEG at the GaAs/AlGaAs heterointerface is confined in one lateral direction by a split-gate electrode on top of the sample surface. The constriction is thin in growth direction and wide in the split-gate direction. Only the ground state in growth direction is occupied, and the constriction is more similar to a slit than to a disk.

A QPC where the constriction is wide in both dimensions is called a 3D QPC [138], see Fig. 7.1a. The fabrication of a circular opening is difficult to achieve. It can be realized in metalls by bringing a tip into proximity with a metallic surface and subsequently retracting the tip, such that a stretched, narrow connective wire results.

Here we present the realization of 3D QPCs with a tunable constriction shape. It is controllably fabricated by lithographically defining a split-gate electrode on top of a 2DEG confined in a PQW. The confinements in the two directions are of similar magnitude and are controlled by the split-gate electrode, and by the back gate controlling the PQW potential, respectively (Fig. 7.1b).

The Fermi energy is adjusted by the voltage U_{sg} applied between the split gate and the 2DEG. By measuring the conductance $G(U_{\mathrm{sg}})$ of the QPC, spectroscopy of the magneto-electric 1D subbands has been realized. We have mapped out the relative positions and degeneracies of the subband energies and investigated their behavior when a magnetic field is applied. The obtained single-particle spectrum resembles the Darwin-Fock states of a quantum dot. Due to the non-circular shape of the confining constriction, the energy spectrum of a system with broken rotational symmetry can be studied, in contrast to the states of a symmetric quantum dot, which are degenerate at $B = 0$.

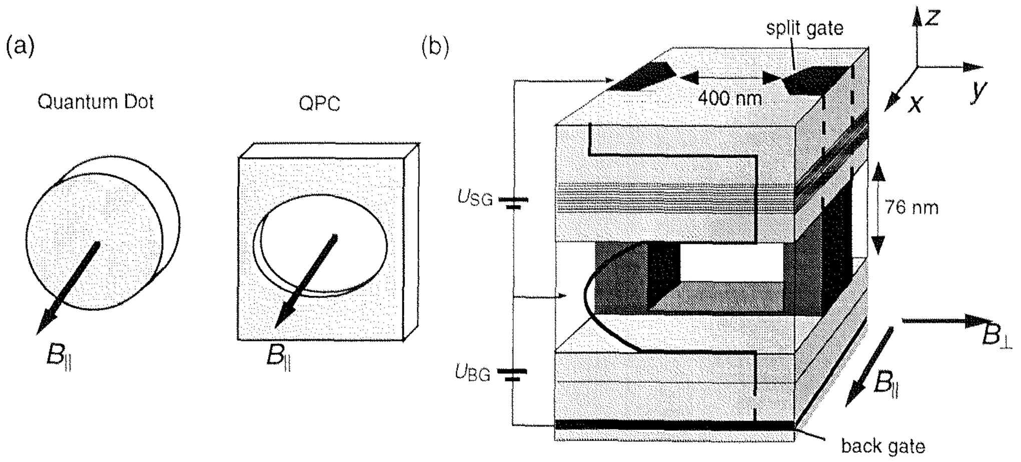

Figure 7.1: (a) Quantum dot and 3D quantum point contact in a magnetic field. (b) Realization of a 3D QPC using a PQW as a host structure.

The interaction between different channels is of special interest. With no interaction, the energy levels simply cross as a function of some controlling parameter (as the back-gate voltage). A coupling of the two confinement directions leads to the anti-crossings of levels. However, 1D subband-level "lockings" were predicted as well [139]. Although we cannot exclude level locking, no clear indication for such behavior has been found experimentally. The results presented in this chapter have been published in Refs. [140, 78].

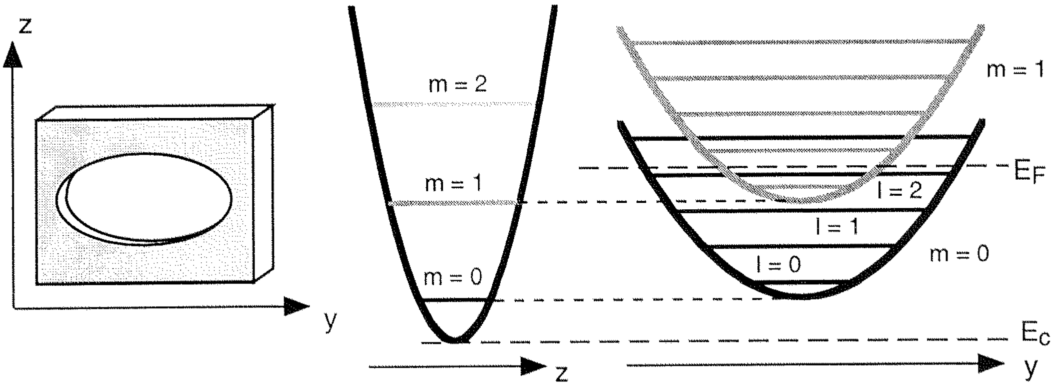

Figure 7.2: Two quantum numbers m and l describe the electron states quantized in y-direction (l) and z-direction (m). For each m, a ladder forms whose steps are labeled by l.

7.1 Introduction

The energy structure of a parabolically confined 3D QPC has been calculated in Ref. [138]. Here, transversal modes in both lateral directions are important. Whereas the 1D channels in a conventional QPC are described by one quantum number l, in a 3D QPC channels from both confinement directions (labeled as y- and z-direction in Fig. 7.1b) can be occupied. The channels are labeled by l (y-direction) and m (z-direction). One can think of several 1D-subband ladders m, the steps of which are labeled by l (Fig. 7.2). This assumption is valid if the Hamiltonian can be separated for the y- and z-directions. Level degeneracies can occur because of the two quantum numbers (l,m).

The conductance through a QPC is quantized in integer multiples N of $2e^2/h$ [131, 130], where N corresponds to the number of occupied, spin-degenerate channels. This quantization results from a cancellation of the energy dependence in the product of velocity and DOS in a 1D system [34]. The total number N of ladder steps below the Fermi level is given by $N = \sum_{m=0}^{M} l_m$ if a total of $M - 1$ ladders are occupied and l_m denotes the occupied channels of the m-th ladder. The 3D QPC can be imagined as M separate – but coupled – QPCs. In this respect, the system is similar to spatially separated QPCs arranged in parallel, as realized laterally with a double split gate [141, 142] and vertically by a split gate on top of a double quantum well structure[143], where transport characteristics have revealed no interaction between the one-dimensional subbands.

Each time when the Fermi energy passes through a 1D subband energy, the conductance changes by $2e^2/h$. This enables us to measure the subband energy spectrum with respect to the Fermi energy. If the Fermi energy passes the energy level of two degenerate channels, the conductance changes by $4e^2/h$, i.e., one conductance plateau is missing.

We list the possible modifications of the 3D QPC shape and its energy spectrum:

- The **split-gate voltage** U_{sg} changes the Fermi energy relative to the 1D subbands as well as the constriction width in y-direction.

- The **back-gate voltage** $U_{\rm bg}$ modifies the constriction in z-direction. For increasing $U_{\rm bg}$, the density in the confinement increases and the width of the screened parabolic potential widens.
- A **magnetic field** influences the energy spectrum of the magneto-electric 1D subbands. The modification depends on the field orientation.

We investigate magnetic field directions parallel and perpendicular to the channel (but always parallel to the 2DEG). While a perpendicular magnetic field $B_\perp$ only shifts the energy position of the modes and thus varies N, a parallel field $B_\|$ induces coupling between certain classes of modes, which leads to level anticrossing as a function of the field. We will describe the influence of the magnetic field on the energy of the modes in a simple picture and model the origin of the mode coupling.

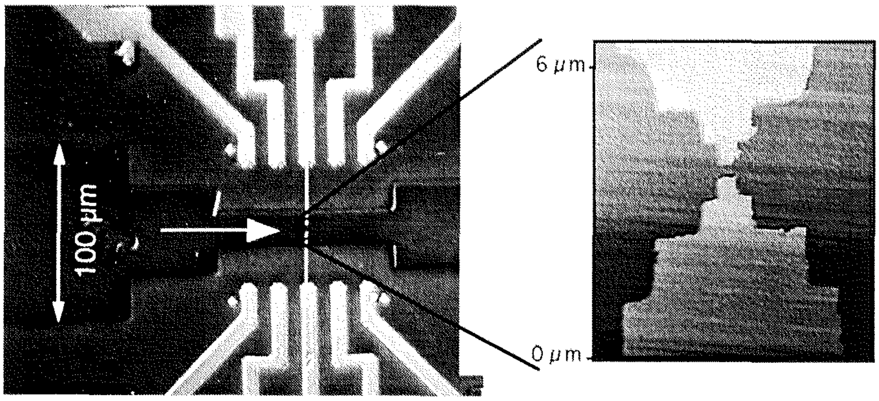

Figure 7.3: Photograph of mesa structure (left) and AFM image of the split gate defining the QPC (right).

7.2 Experiment

The host structure for the electron gas is a 760 Å wide PQW with a weak, 3 monolayer thick $Al_{0.05}Ga_{0.95}As$ potential spike in the center. A back gate electrode is located 1.35 μm below the well. On the top of the structure, a 400 nm wide split gate electrode was defined by standard electron beam lithography and evaporation of 30 nm TiAu (Fig. 7.3). A voltage $U_{\rm sg}$ was applied between the quasi 2DEG and the split gate. The series resistance of the Hallbar and the QPC as well as the Hall resistance outside the QPC have been measured at 100 mK using a standard Hall-bar geometry. The mobility of the electron gas is around 15 m^2/Vs, corresponding to a mean free path of about 1 μm.

The contact resistance of the QPC has been determined from the difference between the measured four-point resistance across the split gate and the resistance of the Hall bar, which was measured separately at $U_{\mathrm{sg}} = 0\,\mathrm{V}$. Small corrections to the Hall-bar resistance of the order of a few percents were necessary to map the lowest conductance plateau to the value of $2e^2/h$. From the plateau values $2Ne^2/h$ of the conductance we found the number N of occupied 1D-subbands.

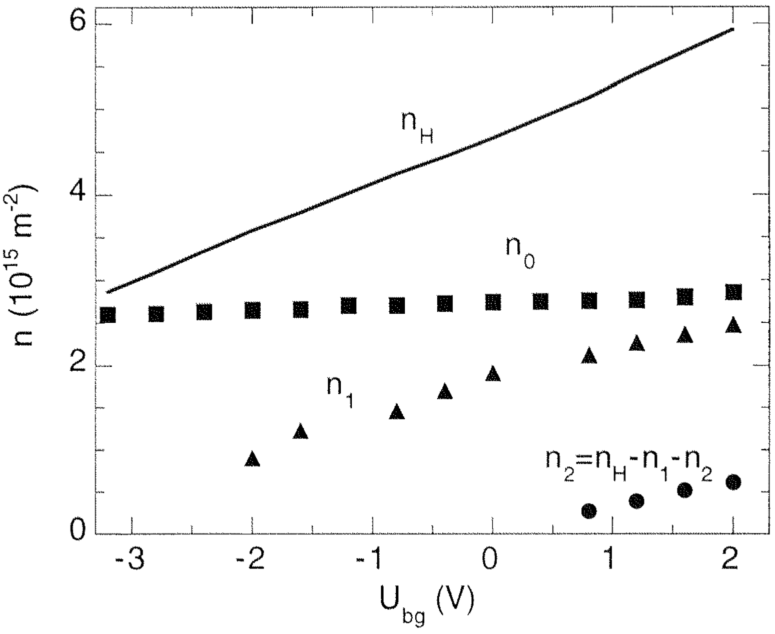

Figure 7.4: Measured Hall density n_{H} and subband densities n_0, n_1 and n_2 vs. U_{bg} for sample 34A. The subband density n_2 was obtained from the measured n_{H}, n_0 and n_1.

7.3 Tuning the Shape of the Constriction

The lithographic width of the split-gate opening is 400 nm. By applying negative gate voltages U_{sg}, the width gets smaller and simultaneously the electron density in the channel decreases, because of an increase of the conduction band edge E_c in the constriction. Self-consistent solutions of the Schrödinger and Poisson equations for channels defined by a split-gate have shown that the confining potential is parabolic with a flat bottom [34]. For small openings a pure parabolic confinement $U(y) = m\omega_y^2 y^2/2$ is a good approximation. The width W of the split-gate can be defined by the separation of the equipotentials at the Fermi energy. With $W = 2y'$ and $U(y') = E_{\mathrm{F}} - E_c$ one obtains

$$W = 2\sqrt{\frac{2(E_{\mathrm{F}} - E_c)}{m\omega_y^2}} \propto \frac{1}{\omega_y}. \tag{7.1}$$

The electron density in the constriction is determined by the position of the Fermi energy E_{F} relative to the conductance band edge minimum in the QPC. For constrictions defined by split-gate electrodes, ω_y usually does not vary much with decreasing U_{sg}. The main effect of U_{sg} is to lift the conductance band E_c relative to E_{F}, until the last channel is depleted.

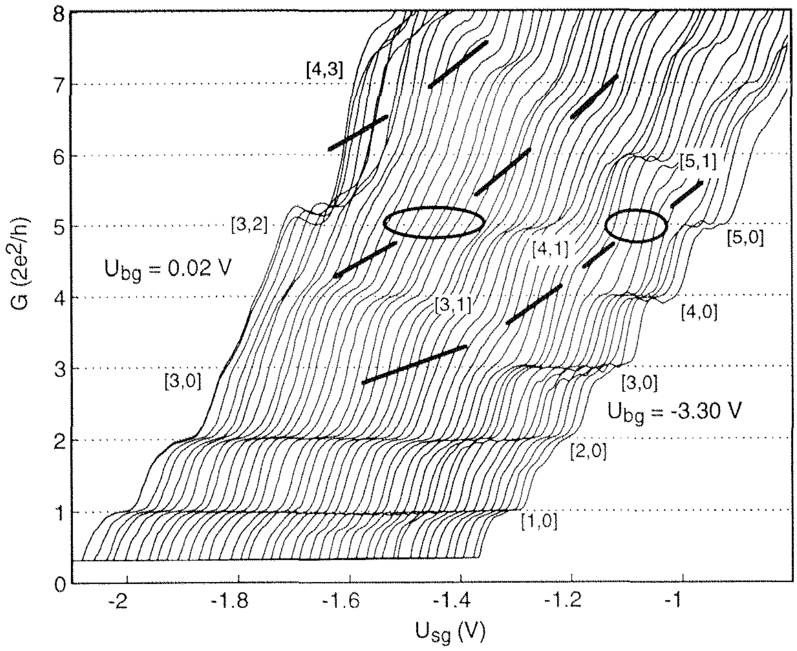

Figure 7.5: Measured conductance vs U_{sg} for different U_{bg} between -3.3 V and +0.02 V in steps of 0.08 V at $B_\perp = 0.2\,\mathrm{T}$. (sample 34A). The dashed lines mark positions, where 1D subbands with different m are filled simultaneously and therefore one conductance plateau is skipped. The two curls indicate positions where simultaneous filling of $(0,1)$ and $(4,0)$ repectively $(1,1)$ and $(3,0)$ occurs.

The confinement along the y-direction has been estimated by dividing $E_{\mathrm{F}} - E_c$ by the number of occupied channels[1]. We have found a 1D subband spacing of $\Delta E \approx 2\,\mathrm{meV}$ for $U_{\mathrm{bg}} = 0\,\mathrm{meV}$.

We now discuss what happens if the confinement in z-direction is tuned by varying U_{bg}. Figure 7.4 shows the 2D subband densities n_0, n_1, and n_2 as obtained from SdH measurements and the Hall density n_{H} as a function of the back-gate voltage. The difference $n_0 - n_1$ monotonically decreases with increasing U_{bg}. This is due to the extension of the electron gas in z-direction with increasing density, as discussed in chapter 3.3. For increasing U_{bg}, the confinement in z-direction widens, whereas the y-direction remains unaffected to first approximation. Thus the shape of the 3D QPC-constriction gets more and more circular. The subband density difference $n_0 - n_1$ corresponds to a subband spacing ΔE of $9\,\mathrm{meV}$ at $U_{\mathrm{bg}} = -3.3\,V$ and of $3\,\mathrm{meV}$ at $U_{\mathrm{bg}} = 0\,V$.

The measured conductance as a function of U_{sg} is presented in Fig. 7.5. Different traces correspond to different U_{bg}. For $U_{\mathrm{bg}} = -3.30\,\mathrm{V}$, five well-resolved conductance plateaus are observed. Since for this gate voltage we expect the confinement in z-direction to be much stronger than in y-direction, we attribute these plateaus to channels belonging to the ground state of the z-confinement, labeled by $m = 0$. As U_{bg} is increased, the confinement in z-direction weakens, and channels with $m = 1$

---

[1] $E_{\mathrm{F}} - E_c$ in the channel has been obtained from measurements in a strong magnetic field perpendicular to the 2DEG, where $E_{\mathrm{F}} - E_c \approx \hbar\omega_c$, as described in Ref. [34].

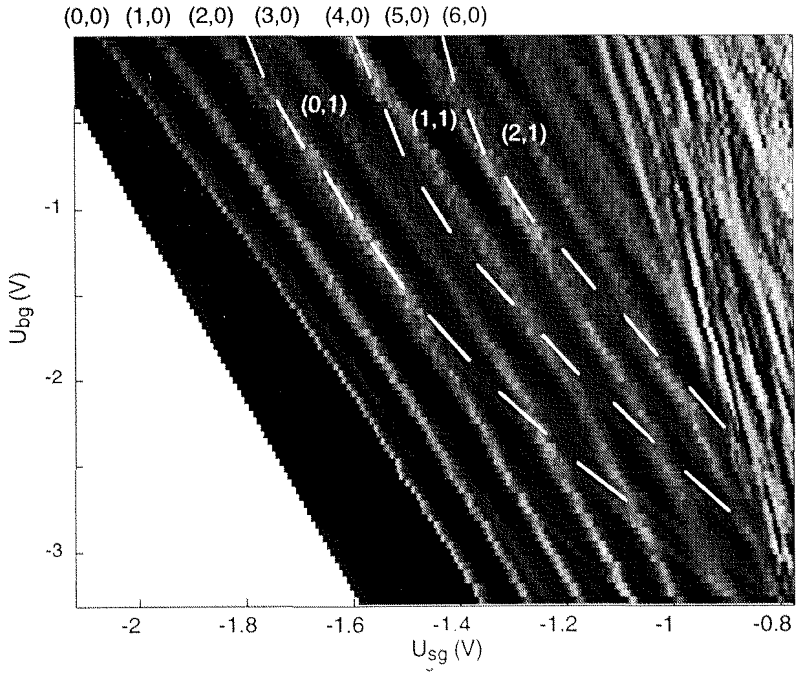

Figure 7.6: Transconductance dG/dU_{fg} as grayscale vs. U_{fg} and U_{bg}. Black regions correspond to conductance plateaus (low transconductance), while bright regions indicate crossings of the Fermi energy with a 1D subband energy, where the transconductance is high. Thus the bright lines correspond directly to the 1D subband energies, which are indicated by (l, m). The dashed lines indicate the location of the subband energies with $m = 1$. The structure at high U_{sg} and U_{bg} has not been reproduced and is attributed to resonance effects due to a nearby impurity.

get occupied. The first indication for this is the disappearance of the $N = 5$ plateau at $U_{\mathrm{bg}} = -3.0\,\mathrm{V}$ and $U_{\mathrm{sg}} = -1.03\,\mathrm{V}$. There, the energy of the $(l, m) = (4, 0)$-channel coincides with the energy of the $(0, 1)$-channel, and the two channels are occupied simultaneously. Thus the corresponding plateau at $N = 5$ disappears. We label the plateaus by $[l_0, l_1]$ with l_0 (l_1) the number of occupied channels with $m = 0$ ($m = 1$). The occupation numbers for the plateaus at $U_{\mathrm{bg}} = -3.3\,\mathrm{V}$ are $[1, 0], [2, 0], \ldots [5, 0]$.

A further increase of U_{bg} successively suppresses the $[4, 0]$ and $[3, 0]$-plateaus, while the $[2, 0]$- and $[1, 0]$ plateaus remain unaffected. This indicates that the shape of the constriction never gets completely circular, because then also the energy levels $(1, 0)$ and $(0, 1)$ would be degenerate and the $N = 2$ plateau would be missing. In fact, the $(1, 0)$ and $(0, 1)$-subbands can only be degenerate if an exactly circular shape is realized.

The plateau at $N = 5$ recovers at $U_{\mathrm{bg}} = -2.5\,\mathrm{V}$. It turned into $[4, 1]$ with four $m = 0$- and one $m = 1$-channel occupied. A further increase of U_{bg} suppresses the plateau again, which is attributed to the intermixing of the $(1, 1)$-state. At $U_{\mathrm{bg}} = -1.0\,\mathrm{V}$, the plateau recovers in the form of $[3, 2]$.

A better visualization of the energy structure is given by plotting the transconductance dG/dU_{sg} as grayscales against U_{sg} and U_{bg} (Fig. 7.6). Dark regions correspond to a conductance plateau. Their width is determined by the potential shape in trans-

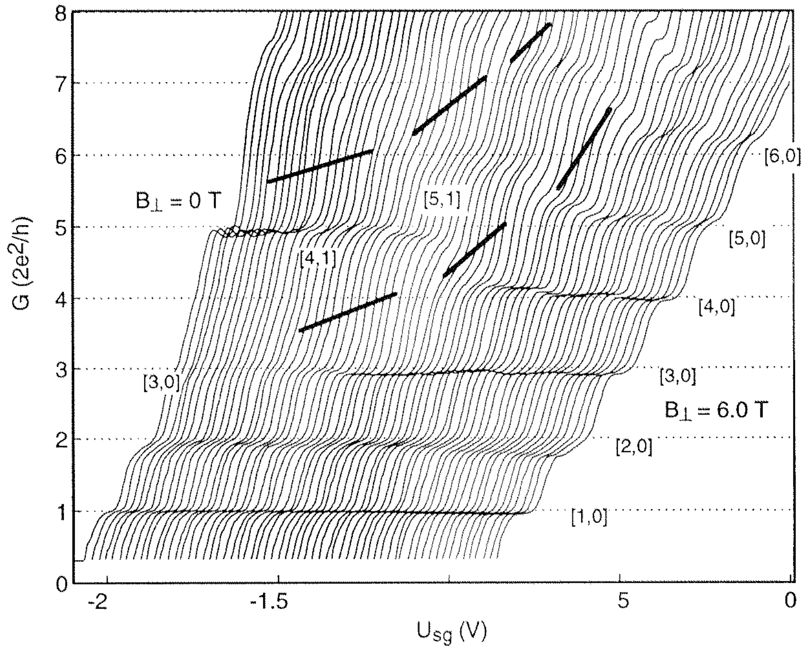

Figure 7.7: Measured G vs U_{sg} for different $B_\perp$ ($U_{\mathrm{bg}} = 0.0\,\mathrm{V}$). For clarity, the curves are offset in the U_{sg}-direction. The offset is increased by 20 mV from curve to curve. The $B_\perp$ values range between 0 and 6 T with steps of 0.1 T. With decreasing $B_\perp$, plateaus are successively destroyed, while plateaus with higher quantum numbers may be recovered at lower fields. The plateaus are labeled with numbers $[l_0, l_1]$ as discussed in the text.

port direction [144] and by $k_{\mathrm{B}}T$. The bright grayscales denote rising conductance edges, where 1D subbands cross the Fermi energy. The white dashed lines in Fig. 7.6 indicate the channels $(1,0)$,$(1,1)$, and $(1,2)$, which interfere with the $m = 0$-channels. We learn from Fig. 7.6 that at $U_{\mathrm{bg}} = -3.3\,\mathrm{V}$, the confinement in z-direction described by the frequency ω_z of the parabolic potential is at least five times stronger than in y-direction, while at $U_{\mathrm{bg}} = 0.0\,\mathrm{mV}$, the relation between ω_z and ω_y is about 1:2. As Eq. 7.1 tells us, the diameter y_0 (z_0) of the constriction is proportional to $1/\omega_y$ ($1/\omega_z$). Thus the shape of the opening is elliptic with axis ratio of $y_0/z_0 = \omega_z/\omega_y$, amounting to to 2:1 for $U_{\mathrm{bg}} = 0.0\,\mathrm{V}$ and 5:1 for $U_{\mathrm{bg}} = -3.3\,\mathrm{V}$.

7.4 1D Subband Spectrum in Magnetic Fields

In the following, we focus on $U_{\mathrm{bg}} = 0$, where in the 2DEG two subbands are occupied, and $n_{\mathrm{S}} = 4.6 \cdot 10^{15}\,\mathrm{m}^{-2}$. The two subband densities are determined from Shubnikov-de Haas oscillations and are found to be $n_0 = 2.6 \cdot 10^{15}\,\mathrm{m}^{-2}$ and $n_1 = 2.0 \cdot 10^{15}\,\mathrm{m}^{-2}$.

We applied a magnetic field in the direction perpendicular ($B_\perp$) and parallel ($B_\parallel$) to the direction of the current flow, but in the plane of the 2DEG (Fig. 7.1b). In Fig. 7.7 we present measurements at different $B_\perp$.

At $B_\perp = 0\,\mathrm{T}$, well defined conductance plateaus at N=1, 2 and 5 are observed. While there is a weak plateau at $N = 3$, the one at $N = 4$ is omitted. With increasing

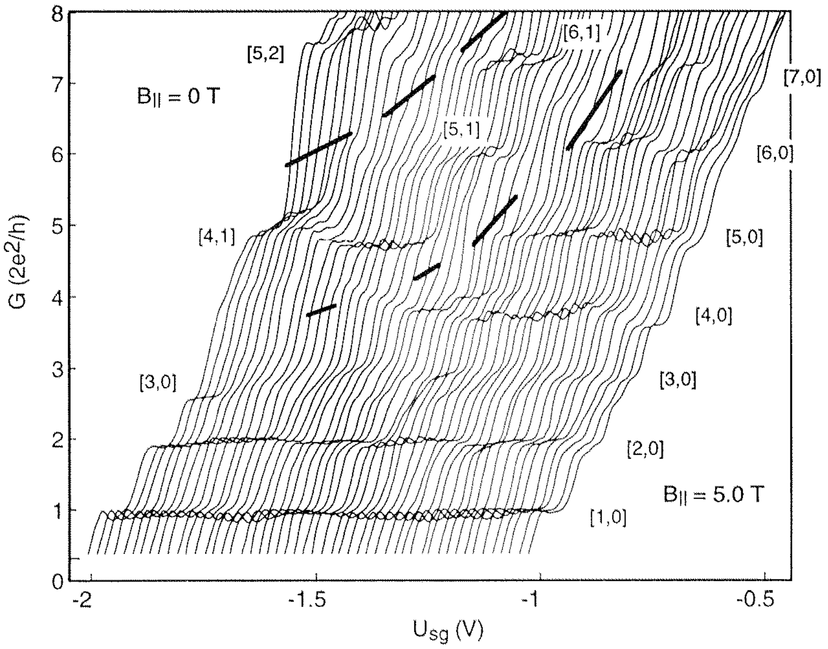

Figure 7.8: Measured conductance as a function of the split-gate voltage U_{sg} and for different magnetic fields $B_{\|}$ ($U_{\mathrm{bg}} = 0.5\,\mathrm{V}$). The curves are offset in the U_{sg}-direction by 20 mV each. The $B_{\|}$ values range from 0 and 5 T with a step size of 0.1 T.

$B_{\perp}$ the $N = 3$ plateau fully recovers at $B_{\perp} \approx 2$ T, and $N = 4$ recovers at 3.4 T. At this field, the plateau at $N = 5$ is suppressed. It recovers at around 4.2 T at a value which is close to $10e^2/h$. This suppression and recovery of conductance plateaus is attributed to the degeneracy of 1D subbands at the Fermi energy. As all observed plateaus seem to recover at higher fields, the suppression of $N = 5$ at $B_{\perp} = 3.4$ T is due to the crossing of the fifth level of the $m = 0$-ladder with the lowest level of the $m = 1$-ladder. The observed plateaus at $B_{\perp} = 0$ T are labeled by $[l_0, l_1]$ =[1,0], [2,0], [3,0], [4,1], [5,2], ..., while at $B_{\perp} = 6$ T the numbers are [1,0], [2,0], [3,0], [4,0], [5,0], ...

The conductance data in a parallel field $B_{\|}$ is presented in Fig. 7.8. For $B_{\|} = 5$ T, the $G(U_{\mathrm{sg}})$-trace showed seven plateaus at $N = 1, 2, \ldots 7$. In the presented measurement, the plateaus are less flat than usual. We attribute the wiggles in the plateaus to resonance effects in the constriction due to impurities nearby [129]. The $N = 3$-plateau is not well pronounced, but it never disappears completely. The $[5, 0]$-plateau evolves into a $[4, 1]$ plateau with decreasing field, and similarly $[6, 0]$ evolves into $[5, 1]$, whereas the $N = 7$ plateau is represented in three ways: $[7, 0]$,$[6, 1]$ and $[5, 2]$. The plateau at $N = 4$ seems to disappear at $B_{\|} < 2$ T, but the differential conductance shows that a small feature always remains at the plateau position, as will be discussed below.

In Fig. 7.9 we plot the transconductance dG/dU_{sg} in a gray scale plot as a function of U_{sg} and B. Two measurements are shown with the two different B directions parallel and perpendicular to the channel, respectively. In both plots, the crossing of the well resolved $m = 0$ ladder with the less pronounced $m = 1$ ladder can be seen. At a given field, subsequent conductance plateaus appear about equidistantly in U_{sg}.

With increasing field, the $m = 1$ ladder moves quickly away from the $m = 0$-ladder. This is explained by a diamagnetic shift of the 2D-subband energy difference [113]. The $m = 0$-ladder spacing strongly depends on the orientation of the magnetic field. For $B_\perp$, it increases with increasing field, for $B_{||}$, it decreases.

In order to understand the structure shown in Fig. 7.9, we model the energy levels of a parabolic constriction given by

$$U(y, z) = \frac{m^*}{2}\left(\omega_y^2 y^2 + \omega_z^2 z^2\right), \tag{7.2}$$

For perpendicular fields along the y-direction the gauge $\mathbf{A} = (B_\perp z, 0, 0)$ is used, for parallel fields along the x-direction $\mathbf{A} = (0, -B_{||} z, 0)$. We first discuss the perpendicular-field case, before we move to the mode-coupling in the parallel case.

In the Hamiltonian, $B_\perp$ couples to the x- and z directions which are perpendicular to the field direction. Along the "free" x-direction, the dispersion relation and thus the effective mass is modified, whereas the z-confinement is enhanced due to the diamagnetic shift proportional to $(1 + \omega_{c,\perp}^2/\omega_z^2)^{(1/2)}$. A term which couples the z- and x-direction results in a shift of the Fermi surface in k_x-direction. Neglecting electron-electron interactions, no coupling of the y- and z direction is expected, such that the 1D subbands cross each other. For a parabolic confinement, the subband energies are given by

$$E_{l,m} = \hbar\omega_y(l + 1/2) + \hbar\sqrt{\omega_z^2 + \omega_{c,\perp}^2}(m + 1/2), \tag{7.3}$$

where $\omega_{c,\perp} = eB_\perp/m^*$ is the cyclotron frequency. Fig. 7.9c shows the energy fan for $\omega_y = 2.0\,\mathrm{meV}$ and $\omega_z = 5.0\,\mathrm{meV}$. The $m = 0$-ladder crosses the $m = 1$-ladder without any indication of coupling. The step size remains constant with $B_\perp$. The spread of the step-size with increasing $B_\perp$ in the measurement (Fig. 7.9a) can be explained by a DOS-reduction in the 2DEG outside the QPC, leading to a decrease of the Fermi energy with increasing $B_\perp$ [114, 109]. For the confinement potential given by Eq. 7.2, the DOS increases with $B_\perp$ as $(1 + \omega_c^2/\omega_z^2)^{1/2}$ [111], where ω_c is the cyclotron frequency.

For magnetic fields $B_{||}$ parallel to the current direction, the dominant effect is the change in energy spacing of the 1D subband ladders. The magnetic field couples the z- and the y-direction, which are both electrically confined by the QPC opening. In a situation with rotational symmetry along the field direction, this leads to the ordinary Zeeman effect, similar to the splitting of the Darwin-Fock states. A calculation of the energy levels for parabolic confinements with arbitrary ω_y and ω_z gives the result (see Appendix B)

$$E_{l,m} = \hbar\omega_1(l + 1/2) + \hbar\omega_2(m + 1/2), \tag{7.4}$$

with

$$\omega_{1,2}^2 = \frac{1}{2}\left(\omega_c^2 + \omega_y^2 + \omega_z^2\right) \pm \frac{1}{2}\sqrt{\left(\omega_c^2 + \omega_y^2 + \omega_z^2\right)^2 - \omega_y^2\omega_z^2} \tag{7.5}$$

At $B = 0$, ω_1 corresponds to ω_y, and ω_2 is equal to ω_z. Figure 7.9d shows the calculated energy spectrum for $\omega_y = 2\,\mathrm{meV}$ and $\omega_z = 5\,\mathrm{meV}$. The larger of the two frequencies increases with $B_{||}$, while the smaller one decreases.

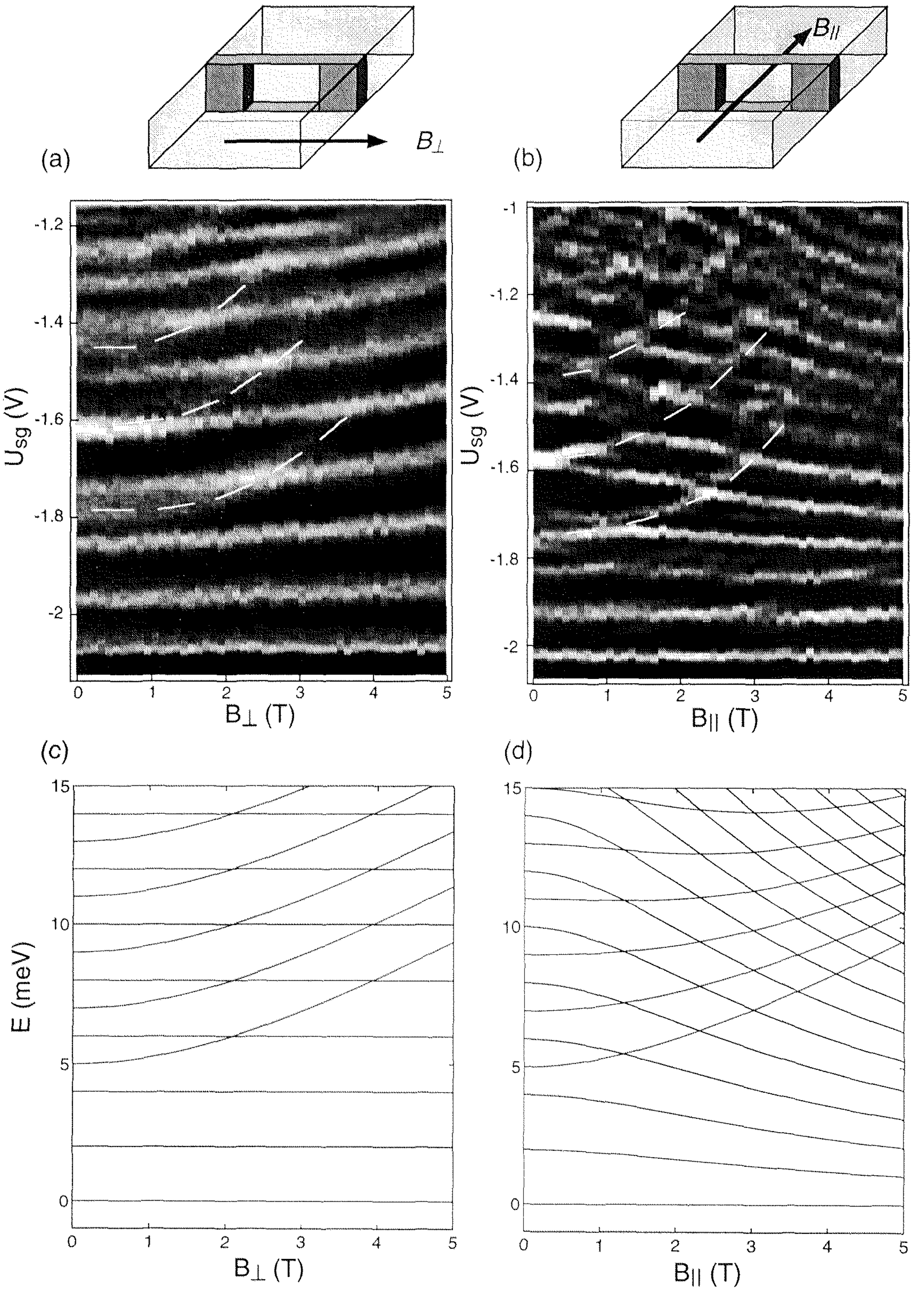

Figure 7.9: Grayscale plot of the transconductance dG/dU_{sg} as a function of U_{sg} and $B_\perp$ (a) and $B_\parallel$ (b). Black regions correspond to conductance plateaus (zero transconductance), while bright regions indicate rising edges of the conductance, and thus crossings of E_{F} with a 1D subband energy. Calculated 1D energy levels $E_{l,m}$ for a 3D QPC with magnetic field $B_\perp$ perpendicular (c) and $B_\parallel$ parallel (d) to the current direction. The energies are indicated relative to $E_{0,0}$. The constriction is defined by $\omega_y = 2\,\mathrm{meV}$ and $\omega_z = 5\,\mathrm{meV}$.

In the experiment at $U_{\mathrm{bg}} = 0.5\,\mathrm{V}$ and $U_{\mathrm{sg}} = -1.3\,\mathrm{V}$, the number of occupied 1D levels of the $m = 0$-ladder increases from 7 at zero field to about 11 for $B_{||} = 5\,\mathrm{T}$, corresponding to a decrease of the spacing of the lower 1D subband ladder. Assuming that the ladder steps are also spread due to the DOS-effect by a factor of 6/5 at $B_{\perp} = 5.0\,\mathrm{T}$, we arrive at a filling of $N \approx 13$, which is in agreement with the calculated energy spectrum in Fig. 7.9d.

If the QPC confinement is not exactly parabolic, the Hamiltonian cannot be decoupled into two parabolic oscillators because of the magnetic confinement. The energy levels anticross as a function of $B_{||}$. This effect has been calculated for dots in the special case of a square well confinement [145, 135]. An indication for such an anticrossing in our 3D QPC is presented in Fig 7.10, which is a close-up of the measurements shown in Fig. 7.9. The $(3, 0)$ level does not cross the $(0, 1)$ level. A small dark region always remains. This means that the transconductance has always two peaks, which stay separate. The plateau-like feature in the $G(U_{\mathrm{sg}})$-traces never completely disappears at $N = 4$, see Fig. 7.8.

As an illustration, we calculated the energy spectrum for a parabolic potential in z-direction disturbed by a potential spike in the form of a three monolayer thick $\mathrm{Al_{0.05}Ga_{0.95}As}$-layer at $z = 0$. We started with the analytically obtained wave functions for a parabolic confinement in y- and z-direction and $B_{||}$ along the x-direction, and treat the spike in first-order perturbation theory. By diagonalization of the Hamiltonian considering the states $m = 0, l = 0, 1, 2, 3, 4$ and $m = 1, l = 0, 1, 2$ we obtain the energy levels plotted in Fig. 7.11. A splitting of most levels is observed. The splitting is smaller than in the experiment (close-up in Fig. 7.10). Note that the separation between the $m = 0$- and the $m = 1$-ladder decreases when a spike is introduced. This is similar to the decrease of the 2D subband spacing, as was calculated in first-order perturbation theory in chapter 3.

7.5 Conclusions

In conclusion, we measured the subband energies of a 3D QPC realized on a semiconductor PQW structure by analyzing the transconductance through the QPC at different magnetic fields with two different orientations parallel to the 2DEG. In the case where B is oriented perpendicular to the axis of the 3D QPC, coupling between 1D subbands is neither observed nor expected. For field directions along the direction of current, a level anticrossings is observed. We cannot attribute this anticrossing to the influence of a potential spike alone, because it is too strong. Other non-parabolicities of the confining potential might be the cause of the observed anticrossing. We have found no level-lockings within the experimental resolution.

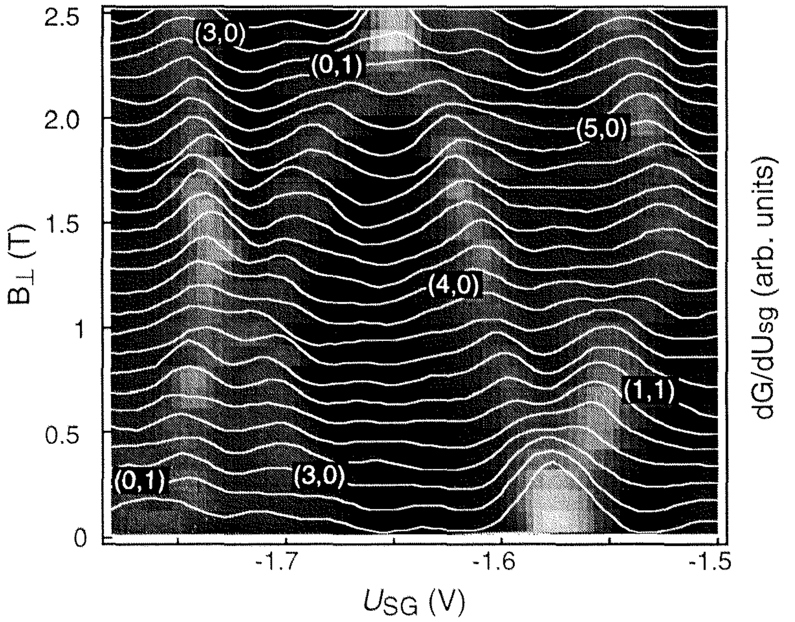

Figure 7.10: Close-up of Fig. 7.9b, showing anticrossing of the (0, 1) with the (3, 0) level. In addition to the grayscale of the transconductance, the individual transconductance traces are shown explicitly.

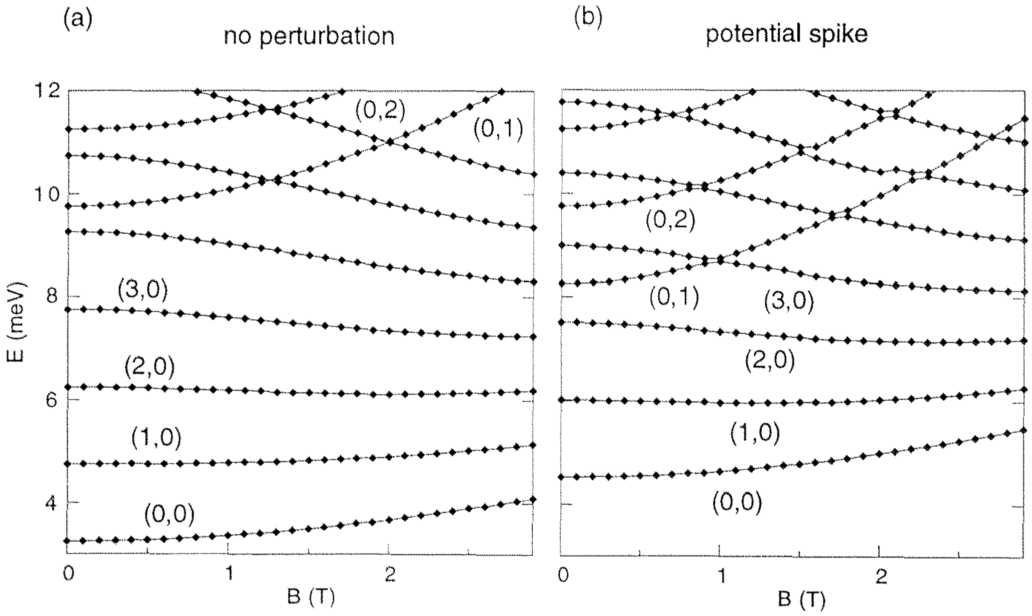

Figure 7.11: Calculated energy spectrum for $\omega_y = 1.5\,\text{meV}$ and $\omega_z = 5.0\,\text{meV}$ (a) without spike and (b) with a 8.5 Å thick $Al_{0.05}Ga_{0.95}As$ potential spike at fixed z-position.

Chapter 8

Conclusions and Outlook

Parabolic quantum wells have been realized in the AlGaAs-GaAs-system in a very precise way using molecular beam epitaxy. They represent a unique model system in which quantum states and their respective influence on classical and semi-classical phenomena can be investigated.

We have measured the width of the electron gas as a function of the electron sheet density and introduced a method to map out the quantum-mechanical density distribution of the electrons. Transport experiments are a versatile tool to study the single-particle energy levels. For the considered samples, it has been found that the electron energy quantization in magnetic fields of arbitrary orientation can be understood by considering text-book examples of quantum mechanical problems describing single electrons in quantum wells. It has been found that the obvious model not always describes the experimental results. For a multi-subband system in an in-plane magnetic field, a second-order effect modifies the first-order result by a factor of seven, in agreement with the measurements.

Intersubband scattering and multi-subband screening determines the mobility of wide electron gases. The model system of a PQW allows the displacement of the electron distribution along the growth direction. We have used this fact to demonstrate a new method to investigate the spatial distribution of scatterers across the structure.

In addition to the parabolic well confinement, the electron gas has been confined in one lateral direction using sub-micrometer lithography techniques. We have fabricated a QPC in which the one-dimensional subbands are described by two quantum numbers. Interactions between subbands with variable energy separation have been measured and have been described by a generalized Darwin-Fock model.

A next step would be the confinement of the third direction. In this way 0D dots would be defined, where three quantum numbers determine the energy levels. Such a complex system would allow the study of multiple tunable energy degeneracies in a few-electron system, where many-particle interactions might be investigated in detail.

In 2D electron focusing experiments in multi-subband systems, the individual subbands are expected to modify the resistance due to their different cyclotron radius. Commensurability between the respective cyclotron radius and the sample geometry leads to peaks in the magnetoresistance. This allows the study the interaction between 2D subbands. It is an example of how classical behavior, namely the cyclotron motion of electrons, is influenced by the population of an additional quantum state. Parabolic quantum wells are in the special regime where the cross-over from two to three dimensional systems can be investigated. Intersubband scattering still holds many open questions, in particular with respect to inelastic scattering events. A more profound investigation on how scattering between electrons of the same subband and between different subbands affects the phase coherence length will be necessary.

Shubnikov-de Haas minima at odd integer filling factors are governed by spin effects. Preliminary experiments have shown that additional structure shows up in the magnetoresistance being related to competing spin levels of different subbands. More detailed studies in this regime might unravel the complicated situation of neighboring Landau levels that are described by three quantum numbers, i.e. subband, Landau and spin quantum number.

With self-aligned gate technique [146, 147], QPCs can be fabricated where the electron densities in- and outside the one-dimensional channel are controlled independently by different gate electrodes. A situation can be realized, where electrons from the lower subband are injected into an upper subband. By varying the energy between the Fermi seas in the source and drain electrode more details of the intersubband scattering process might be found.

Appendix A

Comparison of Screening Approximations

In this appendix we investigate the influence of the screening approximation on the scattering times. We compare results obtained for Thomas Fermi screening and RPA screening and investigate the effect of a third subband in the RPA matrix formalism for two occupied subbands.

Figure A.1 presents calculated scattering times for $N_1 = 3 \cdot 10^{16}\,\mathrm{m}^{-2}$, $N_2 = 1.3 \cdot 10^{15}\,\mathrm{m}^{-2}$ and $N_3 = 1.5 \cdot 10^{15}\,\mathrm{m}^{-2}$ (for a definition of N_i see chapter 4.2.5).

In (a) and (b), $n_{\mathrm{H}} = 2.9 \cdot 10^{15}\,\mathrm{m}^{-2}$ was kept constant and the electron gas was displaced along the growth direction. In (a), the Thomas-Fermi result is compared to the 3-subband RPA result. The scattering times correspond reasonably for both subbands. In (b), the RPA result obtained for a 2-subband matrix is compared to that of a 3-subband matrix. A qualitative change is observed: In the 2-subband RPA result, the upper-subband scattering time is larger than the lower-subband scattering time.

In (c) and (d), we compare results for different n_{H} obtained by keeping $U_{\mathrm{bg}} = 0$ and varying U_{fg}. Again the 3-subband RPA result agrees better with the TF result than with the 2-subband RPA data.

We therefore conclude that the RPA-matrix formalism is not a good approximation to our 2-subband PQW system. Better results are obtained by regarding virtual screening of an unocuppied third subband, or by considering TF screening.

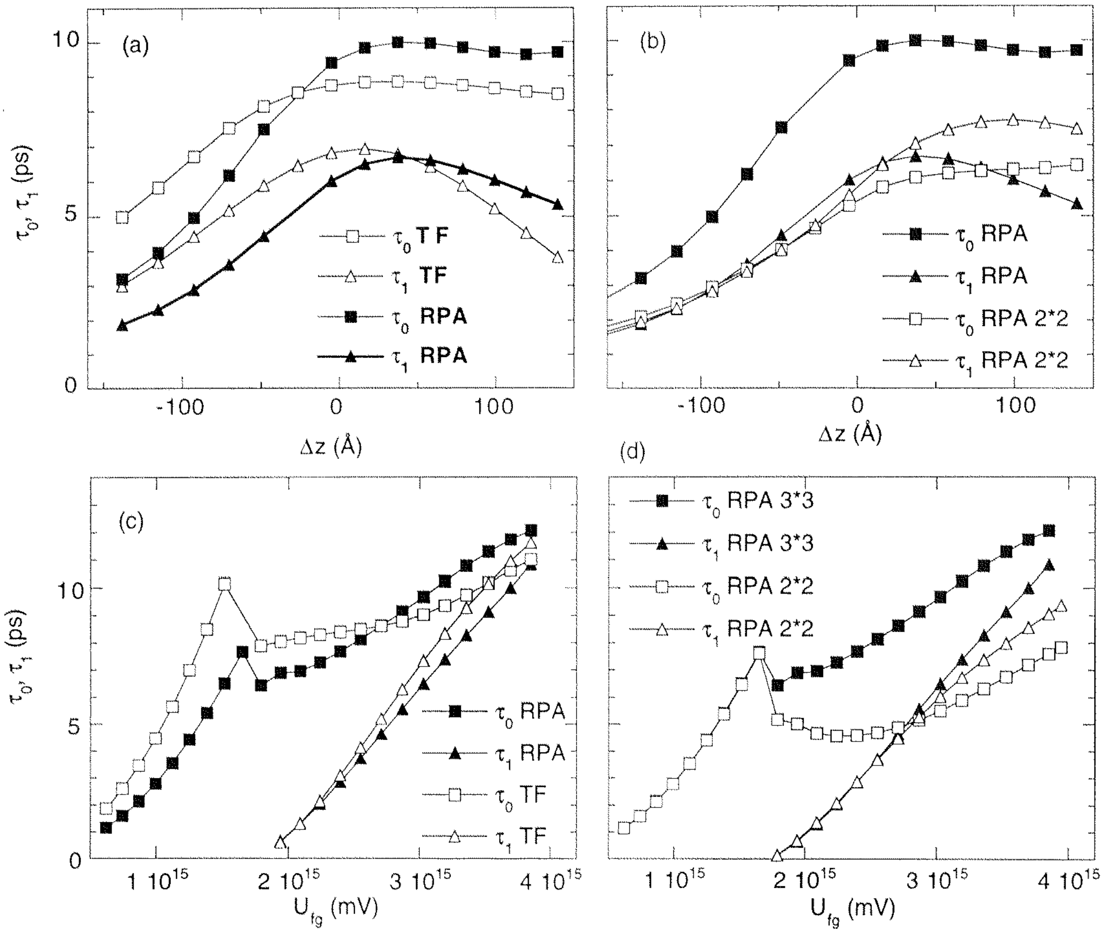

Figure A.1: Comparision of calculated scattering times. In (a) and (b), simulations of the scattering times as a function of the electron-gas displacement across the PQW are shown. In (a), the TF approximation is compared to a three-subband RPA. In (b), the three-subband RPA is compared to the two-subband RPA. Similar data is shown in (c) and (d) for the scattering times as a function n_{H} varied by U_{fg}.

Appendix B

2D Parabolic Confinement

We calculate the energy states and wave functions of electrons confined parabolically in two dimensions and in a magnetic field $B_{\|}$ (Fig 7.1a). In the gauge $\mathbf{A} = (0, -B_{\|}z, 0)$, we obtain the Hamiltonian

$$H = \frac{p_y^2}{2m} + \frac{p_z^2}{2m} + \frac{m}{2}\omega_y^2 y^2 + \frac{m}{2}(\omega_c^2 + \omega_z^2)z^2 + \omega_c p_y z. \tag{B.1}$$

In the general case, the cross-term containing $p_y z$ hinders the separation of the problem into y and z direction. If $B = 0$ and thus $\omega_c = 0$, one readily obtains two decoupled harmonic oscillators with frequencies ω_y and ω_z. The cross-term can be removed by a rotational transformation. We regard the two-dimensional space with p_y and z as coordinates. The new "spatial" coordinates u and v are obtained by

$$\begin{pmatrix} z \\ \frac{p_y}{m\omega_y} \end{pmatrix} = \begin{pmatrix} \cos\theta & -\sin\theta \\ \sin\theta & \cos\theta \end{pmatrix} \begin{pmatrix} u \\ v \end{pmatrix}. \tag{B.2}$$

Correspondingly p_z and y transform into the "momentum" coordinates Π_u and Π_v:

$$\begin{pmatrix} p_z \\ -ym\omega_y \end{pmatrix} = \begin{pmatrix} \cos\theta & -\sin\theta \\ \sin\theta & \cos\theta \end{pmatrix} \begin{pmatrix} \Pi_u \\ \Pi_v \end{pmatrix}. \tag{B.3}$$

The minus sign in y is necessary in order to fulfill the commutation relations:

$$\begin{aligned} [u, \Pi_u] &= i\hbar && \text{(B.4)} \\ [v, \Pi_v] &= i\hbar && \text{(B.5)} \\ [u, v] &= 0 && \text{(B.6)} \\ [\Pi_u, \Pi_v] &= 0 && \text{(B.7)} \\ & && \text{(B.8)} \end{aligned}$$

The Hamiltonian expressed in the transformed coordinates contains a cross term proportional to uv, which we require to vanish:

$$\left[m\omega_c\omega_y \cos 2\theta - \frac{m\left(\omega_c^2 - \omega_y^2 + \omega_z^2\right)}{2} \sin 2\theta \right] uv = 0 \tag{B.9}$$

In any case no cross term proportional to $\Pi_u \Pi_v$ appears, such that the problem has been separated once this equation is fulfilled. The solution given by the rotation-angle θ is expressed as

$$\cos 2\theta = -\frac{\left(\omega_c^2 - \omega_y^2 + \omega_z^2\right)}{\sqrt{\omega_c^4 + \omega_y^4 + \omega_z^4 - 2\omega_y^2\omega_z^2 + 2\omega_c^2(\omega_y^2 + \omega_z^2)}}. \tag{B.10}$$

The decoupled Hamiltonian then reads

$$H = \frac{\Pi_u^2}{2m} + \frac{\Pi_v^2}{2m} + \frac{m}{2}\omega_u^2 u^2 + \frac{m}{2}\omega_v^2 v^2, \tag{B.11}$$

with the frequencies

$$\omega_{u,v}^2 = \frac{1}{2}(\omega_c^2 + \omega_y^2 + \omega_z^2) \mp \frac{1}{2}\sqrt{\omega_c^4 + \omega_y^4 + \omega_z^4 - 2\omega_y^2\omega_z^2 + 2\omega_c^2(\omega_y^2 + \omega_z^2)}. \tag{B.12}$$

We now solve the Schrödinger equation

$$H\varphi_{i,j} = E_{i,j}\varphi_{i,j} \tag{B.13}$$

The energy eigenvalues are evidently given by

$$E_{i,j} = \hbar\omega_u(i + 1/2) + \hbar\omega_v(j + 1/2) \tag{B.14}$$

We focus our attention on the wave functions $\phi_{i,j}$. For its calculation we construct the ladder operators

$$a_u = \frac{1}{\sqrt{2}}\left(\frac{u}{u_0} + i\frac{u_0\Pi_u}{\hbar}\right) \tag{B.15}$$

$$a_v = \frac{1}{\sqrt{2}}\left(\frac{v}{v_0} + i\frac{v_0\Pi_v}{\hbar}\right) \tag{B.16}$$

$$a_u^\dagger = \frac{1}{\sqrt{2}}\left(\frac{u}{u_0} - i\frac{u_0\Pi_u}{\hbar}\right) \tag{B.17}$$

$$a_v^\dagger = \frac{1}{\sqrt{2}}\left(\frac{v}{v_0} - i\frac{v_0\Pi_v}{\hbar}\right). \tag{B.18}$$

Here we introduced the length scales $u_0 = \sqrt{\hbar/\omega_u m^*}$ and $v_0 = \sqrt{\hbar/\omega_v m^*}$, respectively. The ground state is defined by $a_u a_v \varphi_{0,0} = 0$. Expressed in the unrotated coordinates y and z, one obtains the coupled differential equation ($y_0 = \sqrt{\hbar/\omega_y m^*}$)

$$\frac{d}{dy}\varphi_{0,0}(y,z) = \frac{-2\omega_y y + i(\omega_v - \omega_u)\sin 2\theta\, z}{y_0^2(\omega_u + \omega_v + (\omega_v - \omega_u)\cos 2\theta)}\varphi_{0,0}(y,z) \tag{B.19}$$

$$\frac{d}{dz}\varphi_{0,0}(y,z) = \frac{i(\omega_v - \omega_u)\sin 2\theta\, y - 2\omega_u\omega_v/\omega_z\, z}{y_0^2(\omega_u + \omega_v + (\omega_v - \omega_u)\cos 2\theta)}\varphi_{0,0}(y,z), \tag{B.20}$$

which can be solved by the ansatz

$$\varphi_{0,0}(y,z) = C\exp[\alpha x^2 + \beta y^2 + \gamma xy]. \tag{B.21}$$

One obtains

$$\alpha = -\frac{\omega_y}{y_0^2(\omega_u + \omega_v + (\omega_v - \omega_u)\cos 2\theta)} \tag{B.22}$$

$$\beta = -\frac{\omega_u\omega_v/\omega_z}{y_0^2(\omega_u + \omega_v + (\omega_v - \omega_u)\cos 2\theta)} \tag{B.23}$$

$$\gamma = \frac{i(\omega_v - \omega_u)\sin 2\theta}{y_0^2(\omega_u + \omega_v + (\omega_v - \omega_u)\cos 2\theta)}. \tag{B.24}$$

The normalization of $\varphi_{0,0}$ is obtained by choosing

$$C = \left(\frac{2\sqrt{\alpha\beta}}{\pi}\right)^{1/2}. \tag{B.25}$$

Higher states can be constructed by applying the creation operators $a_u^\dagger$ and $a_v^\dagger$ on the ground state:

$$\varphi_{i,j}(y,z) = \frac{1}{\sqrt{i!}\sqrt{j!}}(a_u^\dagger)^i(a_v^\dagger)^j\varphi_{0,0}(y,z). \tag{B.26}$$

We finally give the explicit form of the creation operators:

$$a_u^\dagger = i\sin\theta\left(\frac{\omega_y}{\omega_u}\frac{1}{u_0}y - \frac{\omega_u}{\omega_y}u_0\frac{d}{dy}\right) + \cos\theta\left(\frac{1}{u_0}z - u_0\frac{d}{dz}\right) \tag{B.27}$$

$$a_v^\dagger = i\cos\theta\left(\frac{\omega_y}{\omega_v}\frac{1}{v_0}y - \frac{\omega_v}{\omega_y}u_0\frac{d}{dy}\right) + \sin\theta\left(\frac{1}{v_0}z - v_0\frac{d}{dz}\right). \tag{B.28}$$

Note that when $\omega_c = 0$ then $\cos\theta = 0$, $\sin\theta = -1$, $\omega_u = \omega_y$ and $\omega_v = \omega_z$.

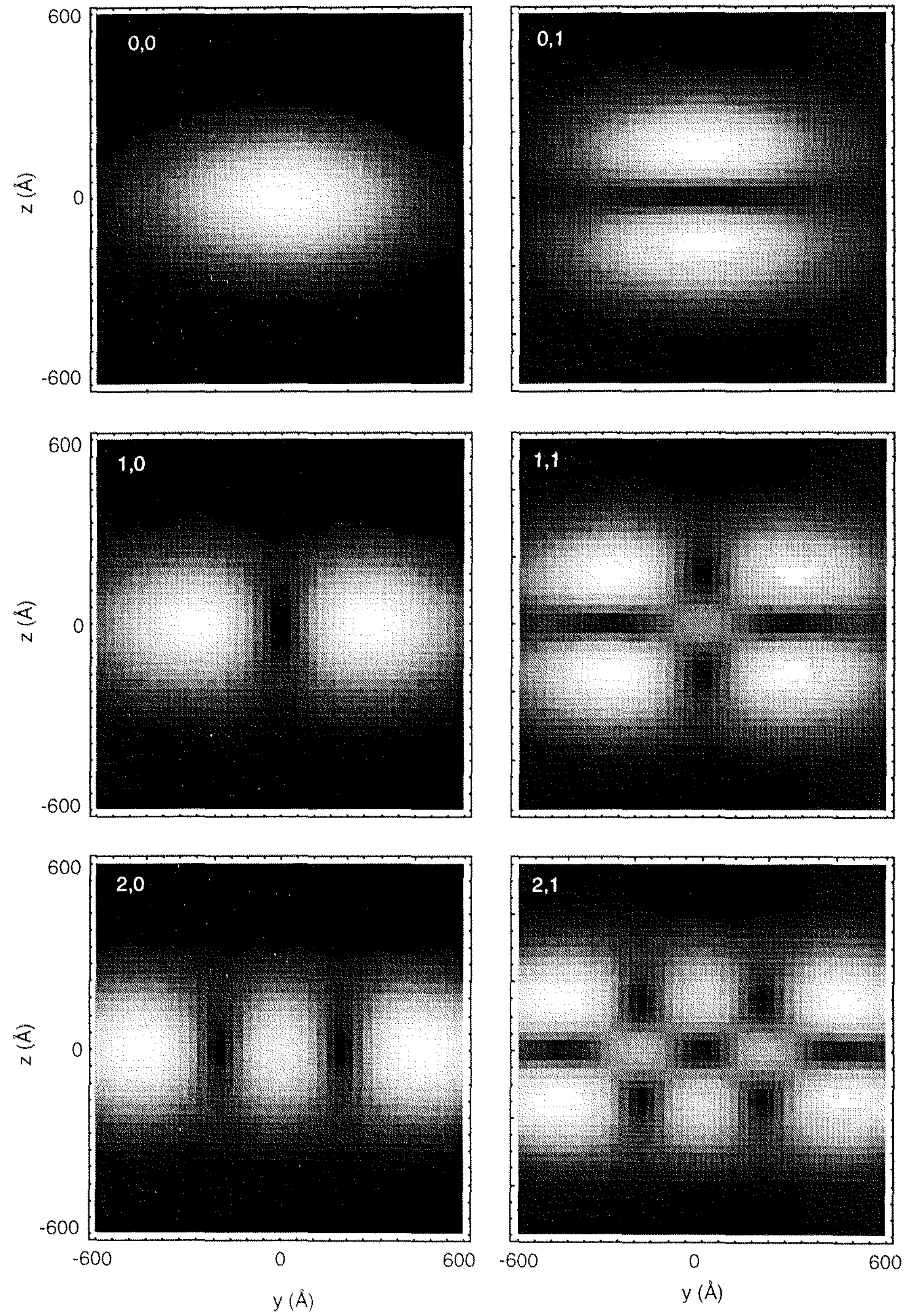

Figure B.1: Wave functions of a 2D constriction with parabolic confinements described by $\hbar\omega_y = 1.5\,\mathrm{meV}$ and $\hbar\omega_z = 5.0\,\mathrm{meV}$. A magnetic field of $B = 1\,\mathrm{T}$ was assumed perpendicular to the constriction.

Appendix C

List of Samples

sample	potential spike	wafer	structure
6	x=0.1	941027A	old Hall bar
21	x=0.05	961117B	old Hall bar
22	x=0.10	961117C	old Hall bar
18	x=0.15	961117D	old Hall bar
15	x=0.00	961117A	old Hall bar
14	x=0.15	941027A	old Hall bar
17	x=0.05	961117B	old Hall bar
33A	x=0.05	961117B	new Hall bar, QPC
33AII	x=0.05	961117B	new Hall bar, QPC
33D	x=0.05	961117B	new Hall bar, QPC
43D1	x=0.15	961117D	thin UCF Hall bar

Publications

G. Salis, B. Graf, K. Ensslin, K. Campman, K. Maranowski and A. C. Gossard, "Wave Function Spectroscopy in Quantum Wells with Tunable Electron Density", Phys. Rev. Lett.**79**, 5106 (1997).

G. Salis, B. Ruhstaller, K. Ensslin, K. Maranowski and A. C. Gossard, "Subband Densities in Quantum Wells under In-Plane Magnetic Fields", Phys. Rev. B **58**, 1436 (1998).

G. Salis, K. Ensslin, K. Maranowski, K. Campman and A. C. Gossard, "Wave function spectroscopy in parabolic quantum wells", Physica E **1**, 254 (1998).

G. Salis, T. Heinzel, K. Ensslin, O. Homan, W. Bächtold, K. Maranowski and A. C. Gossard, "Spectroscopy of Coupled One-Dimensional Subbands in Parabolic Quantum Wells", Proceedings ICPS 24, Jerusalem, 1998.

G. Salis, K. Ensslin, K. B. Campman, K. Maranowski and A. C. Gossard, "Wave-function spectroscopy in parabolic quantum wells", Physica B **251**, 941 (1998).

G. Salis, P. Wirth, T. Heinzel, T. Ihn, K. Ensslin, K. Maranowski and A. C. Gossard, "Variation of elastic scattering across a quantum well", Phys. Rev. B **59**, R5304 (1999), in press.

G. Salis, T. Heinzel, K. Ensslin, O. Homan, W. Bächtold, K. Maranowski and A. C. Gossard, "Coupled one-dimensional subbands in in-plane magnetic fields", Physica B **256-258**, 384 (1998).

T. Heinzel, G. Salis, K. Ensslin, K. Maranowski and A. C. Gossard, "Investigation of the spatial variation of scattering venters in parabolic quantum wells", Phyica B **256-258**, 252 (1998).

T. Ihn, M. Huberty, G. Salis, K. Ensslin, O. Homan, W. Bächtold, K. Maranowski and A. C. Gossard, "Universal conductance fluctuations in a parabolic quantum well tunable from two- to three-dimensional behavior", Physica B, **256-258**, 401 (1998), and Proceedings ICPS 24, Jerusalem, 1998.

Bibliography

[1] K. v. Klitzing, G. Dorda, and M. Pepper, Phys. Rev. Lett. **45**, 494 (1980).

[2] R. Dingle, H. L. Störmer, A. C. Gossard, and W. Wiegmann, Appl. Phys. Lett. **33**, 665 (1978).

[3] H. L. Störmer, Surf. Sci. **132**, 519 (1983).

[4] R. B. Laughlin, Phys. Rev. Lett. **50**, 1395 (1983).

[5] D. C. Tsui, H. L. Störmer, and A. C. Gossard, Phys. Rev. Lett. **48**, 1559 (1982).

[6] C. Weisbuch and B. Vinter, *Quantum semiconductor structures* (Boston, Academic Press, 1991).

[7] R. Bate, G. Frazier, W. Frensley, and M. Reed, Technical report, TI Technical Journal, July-August (unpublished).

[8] B. I. Halperin, Jpn. J. Appl. Phys. **26**, 1913 (1987), suppl. 26-3.

[9] M. Sundaram, A. C. Gossard, J. H. English, and R. M. Westervelt, Superlattices and Microstructures **4**, 683 (1988).

[10] M. Shayegan, T. Sajoto, M. Santos, and C. Silvestre, Appl. Phys. Lett. **53**, 791 (1988).

[11] K. Karrai, H. D. Drew, M. W. Lee, and M. Shayegan, Phys. Rev. B **39**, 1426 (1989).

[12] A. Wixforth, M. Sundaram, K. Ensslin, J. H. English, and A. C. Gossard, Phys. Rev. B. **43**, 10000 (1991).

[13] W. Kohn, Phys. Rev. **123**, 1242 (1961).

[14] L. Brey, N. F. Johnson, and B. J. Halperin, Phys. Rev. B **40**, 10647 (1989).

[15] S. M. Sze, *Semiconductor Devices, Physics and Technology* (John Wiley & Sons, 1985).

[16] A. C. Gossard, M. Sundaram, and P. F. Hopkins, Semiconductors and Semimetals **40**, 153 (1994).

[17] A. C. Gossard, IEEE J. Quant. Electron. **22**, 1649 (1986).

[18] R. Jurk, K. Ensslin, P. F. Hopkins, and A. C. Gossard, Superlattices and Microstructures **15**, 325 (1994).

[19] K. Ensslin, H. Baum, P. F. Hopkins, and A. C. Gossard, Surf. Sci. **305**, 317 (1994).

[20] V. T. Dolgopolov, G. E. Tsydynzhapov, A. A. Shashkin, E. V. Deviatov, F. Hastreiter, M. Hartung, A. Wixforth, K. L. Campman, and A. C. Gossard, JETP Lett. **67**, 595 (1998).

[21] M. Hartung, A. Wixforth, K. Campmann, and A. Gossard, Superlattices and Microstructures **19**, 1 (1996).

[22] K. D. Maranowski, J. P. Ibbetson, K. L. Campman, and A. C. Gossard, Appl. Phys. Lett. **66**, 3459 (1995).

[23] P. F. Hopkins, PhD-thesis, Harvard University, Cambride, Massachusetts, 1990.

[24] R. Williams, *Modern GaAs processing methods* (Artech House, 1990).

[25] J. C. Slater, Phys. Rev. **76**, 1592 (1949).

[26] J. M. Luttinger and W. Kohn, Phys. Rev. **97**, 869 (1954).

[27] J. M. Luttinger, Phys. Rev. **84**, 814 (1951).

[28] P. Hohenberg and W. Kohn, Phys. Rev. B **136**, 864 (1964).

[29] W. Kohn and L. J. Sham, Phys. Rev. A **140**, 1133 (1965).

[30] L. Hedin and B. I. Lundqvist, J. Phys. C **4**, 2064 (1971).

[31] G. L. Snider, I. H. Tan, and E. L. Hu, J. of Appl. Phys. **68**, 2849 (1990).

[32] I. H. Tan, G. L. Snider, and E. L. Hu, J. of Appl. Phys. **68**, 4071 (1990).

[33] K. Ensslin, D. Heitmann, and K. Ploog, Surf. Sci. **228**, 456 (1990).

[34] C. W. J. Beenakker and H. van Houten, *Solid State Physics, Vol. 44*, eds. h. ehrenreich and d. turnbull ed. (Academic Press, Boston, 1991).

[35] T. Ando and Y. Uemura, J. Phys. Soc. Jpn. **36**, 959 (1974).

[36] R. R. Gerhardts, Surf. Sci. **58**, 227 (1976).

[37] G. Gobsch, D. Schulze, and G. Paasch, Phys. Rev. B **38**, 10943 (1988).

[38] R. Kusters, Ph.D. thesis, Katholieke Universiteit te Nijmegen, 1990.

[39] R. M. Kusters, J. Singleton, G. Gobsch, G. Paasch, D. Schulze, F. A. Wittekamp, G. A. C. Jones, J. E. F. Frost, D. C. Peacock, and D. A. Ritchie, Superlattices-and-Microstructures **9**, 55 (1991).

[40] K. Ensslin, A. Wixforth, M. Sundaram, P. Hopkins, J. English, and A. Gossard, Phys. Rev. B **47**, 1366 (1993).

[41] G. Salis, K. Ensslin, K. Maranowski, K. Campman, and A. C. Gossard, Physica E **1**, 254 (1988).

[42] Y. Guldner, J. P. Vieren, M. Voos, F. Delahaye, D. Dominguez, J. P. Hirtz, and M. Razeghi, Phys. Rev. B **33**, 3990 (1986).

[43] K. Ensslin, M. Sundaram, A. Wixforth, and A. C. Gossard, Surf. Sci. **267**, 553 (1991).

[44] G. Salis, K. Ensslin, K. B. Campman, K. Maranowski, and A. C. Gossard, Physica B **251**, 941 (1998).

[45] M. F. Crommie, C. P. Lutz, and D. M. Eigler, Science **262**, 218 (1993).

[46] M. F. Crommie, C. P. Lutz, and D. M. Eigler, Nature **363**, 524 (1993).

[47] G. Salis, B. Graf, K. Ensslin, K. Campman, K. Maranowski, and A. C. Gossard, Phys. Rev. Lett. **79**, 5106 (1997).

[48] J.-W. Sakai, T. M. Fromhold, P. H. Beton, L. Eaves, M. Henini, P. C. Main, and F. W. Sheard, Phys. Rev. B **48**, 5664 (1993).

[49] B. Kardynal, C. H. W. Barnes, E. H. Linfield, D. A. Ritchie, J. T. Nicholls, K. M. Brown, G. A. C. Jones, and M. Pepper, Phys. Rev. B **55**, R1966 (1997).

[50] J.-Y. Marzin and J.-M. Gérard, Phys. Rev. Lett. **62**, 2172 (1989).

[51] T. C. Hsieh, T. Miller, and T.-C. Chiang, Phys. Rev. Lett. **55**, 2483 (1985).

[52] E. Ribeiro, E. Müller, T. Heinzel, H. Auderset, K. Ensslin, G. Medeiros-Ribeiro, and P. M. Petroff, Phys. Rev. B **58**, 1506 (1998).

[53] Ashcroft and Mermin, *Solid State Physics*, international ed. (Saunders College, 1976).

[54] E. D. Siggia and P. C. Kwok, Phys. Rev. B **2**, 1024 (1970).

[55] L. Hedin and S. Lundqvist, Solid State Physics **23**, 2 (1969), eds. F. Seitz, D. Turnbull and H. Ehrenreich.

[56] F. Stern, Phys. Rev. Lett. **18**, 546 (1967).

[57] J. K. Jain and S. D. Sarma, Phys. Rev. B **36**, 5949 (1987).

[58] R. Fletcher, E. Zaremba, M. D'Iorio, C. T. Foxon, and J. J. Harris, Phys. Rev. B **41**, 10649 (1990).

[59] S. Mori and T. Ando, Phys. Rev. B **19**, 6433 (1979).

[60] R. Riera, J. L. Marin, H. León, and E. Roca, Nanostructured Materials **9**, 701 (1997).

[61] A. R. Nelson and E. Brown, Phys. Rev. B **9**, 1664 (1974).

[62] G.-Q. Hai, N. Stuart, and F. M. Peeters, Phys. Rev. B **52**, 8363 (1995).

[63] J. W. Harrison and J. R. Hauser, Phys. Rev. B **13**, 5347 (1976).

[64] P. K. Basu and B. R. Nag, Appl. Phys. Lett. **43**, 689 (1983).

[65] A. Gold, Phys. Rev. B **38**, 10798 (1988).

[66] R. E. Prange and T. W. Nee, Phys. Rev. **168**, 779 (1968).

[67] H. Sakaki, T. Noda, K. Hirakawa, M. Tanaka, and T. Matsusue, Appl. Phys. Lett. **51**, 1934 (1987).

[68] A. Gold, Phys. Rev. B **35**, 723 (1987).

[69] J. Majer, Diploma thesis, ETH Zürich, 8093 Zürich, Switzerland (1997).

[70] H. van Houten, J. G. Williamson, M. E. I. Broekaart, C. T. Foxon, and J. J. Harris, Phys. Rev. B **37**, 2756 (1988).

[71] T. P. Smith III and F. F. Fang, Phys. Rev. B **37**, 4303 (1988).

[72] T. P. Smith III, F. F. Fang, U. Meirav, and M. Heiblum, Phys. Rev. B **38**, 12744 (1988).

[73] H. L. Störmer, A. C. Gossard, and W. Wiegmann, Solid State Comm. **41**, 707 (1982).

[74] T. Englert, J. C. Maan, D. C. Tsui, and A. C. Gossard, Solid State Commun. **45**, 989 (1983).

[75] E. Zaremba, Phys. Rev. B **45**, 14143 (1992).

[76] P. Wirth, Diploma thesis, ETH Zürich, 8093 Zürich, Switzerland (1997).

[77] T. Heinzel, G. Salis, K. Ensslin, K. Maranowski, and A. C. Gossard, Physica B **0**, in print (1998).

[78] G. Salis, P. Wirth, T. Heinzel, T. Ihn, K. Ensslin, K. Maranowski, and A. C. Gossard, Phys. Rev. B **0**, submitted (1998).

[79] T. Ando, Journal of the Physical Sociecty of Japan **51**, 3900 (1982).

[80] T. Ando, A. B. Fowler, and F. Stern, Rev. Mod. Phys. **54**, 437 (1982).

[81] P. T. Coleridge, R. Stoner, and R. Fletcher, Phys. Rev. B **39**, 1120 (1989).

[82] M. Heiblum, E. E. Mendez, and F. Stern, Appl. Phys. Lett. **44**, 1064 (1984).

[83] P. T. Coleridge, Semicond. Sci. Technol. **5**, 961 (1990).

[84] P. T. Coleridge, Phys. Rev. B **44**, 3793 (1991).

[85] W. Walukiewicz, P. F. Hopkins, M. Sundaram, and A. C. Gossard, Phys. Rev. B **44**, 10909 (1991).

[86] I. L. Chuang, R. Laflamme, P. W. Shor, and W. H. Zurek, Science **270**, 1633 (1995).

[87] J. I. Cirac, T. Pellizzari, and P. Zoller, Science **273**, 1207 (1996).

[88] D. A. Lidar, I. L. Chuang, and K. B. Whaley, Phys. Rev. Lett. **81**, 2594 (1998).

[89] R. P. Feynman and F. L. Vernon, Ann. Phys. (N. Y.) **24**, 118 (1963).

[90] R. Landauer, Philos. Mag. **21**, 863 (1970).

[91] A. Stern, Y. Aharonov, and Y. Imry, Phys. Rev. B **41**, 4346 (1990).

[92] S. Chakravarty and A. Schmid, Physics Reports **140**, 193 (1986).

[93] B. L. Altshuler and A. G. Aronov, in *Electron-electron interactions in disordered systems*, *Modern problems in condensed matter sciences, Vol. 10*, edited by A. L. Efros and M. Pollak (Amsterdam a. o. : North Holland, 1985), p. 1.

[94] B. L. Altshuler, in *Soviet Scientific Reviews. Section A: Physics Reviews*, *Vol. 9*, edited by I. K. Khalatnikov (Harwood Academic New York, 1987).

[95] P. Mohanty, E. M. Q. Jariwala, and R. A. Webb, Phys. Rev. Lett. **78**, 3366 (1997).

[96] P. Mohanty and R. A. Webb, Phys. Rev. B **55**, R13452 (1997).

[97] B. L. Altshuler, M. E. Gershenson, and I. L. Aleiner, Los Alamos preprint server, cond matt **9803125**, (1998).

[98] B. L. Altshuler, JETP Lett. **41**, 648 (1985).

[99] P. A. Lee and T. V. Ramakrishnan, Rev. Mod. Phys. **57**, 287 (1985).

[100] B. L. Al'tshuler and P. A. Lee, Physics Today **12**, 36 (1988).

[101] P. A. Lee and A. D. Stone, Phys. Rev. Lett. **55**, 1622 (1985).

[102] P. A. Lee, A. D. Stone, and H. Fukuyama, Phys. Rev. B **35**, 1039 (1987).

[103] M. Huberty, Diploma thesis, ETH Zürich, 8093 Zürich, Switzerland (1998).

[104] C. W. J. Beenakker and H. van Houten, Phys. Rev. B **38**, 3232 (1988).

[105] T. Ihn, M. Huberty, G. Salis, K. Ensslin, O. Homan, W. Bächtold, K. Maranowski, and A. C. Gossard, Physica B **1**, 1 (1998).

[106] T. Ihn, M. Huberty, G. Salis, K. Ensslin, O. Homan, W. Bächtold, K. Maranowski, and A. C. Gossard, Proceedings of the International Conference on Physics of Semiconductors (ICPS) (1998).

[107] V. Fal'ko, J. Phys.: Cond. Matter **2**, 3797 (1990).

[108] G. S. Boebinger, A. Passner, L. N. Pfeiffer, and K. W. West, Phys. Rev. B. **43**, 12673 (1991).

[109] G. Salis, B. Ruhstaller, K. Ensslin, K. Maranowski, and A. C. Gossard, Phys. Rev. B **58**, 1436 (1998).

[110] B. Ruhstaller, Diploma thesis, ETH Zürich, 8093 Zürich, Switzerland (1997).

[111] J. C. Maan, *Two-Dimensional Systems, Heterostructures and Superlattices* (Springer, 1984), pp. 183–191, berlin, p. 183-191.

[112] R. Merlin, Solid State Commun. **64**, 99 (1987).

[113] F. Stern and W. E. Howard, Phys. Rev. **163**, 816 (1967).

[114] F. Stern, Phys. Rev. Lett. **21**, 1687 (1968).

[115] S. K. Bhattacharya, Phys. Rev. B **25**, 3756 (1982).

[116] W. Zawadzki, S. Klahn, and U. Merkt, Phys. Rev. B **33**, 6916 (1986).

[117] T. Jungwirth and L. Smrcka, J. Phys.: Condens. Matter **5**, L217 (1993).

[118] J. M. Heisz and E. Zaremba, Semicond. Sci. Technol. **8**, 575 (1993).

[119] S. J. Lee, M. J. Park, G. Ihm, M. L. Falk, S. K. Noh, T. W. Kim, and B. D. Choe, Physica B **184**, 318 (1993).

[120] J. Dempsey and B. I. Halperin, Phys. Rev. B **47**, 4662 (1993).

[121] L. Smrcka and T. Jungwirth, J. Phys.: Condens. Matter **6**, 55 (1994).

[122] D. M. Mitrinović, V. Milanović, and Z. Ikonić, Phys. Rev. B **54**, 7666 (1996).

[123] W. Beinvogl, A. Kamgar, and J. F. Koch, Phys. Rev. B **14**, 4274 (1976).

[124] J. C. Portal, R. J. Nicholas, M. A. Brummell, A. Y. Cho, K. Y. Cheng, and T. P. Pearsall, Solid State Commun. **43**, 907 (1982).

[125] S. Oelting, A. D. Wieck, E. Batke, and U. Merkt, Surf. Sci. **196**, 273 (1988).

[126] L. Smrcka, P. Vasek, J. Kolacek, T. Jungwirth, and M. Cukr, Phys. Rev. B **51**, 18011 (1995).

[127] G. R. Facer, B. E. Kane, R. G. Clark, L. N. Pfeiffer, and K. W. West, Phys. Rev. B **56**, 10036 (1997).

[128] M. Shayegan, T. Sajoto, J. Jo, and M. Santos, Phys. Rev. B **40**, 3576 (1989).

[129] B. J. van Wees, L. P. Kouwenhoven, E. M. M. Willems, C. J. P. M. Harmans, J. E. Mooij, H. van Houten, C. W. J. Beenakker, J. G. Williamson, and C. T. Foxon, Phys. Rev. B **43**, 12431 (1991).

[130] D. A. Wharam, T. J. Thornton, R. Newbury, M. Pepper, H. Ahmed, J. E. F. Frost, D. G. Hasko, D. C. Peacock, D. A. Ritchie, and G. A. C. Jones, J. Phys. C **21**, L209 (1988).

[131] B. J. van Wees, H. van Houten, C. W. J. Beenakker, J. G. Williamson, L. P. Kouwenhoven, D. van der Marel, and C. T. Foxon, Phys. Rev. Lett. **60**, 848 (1988).

[132] L. P. Kouwenhoven, C. M. Marcus, P. L. Mceuen, S. Tarucha, R. M. Westervelt, and N. S. Wingreen, in *Mesoscopic electron transport, Proceedings of the NATO Advanced Study Institute on Mesoscopic Electron Transport*, edited by L. L. Sohn, L. P. Kouwenhoven, and G. Schoen (Luwer Academic, 1997).

[133] V. Fock, Z. Phys. **47**, 446 (1928).

[134] C. G. Darwin, Proc. Cambridge Philos. Soc. **27**, 86 (1931).

[135] W. Hansen, T. P. Smith III, K. Y. Lee, J. A. Brum, C. M. Knoedler, J. M. Hong, and D. P. Kern, Phys. Rev. Lett. **62**, 2168 (1989).

[136] S. E. L. A. Kumar and F. Stern, Phys. Rev. B **42**, 5166 (1990).

[137] B. T. Miller, W. Hansen, S. Manus, R. J. Luyken, A. Lorke, J. P. Kotthaus, S. Huant, G. Medeiros-Ribeiro, and P. M. Petroff, Phys. Rev. B **56**, 6764 (1997).

[138] A. G. Scherbakov, E. N. Bogachek, and U. Landman, Phys. Rev. B **53**, 4054 (1996).

[139] Y. Sun and G. Kirczenow, Phys. Rev. Lett. **72**, 2450 (1994).

[140] G. Salis, T. Heinzel, K. Ensslin, O. Homan, W. Bächtold, K. Maranowski, and A. C. Gossard, in *Proceedings of 24rd ICPS Jerusalem* (1998).

[141] C. G. Smith, M. Pepper, R. Newbury, H. Ahmed, D. G. Hasko, D. C. Peacock, J. E. F. Frost, D. A. Ritchie, G. A. C. Jones, and G. Hills, J. Phys.: Condens. Matter **1**, 6763 (1989).

[142] P. J. Simpson, D. R. Mace, C. J. B. Ford, I. Zailer, M. Pepper, D. A. Ritchie, J. E. F. Frost, M. P. Grimshaw, and G. A. C. Jones, Appl. Phys. Lett. **63**, 3191 (1993).

[143] I. M. Castleton, A. G. Davies, A. R. Hamilton, J. E. F. Frost, M. Y. Simmons, D. A. Ritchie, and M. Pepper, Physica B **251**, 157 (1998).

[144] M. Büttiker, Phys. Rev. B **41**, 7906 (1990).

[145] M. Robnik, J. Phys. A: Math. Gen. **19**, 3619 (1986).

[146] R. Held, T. Heinzel, P. Studerus, K. Ensslin, and M. Holland, Appl. Phys. Lett. **71**, 2689 (1998).

[147] R. Held, T. Vancura, T. Heinzel, K. Ensslin, M. Holland, and W. Wegscheider, Appl. Phys. Lett. **73**, 262 (1998).

Acknowledgements

I want to thank Prof. Klaus Ensslin for his guidance through this work and his enthusiasm for the experimental data and - more important - its possible explanations. He always took the time for a discussion or to come in the lab to take hands on the measurements. It was a great pleasure to work in his group.

Special thanks go to Prof. Gianni Blatter for his careful reading of the manuscript and his many comments. The discussions with him always lasted longer than intended, and the questions about the physics behind some formulae gave me new insights.

Thomas Ihn's didactic clarity in explaining theories, his readiness to discuss complicated formulae, and his hints and corrections in writing papers all deserve my gratitude. I thank Thomas Heinzel for his many ideas, his support, his immediate and thorough proof-reeding and his willingness to look after the cryostate on some week-ends.

I thank Bruno Graf for his professional introduction to the clean-room in Altstetten, and Otte Homan for his patience and support in making the e-beam lithography work. W. Bächtold is thanked for letting us use the electron microscope.

Prof. Sergio Ulloa and many other guests for discussions.

Especially I want to thank all people of our group – a group in which working was always a pleasure. Special thanks go to Sebastian Brosig for his instantaneous help with all kinds of computer troubles, particularly with Matlab, C and LaTeX, and for proof-reading the manuscript. Jörg Rychen for his many intelligent questions, the skiing tours, and the nice afternoons rock climbing in Ascona; Tobias Vancura for reading the manuscript and taking care of the computer stuff; Silvia Lüscher for the many good conversations, her useful suggestions on the manuscript, and the sports activities including three superb ascents above 4000 meters; Ryan Held for his support against infiltrations from the PC community; and Brigitte Abt for her organization talent, not only regarding the cakes on Fridays...

Furthermore I want to thank Rainer Jäggi, Stefan Lindemann, Elisabeth Müller and Evaldo Ribeiro for the good times in HPF E13.

Without Andreas Hermann, measuring would have been far more streneous, and the many inventions from Paul Studerus have made good measurements first possible.

I miss the comradeship and the discussions about the fascination of mountaineering with Stefan Lüthi during the first few months in the group.

I thank my Diploma and Term students including Beat Ruhstaller, Patrick Wirth, Marc Huberty and Leif Roschier for the good working atmosphere.

Special thanks go to Urs Gasser for his many comments on the manuscript and the

many summits conquered together.

I am happy that Nicole reminds me that there are more important things in life than physics. I wish to thank her for her patience and understanding, if for some reason physics was nevertheless important... Our many trips into nature on week-ends and vacations gave me the necessary distance to my work.

Curriculum Vitae

Gian Salis, geboren am 26.12.1970 in Mailand.
Bürger von Vicosoprano und Soglio (GR), Schweiz

Zivilstand: ledig
Eltern: Claire und Radolf Salis-Luisoli
Geschwister: Reto und Giulia Salis

1977-1982	Primarschule Liestal und Hölstein
1982-1986	Sekundarschule Oberdorf, progymnasiale Abteilung
1986-1989	Gymnasium Liestal
Dez. 1989	Matura Typus C
1990	Rekrutenschule
1990-1995	Physikstudium ETH Zürich
Okt. 1995	Diplom experimentelle Physik mit Auszeichnung
Jan. 1996	Beginn der Doktorarbeit an der ETH Zürich, Institut für Festkörperphysik, Gruppe Prof. Klaus Ensslin